MENDEL UNIVERSITY IN BRNO

FACULTY OF AGRISCIENCES

DEPARTMENT OF TECHNOLOGY AND AUTOMOBILE TRANSPORT

Degradation Analysis of Materials in Agriculture

Dissertation

Supervisor:

Ing.et Ing. Petr Dostál, Ph.D.

Author:

Piyapong Sriwongras

Brno 2016

Čestné prohlášení

Prohlašuji, že jsem práci: **"Degradation analysis of materials in agriculture"** vypracoval/a samostatně a veškeré použité prameny a informace uvádím v seznamu použité literatury. Souhlasím, aby moje práce byla zveřejněna v souladu s § 47b zákona č. 111/1998 Sb.,o vysokých školách ve znění pozdějších předpisů a v souladu s platnou *Směrnicí o zveřejňování vysokoškolských závěrečných prací.*

Jsem si vědom/a, že se na moji práci vztahuje zákon č. 121/2000 Sb., autorský zákon, a že Mendelova univerzita v Brně má právo na uzavření licenční smlouvy a užití této práce jako školního díla podle § 60 odst. 1 autorského zákona.

Dále se zavazuji, že před sepsáním licenční smlouvy o využití díla jinou osobou (subjektem) si vyžádám písemné stanovisko univerzity, že předmětná licenční smlouva není v rozporu s oprávněnými zájmy univerzity, a zavazuji se uhradit případný příspěvek na úhradu nákladů spojených se vznikem díla, a to až do jejich skutečné výše.

V Brně dne:……..

……..

podpis

ACKNOWLEDGEMENTS

First of all, I would like to express my sense of gratitude to my supervisor Ing. et Ing. Petr Dostál, Ph.D, who offered his continuous advice and invaluable encouragement throughout the course of this dissertation and my study in Czech Republic. Without his guidance and persistent helps, this dissertation would not have been possible.

I want to acknowledge a special thank Ing. František Vlašic, Ph.D, the reseacher at Brno University of Technology, for supporting and suggesting me how to use the acoustic emission device properly and efficiently in the experiments of this dissertation.

Also, I would like to thank my Ph.D colleagues at Department of Technology and Automobile Transport, Faculty of AgriSciences, Mendel University in Brno who kindly assist and work together to achieve the interesting experiments which are the partial part of this dissertation.

I am extremely grateful to my father (Prajak Sriwongras), my mother (Supa Sriwongras), my sister and also my girlfriend who are always my inspirations for reinforcing me to overcome all difficult tasks during my study in Czech Republic.

Last but not least, I would to express my great appreciation to both Mendel University in Brno (Czech Republic) and Kasetsart University (Thailand) to give me having the worth opportunity of studying in Ph.D program in Czech Republic.

The present dissertation was financially supported by IGA TP 4/2014 and IGA IP 26/2015.

Piyapong Sriwongras

August 2016

ABSTRAKT

Sriwongras, P.: Analýza degradačních vlastností materiálů využívaných v zemědělství Disertační práce, Mendelova univerzita v Brně. 2016

Předložená disertační práce se zabývá využitím akustické emise (AET), jako jedné z metod nedestruktivního testování, pro identifikaci kvality kovových materiálů používaných v zemědělské technice. Experimentální studie je rozdělena do dvou základních částí. První část představuje využití akustické emise v oblasti svařování „Cold Metal Transfer“ (CMT). Je hodnocena kvalita svařovacího procesu a rovněž kvalita svaru a to při korozní a mechanické degradaci. Druhá související část práce je věnována hořčíkovým slitinám, které jsou v současnosti používány v automobilovém průmyslu a mají potenciál využití i ve specifických zemědělských aplikacích. Výzkum v této oblasti je zaměřen na hodnocení vysoko-cyklové únavy při různých stádiích korozní degradace hořčíku. Rovněž je řešena problematika obtížné svařitelnosti tohoto materiálu. Pozornost je věnována i CMT svařování dvou různých základních materiálů, zejména hořčíkové slitiny AZ31B s hliníkovou slitinou EN AW 6065, dále pozinkovaného plechu DX51D rovněž s hliníkovou slitinou. Výsledky deklarují způsob, jakým lze použít akustickou emisi pro kvalitativní hodnocení svařovacího procesu i procesu mechanické a korozní degradace vzorků. Byla prokázána efektivita monitoringu akustické emise při ochlazovací fázi po svařování. Tyto záznamy slouží k optimalizaci svařovacího procesu. Rovněž byl akustickou emisí detekován a vizualizován rozdíl mechanické odolnosti vzorků bez koroze a s korozí při tahových a únavových zkouškách. Pro účelné hodnocení kvality hořčíkových slitin při dynamickém zatížení byl použit vysokofrekvenční pulsátor. Aplikací akustické emise byl vizualizován stupeň snížení únavové životnosti vlivem korozní degradace. Práce předkládá aplikovatelné výsledky pro využití akustické emise při hodnocení kvality inovativních materiálů při mechanické a korozní degradaci a při svařovacím procesu. Smysl této práce je v prohloubení znalostí o možných moderních přístupech v hodnocení kvality za účelem identifikace nových aplikačních oblastí specifických materiálů, zvyšování kvality produkce a bezpečnosti při snižování nákladů.

Práce byla podpořena interní grantovou agenturou AF Mendelu.

Klíčová slova: akustická emise, koroze, únava, hořčík, svařování

ABSTRACT

Sriwongras, P.: Degradation analysis of materials in agriculture

Dissertation Thesis, Mendel University in Brno. 2016

The present dissertation deals with the application of acoustic emission testing (AET) as one of the non-destructive testing to identify the quality of metal materials used in agricultural technology. Experimental study is divided into two parts. The first part is the use of AET in welding by "Cold Metal Transfer" (CMT). The quality of the welding process and the welded specimens is evaluated, especially in corrosion and mechanical degradation. Second part is devoted to magnesium alloys which are currently being used in the automotive industry and have the potential utilization in specific agricultural applications as well. Research in this area is focused on the evaluation of high-cyclic fatigue at different stages of corrosion degradation of magnesium. The problems of weldability of the material are solved. Attention is also focused on the CMT welding of two dissimilar materials, especially in AZ31B magnesium alloy and EN AW 6065 aluminum alloy, further DX51D galvanized steel and aluminum alloy. Results declare a way to use AET for qualitative evaluation of the welding process and process of mechanical and corrosive degradation of specimens. The efficiency of AET during the cooling phase after welding was demonstrated. These records are used to optimize the welding process. The mechanical resistance of the specimens with and without corrosion in tensile and fatigue tests was detected and visualized by means of AET. The high-frequency pulsator was used for practical evaluation of the quality of magnesium alloys under dynamic loading. The degree of reduction of fatigue life due to corrosion degradation was visualized by application of AET. The work presents the applicable results of using AET in the qualitative evaluation of innovative materials during mechanical and corrosive degradation as well as during the welding process. Therefore, the sense of this work is to deepen knowledge about the potential of modern approaches for qualitative assessment in order to identify new areas of specific material application, improving production quality and safety as well as reducing costs. The work was supported by the Internal Grant Agency AF MENDELU.

Keywords: acoustic emission, corrosion, fatigue, magnesium, welding

CONTENTS

INTRODUCTION

Selection of the appropriate materials in development of machinery is great significant to increase its service life and working performance. Recently, using lightweight materials and welding the dissimilar metals in production processes are the methods that have been widely used to design and develop the structure of machinery in order to improve the strength of machine, reduce the weight of machine, and minimize the production cost.

Cold metal transfer welding process (CMT) is the outstanding technology to connect the dissimilar metals, particularly in metal sheet. CMT has been broadly used in several industries such as, automotive manufacturer because it provides many advantage points, for example, reduction of thermal input, preparation of spatter-free metal, weldment of the dissimilar metals. However, welding the dissimilar metals must be carefully considered about the degradation process occurring on welded materials due to welding process and galvanic corrosion. Therefore, using specific monitoring method in welded materials during both welding process and post-welding process is necessary to estimate the quality of welded materials.

Acoustic emission method (AET) is one of non-destructive method (NDT) that is based on the generation of elastic waves produced by a sudden redistribution of stress in a material. It is a powerful method for examining the behavior of materials deforming under stress. Moreover, AET can be also used to evaluation of many forms of manufacturing such as, monitoring the qualities of welding process, inspecting the corrosion process of materials, and detecting fatigue failure of materials. Therefore, due to its versatility, it is very interesting to investigate more information of using acoustic emission method for monitoring the degradation of lightweight materials and welded dissimilar metals when these materials are in production process and loading condition.

From many reasons mentioned above, thus, monitoring the degradation process of metal materials used in agricultural tools by using non-destructive technique was studied in the present dissertation. In the experiments, acoustic emission system was mainly employed to detect the acoustic emission activities generated from the test materials during welding process, corrosion process, and mechanical testing processes. The all experimental results were discussed and reported in order to be the useful information for developing the inspecting system in manufacturing process, corrosion protection, and failure prevention by means of acoustic emission method.

CHAPTER 1: BACKGROUND AND LITERATURE REVIEW

1.1 Aluminum alloys

About 7.5% of the earth's crust, aluminum is the most abundant metal and the third most abundant element in the earth's crust. Bauxite, which consists mainly of hydrated aluminum oxides, is the chief commercial mineral used for the production of aluminum. In the Bayer process, bauxite is reacted with hot sodium hydroxide to convert the aluminum in the ore to sodium aluminate. After separation of the insoluble material, aluminum hydroxide is precipitated from the aluminate solution. The aluminum hydroxide is the thickened and calcined to aluminum oxide, Al_2O_3.

The aluminum oxide is dissolved in a molten bath of cryolite (Na_3AlF_6) and electrolyzed in an electrolytic cell (figure 1.1) by using carbon anodes and cathodes. In the electrolysis process, metallic aluminum forms in the liquid state and sinks to the bottom of the cell and is periodically tapped off. The cell-tapped aluminum usually contains from 99.5 to 99.9 percent aluminum with iron and silicon being the major impurities [85].

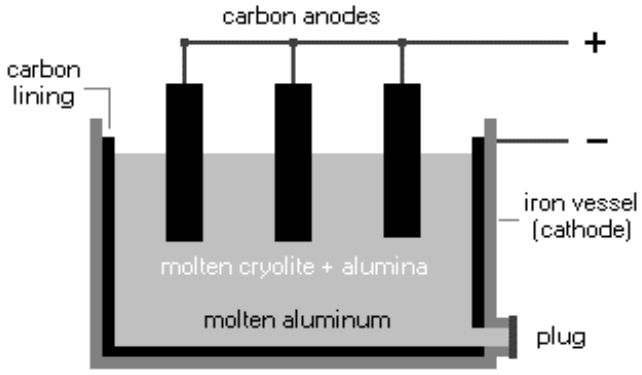

Figure 1.1: Electrolytic cell used to produce aluminum. [17]

Aluminum alloys can be categorized into the wrought and cast aluminum alloys. The wrought and cast aluminums have different systems of identification. Technically, the wrought system is a four-digit system and the castings have a three-digit and one-decimal place system.

1.1.1 Wrought aluminum alloys

Aluminum alloys produced in the wrought form (i.e., sheet, plate, extrusions, rod, and wire) are classified according to their major alloying elements and their precipitation-

strengthened processes. A four-digit numerical designation is used to identify aluminum wrought alloys. The first digit indicates the alloy group that contains specific alloying elements. The last two digits identify the aluminum alloy or indicate the aluminum purity. The second digit indicates modification of the original alloy or impurity limits. Table 1 lists the wrought aluminum alloy groups [86].

Table 1: Wrought aluminum alloy designation system. [2]

Alloy series	Principal alloying element	Alloy properties
1xxx	99.000% Minimum Aluminum	Non-heat treatable
2xxx	Copper	Heat treatable
3xxx	Manganese	Non-heat treatable
4xxx	Silicon	Heat treatable/ non-heat treatable
5xxx	Magnesium	Non-heat treatable
6xxx	Magnesium and Silicon	Heat treatable
7xxx	Zinc	Heat treatable
8xxx	Other elements	-

1.1.1.2 Temper designations

Temper designations for wrought aluminum alloys follow the alloy designation and are separated by a hyphen (for example, 1100-0). Subdivisions of a basic temper are indicated by one or more digits and follow the letter of the basic designation (for example, 1100-H14).

1.1.1.3 Basic temper designations

F - As fabricated. No control over the amount of strain hardening; no mechanical property limits.

O - Annealed and recrystallized. Temper with the lowest strength and highest ductility.

H - Strain-hardened. Applies to product that are strengthened through cold-working. The strain hardening may be followed by supplementary thermal treatment, which produces some reduction in strength. The “H” is always followed by two or more digits (see subdivisions of H temper below).

T - Thermally treated. To produce stable tempers other than F, O, or H. Applies to product that has been heat-treated, sometimes with supplementary strain-hardening, to produce a stable temper. The “T” is always followed by one or more digits (see subdivisions of T temper below).

1.1.1.4 Strain-hardened subdivisions

H1 – Strain-hardened only. The degree of strain hardening is indicated by the second digit and varies from quarter-hard (H12) to full-hard (H18), which is produced with approximately 75 percent reduction in area.

H2 – Strain-hardened and partially annealed. Tempers ranging from quarter-hard to full-hard obtained by partial annealing of cold-worked materials with strengths initially greater than desired. Tempers are H22, H24, H26, and H28.

H3 – Strain-hardened and stabilized. Tempers for age-softening aluminum-magnesium alloys that are strain-hardened and then heated at a low temperature to increase ductility and stabilize mechanical properties. Tempers are H32, H34, H36, and H38.

1.1.1.5 Heat-treated subdivisions

T1 – Naturally aged. Product is cooled from an elevated-temperature shaping process and naturally aged to a substantially stable condition.

T2 – Cold worked after cooling from an elevated temperature shaping process and then naturally aged.

T3 – Solution heat-treated, cold-worked, and naturally aged to a substantially stable condition.

T4 – Solution heat-treated and naturally aged to a substantially stable condition.

T5 – Cooled from an elevated-temperature shaping process and then artificially aged.

T6 – Solution heat-treated and then artificially aged.

T7 – Solution heat-treated and stabilized.

T8 – Solution heat-treated, cold-worked, and then artificially aged.

1.1.1.6 Aluminum alloys and their characteristics

1xxx Series Alloys

This series is often referred to as the pure aluminum series because it is required to have 99.0% minimum aluminum. However, because of their narrow melting range, they require certain considerations in order to produce acceptable welding procedures. When considered for fabrication, these alloys are selected primarily for their superior corrosion resistance such as in specialized chemical tanks and piping. These alloys have relatively poor mechanical properties and would seldom be considered for general structural applications. These base alloys are often welded with matching filler material or with 4xxx filler alloys dependent on application and performance requirements.

2xxx Series Alloys

These are aluminum / copper alloys (copper additions ranging from 0.7 to 6.8%), and are high strength, high performance alloys that are often used for aerospace and aircraft applications. They have excellent strength over a wide range of temperature. These base materials are often welded with high strength 2xxx series filler alloys designed to match their performance, but can sometimes be welded with the 4xxx series fillers containing silicon or silicon and copper, dependent on the application and service requirements.

3xxx Series Alloys

These are the aluminum / manganese alloys (manganese additions ranging from 0.05 to 1.8%) and are of moderate strength, good corrosion resistance, and good formability. One of their first uses was pots and pans, and they are the major component today for heat exchangers in vehicles and power plants. Their moderate strength, however, often precludes their consideration for structural applications. These base alloys are welded with 1xxx, 4xxx and 5xxx series filler alloys, dependent on their specific chemistry and particular application and service requirements.

4xxx Series Alloys

These are the aluminum / silicon alloys (silicon additions ranging from 0.6 to 21.5%) and are the only series that contain both heat treatable and non-heat treatable alloys. Silicon, when added to aluminum, reduces its melting point and improves its fluidity when molten. These characteristics are desirable for filler materials used for both fusion welding and brazing. Consequently, these series of alloys are predominantly found as filler material. Silicon, independently in aluminum, is non-heat treatable; however, a

number of these silicon alloys have been designed to have additions of magnesium or copper, which provides them with the ability to respond favorably to solution heat treatment. Typically, these heat treatable filler alloys are used only when a welded component is to be subjected to post weld thermal treatments.

5xxx Series Alloys

These are the aluminum / magnesium alloys (magnesium additions ranging from 0.2 to 6.2%) and have the highest strength of the non-heat treatable alloys. In addition, this alloy series can be readily welded, and for these reasons they are used for a wide variety of applications such as shipbuilding, transportation, pressure vessels, bridges and buildings. The magnesium base alloys are often welded with filler alloys, which are selected after consideration of the magnesium content of the base material, and the application and service conditions of the welded component. Alloys in this series with more than 3.0% magnesium are not recommended for elevated temperature service above 150 °F because of their potential for sensitization and subsequent susceptibility to stress corrosion cracking. Base alloys with less than approximately 2.5% magnesium are often welded successfully with the 5xxx or 4xxx series filler alloys.

6XXX Series Alloys

These are the aluminum / magnesium - silicon alloys (magnesium and silicon additions of around 1.0%) and are found widely throughout the welding fabrication industry, used predominantly in the form of extrusions, and incorporated in many structural components. The addition of magnesium and silicon to aluminum produces a compound of magnesium-silicide, which provides this material its ability to become solution heat treated for improved strength. These alloys are naturally solidification crack sensitive, and for this reason, they should not be arc welded autogenously (without filler material). The addition of adequate amounts of filler material during the arc welding process is essential in order to provide dilution of the base material, thereby preventing the hot cracking problem. They are welded with both 4xxx and 5xxx filler materials, dependent on the application and service requirements.

7XXX Series Alloys

These are the aluminum / zinc alloys (zinc additions ranging from 0.8 to 12.0%) and comprise some of the highest strength aluminum alloys. These alloys are often used in high performance applications such as aircraft, aerospace, and competitive sporting equipment. The commonly welded alloys in this series, such as 7005, are predominantly welded with the 5xxx series filler alloys [2].

1.1.2 Cast aluminum alloys

Cast aluminum components are used for many varied functions, from decorative home, such as lighting fixtures, to highly engineered, safety-critical components for aerospace and automotive applications as shown in figure 1.2. Technically, casting process of aluminum alloys can be separated into three main processes: sand casting, permanent-mold, and die casting.

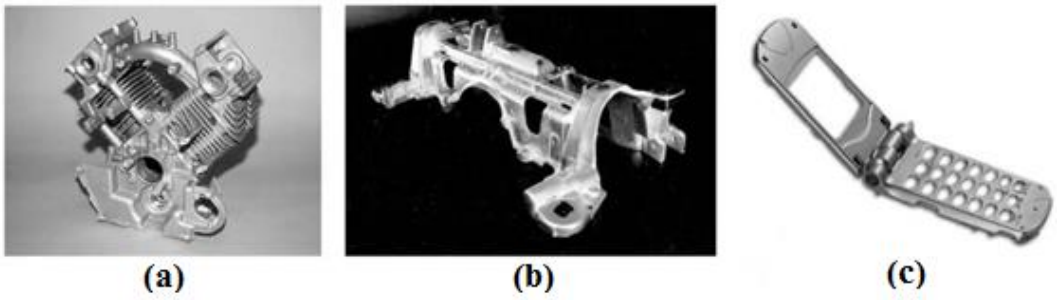

Figure 1.2: Aluminum casting alloy application. (a) Crank case for small engine, (b) Cross member for a minivan, (c) mobile case. [7]

Sand casting is the simplest and most versatile of the aluminum casting processes and it is usually chosen for the production of small quantities of identical castings, complex castings with intricate cores, and large castings. In permanent-mold casting, the molten metal is poured into a permanent metal mold under gravity, low pressure, or centrifugal pressure. Casting of the same alloy and shape produced by a permanent mold have a finer grain structure and higher strength than those cast by sand mold. However, permanent mold have size limitations, and complex parts may be difficult to cast with a permanent mold. For dis casting, identical parts are cast at maximum production rates by forcing molten metal under considerable pressure into metal molds. The molten aluminum is forced into the cavities in the dies until the metal has solidified. Some of the advantages of die casting are producing workpieces at high rates, obtaining the smooth surfaces on the casting, and getting dimensional tolerances of each cast part more closely held than with any other major casting process [106].

In generally, silicon in the range of about 5 to 12 percent is the most important alloying element in aluminum casting alloys since it increases the fluidity of the molten metal and its feeding ability in the mold as well as strengthens the aluminum. Magnesium in the range of about 0.3 to 1 percent is added to increase strength. Copper in range of about 1 to 4 percent is also added to some aluminum casting alloys to increase strength,

particularly at elevated temperatures. Other alloying elements such as zinc, tin, titanium, and chromium are also added to some aluminum casting alloys [85].

1.1.2.1 Aluminum casting alloy designation system

The system designates individual aluminum casting alloys using a three-digit number plus a decimal. The standard specifies the chemical compositions of aluminum alloys and the percentage of each alloying element. The first digit of the three-digit number system categorizes the casting alloys by groups (or series) according to their major alloying elements as seen in table 2.

Table 2: Aluminum alloy classification system. [3]

Alloy Series	Principal Alloy Element
1xx.x	99% minimum aluminum
2xx.x	Copper
3xx.x	Silicon + Magnesium, Silicon + Copper
4xx.x	Silicon
5xx.x	Magnesium
7xx.x	Zinc
8xx.x	Tin

The three-digit number identifies the various individual alloys within each alloy series. For instance, the 300 series of alloys includes more than 50 individual alloys (319, 356, 357, 380, etc.). Some of these individual alloys have multiple variations, all using the same three-digit number. These alloy designations include a letter before the three-digit alloy designation. For example, variations of 356 are A356, B356, C356 and F356. This letter distinguishes between alloys that differ only slightly in percentages of impurities or alloying elements, and the single digit following the decimal indicates how the alloy will be used. These designations include: xxx.0 indicates the chemistry limits applied to an alloy casting, xxx.1 indicates the chemistry limits for ingot used to make the alloy casting, and xxx.2 indicates ingot but with somewhat different chemical limits [67]. Table 3 lists various aluminum casting alloy series that are used in many applications nowadays.

Table 3: Typical applications of aluminum casting compositions. [57]

Alloy	Application
319.0	Engine crank cases, gas and oil tanks, engine oil pans
355.0	Air compressor pistons, printing press
356.0	Flywheel castings, automotive transmission cases
A356.0	High strength airframe, machine parts, truck chassis parts
A357.0	High strength aerospace castings

1.1.3 Basic phenomena of corrosion of aluminum materials

The generally good corrosion resistance of "aluminum" is based on the stability and adherence of its natural, protective oxide film. Since the bare metal is rather reactive in aqueous environments, corrosion attack is only experienced where the protective oxide film is penetrated or destroyed and prevented from regeneration.

The natural compact and adherent film of aluminum oxide forms when a fresh aluminum surface is exposed to air. The thickness of the oxide film on the rolled metal sheet of aluminum is 2.5 nm approximately and grows over the years to 10 – 20 nm.

The Al-oxide film is stable over the range of pH 4.5 to 8.5. When the oxide film dissolves, e.g. in strong acids and alkalis, dissolution of the metal occurs too, i.e. the metal corrodes. Therefore aluminum is termed an amphoteric metal. The presence of certain anions (e.g. Cl^-) or cations (e.g. $Cu2^+$) also has an influence on the stability of the oxide film. The diagram in figure 1.3 shows the regions of immunity and passivity as a function of pH-value and electrode potential [30].

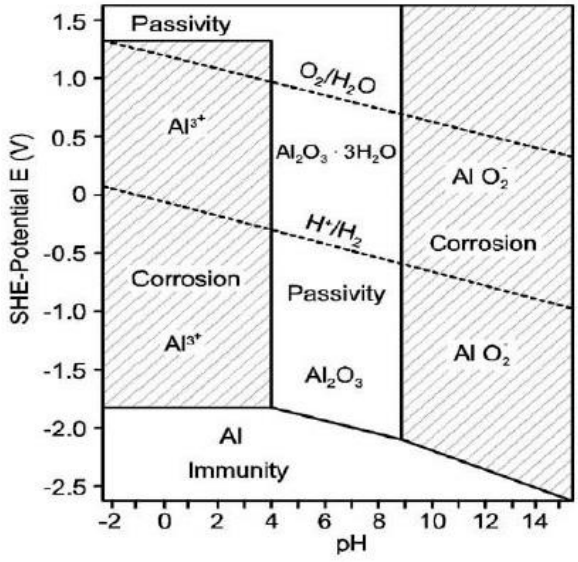

Figure 1.3: Potential-pH diagram due to Al with oxide film in solution at 25°C. [30]

1.2 Magnesium alloys

Magnesium is the lightest of all commonly used structural materials with a density of 1.7g/cm^3. With the lowest density of all commercial casting alloys, magnesium is 33 percent lighter than aluminum and 75 percent lighter than steel [66]. It is the third most abundant metallic element in the earth's crust. However, it is rarely found in its pure form due to the fact that it bonds with other elements easily. It was first produced in 1808 in small quantities by Sir Humphrey Davy and industrial production first began in 1886. Magnesium was first found in an area of Greece called Magnesia. The ore got its name from this location and can still be found in great quantities there [45].

Magnesium alloys are used around the world in a variety of different applications. It is a preferred material when looking for weight reduction without compromising overall strength. The vibration damping capacity is also beneficial in applications in which the internal forces of high-speed components must be reduced [80]. The most common applications of magnesium alloys consist of aircraft components, automotive structures and electronic appliances as shown in figure 1.4.

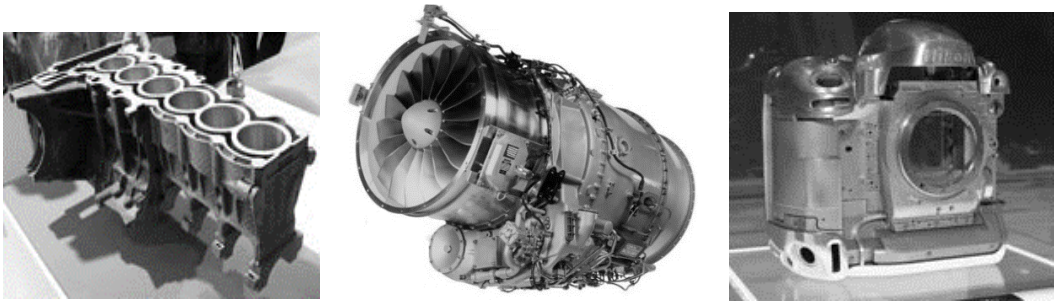

(a) *(b)* *(c)*

Figure 1.4: Magnesium alloys constructed as car cylinder block (a), airplane turbofan (b), camera structure (c). [62]

Unalloyed magnesium is not extensively used for structural purposes because it is susceptible to be corroded by corrosive environments. Consequently, the corrosion resistance of magnesium alloys is of primary concern. Two major magnesium alloy systems are available to the designer.

The first includes alloys containing 2 to 10%Al, combined with minor additions of zinc and manganese. These alloys are widely available at moderate cost, and their room-temperature mechanical properties are maintained to 95 to 120 °C. Beyond this,

elevated temperatures adversely affect mechanical properties and the corrosion properties deteriorate rapidly with increasing temperature.

The second group consists of magnesium alloyed with various elements (rare earths, zinc, thorium, and silver) except aluminum, all containing a small but effective zirconium content that imparts a fine grain structure and thus improved mechanical properties. These alloys generally possess much better elevated-temperature properties, but the more costly elemental additions combined with the specialized manufacturing technology required result in significantly higher cost [10]. Table 4 demonstrates some of the compositions commonly available in both systems.

Table 4: Common magnesium alloys. [91]

Alloy Designation	**Alloying Additives**	**Uses**	**Reasons for use**
AZ91	9.0%Al,0.7%Zn, 0.13%Mn	General casting alloy	Good castability, good mechanical properties at T<150'C.
AM60	6.0%Al, 0.15%Mn	High pressure die casting alloy	Greater toughness and ductility than AZ91, slightly lower strength, Often preferred for automotive structural applications.
AZ31	3.0%Al, 1.0%Zn, 0.2%Mn	Wrought magnesium products	Good extrusion alloy.
ZE41	4.2%Zn, 1.2%RE, 0.7%Zr	Specialist casting alloy	Rare earth addition improves creep strength at elevated temperatures.

Aluminum Zinc Alloy. The AZ alloys, which contain zinc as a secondary alloying element, solidify with a sufficiently fine grain size to meet most property requirements. They can be casted and have a minimum tendency toward hot cracking; this tendency increases with increasing zinc content. Alloy AZ91 is the most commonly used of all magnesium alloy due to its relatively low cost and excellent mechanical properties and processing characteristics [80]. Figure 1.5 illustrates the tensile property of AZ91 in various temperatures.

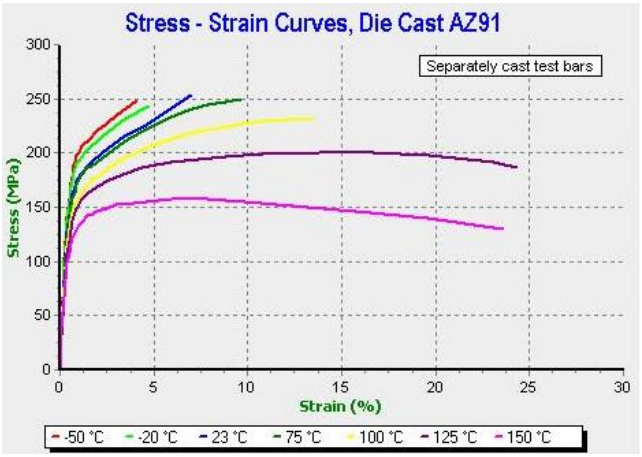

Figure 1.5: Stress/strain curves versus different temperatures. [44]

Zinc, Rare Earth and Silver Alloys. In these alloys the very effective precipitation hardening reactions of the Mg-Zn binary and the grain refining effect of zirconium combine to yield high strengths with good ductility. The Mg-Zn alloys with zirconium, thorium, or rare earth elements can provide very good combinations of room temperature yield strength and elongation. As the zinc content in these alloys is increased, micro-porosity and hot cracking become a problem, and this tends to be less severe in the alloys containing thorium or rare earth (RE) elements. All of these grades tend to be more costly than Mg-Al alloys and are used selectively when service temperatures exceed about 150 °C [80].

1.2.1 Wrought magnesium alloy

Wrought materials are produced mainly by extrusion, rolling, and press forging at temperatures in the range of 300 to 500 °C. Specific alloys have been developed that are suitable for wrought products, most of which fall into the same categories as the casting alloys. Examples of sheet and plate alloys are AZ31, which is the most widely used one because it offers a good combination of strength, ductility, and corrosion resistance.

Higher strength alloys such as AZ81 have strength/weight ratios comparable to those of the strongest wrought aluminum alloys [87].

1.2.2 Cast magnesium alloy

Two major cast magnesium alloy systems are available to the designer. The first system includes alloys containing 2 to 10% Al, combined with minor additions of zinc and manganese. These alloys are widely available at moderate cost, and their mechanical properties are satisfactory up to 120 °C. The second system consists of magnesium alloyed with various elemental additions and all contain a small but important zirconium addition that imparts a fine grain structure which improves mechanical properties. These alloys generally possess much better elevated-temperature properties, but their more costly elemental additions, combined with the specialized manufacturing technology required, result in significantly higher costs [80].

1.2.3 Advantages of magnesium alloy

Magnesium alloy properties can provide a casting designer with several advantages as an engineering material over other lightweight alloys.

Weight – The lightest of all structural metals, magnesium preserves the light weight of a design without sacrificing strength and rigidity. This benefit is important when portability is a key element of the product design, such as with chainsaws, pneumatic nailers, circular saws, luggage, laptop computers and cellular phones. Automobiles and other transportation equipment continue to take advantage of magnesium's low density in expanding application areas ranging from under-hood and driveline used found in engine brackets and transfer cases to numerous interior parts, such as steering column components, pedal brackets, instrument panel supports and seating.

Damping capacity – Magnesium in unique among metals because of its ability to absorb energy. Increased vibration absorption capacity provides for quieter operation of equipment when magnesium castings are used for housings and enclosures.

Dimensional stability – Annealing, artificial-aging or stress-relieving treatments normally are not necessary to achieve stable final dimensions. Metallurgical changes in the structure of some metals can affect dimensions after prolonged exposure to elevated temperatures, but this is not the case with magnesium alloys. As a result, there have been few problems associated with the dimensional change of castings in assemblies. Magnesium shrinkage rates are more consistent and predictable in comparison to other

nonferrous metals. Components release from the die with minimal force and distortion, hence they have minimal residual casting stress.

Impact and Dent resistance – The elastic energy absorption characteristics of magnesium result in good impact and dent resistance and energy management, which is one reason magnesium castings can be used for automotive safety-related applications, such as air bag systems. Portable tools and handheld electronics also benefit from this combination of properties, offering mechanical shock resistance.

Anti galling – Magnesium alloys possess a low galling tendency and can be used as a bearing surface in conjunction with a shaft hardness above 400 Brinell measurement [10].

1.2.4 Magnesium alloy designation

Magnesium alloys are designated by a combination of letters and number, which was established by ASTM International. Figure 1.6 shows the abbreviation letters for the alloying elements that are commonly used to designate the magnesium alloys. Each alloy is labeled by letters that indicate the main alloying element.

Alloying element	Abbreviation letter
Aluminum	A
Bismuth	B
Copper	C
Cadmium	D
Rare earth metals	E
Iron	F
Thorium	H
Zirconium	K
Lithium	L
Manganese	M
Nickel	N
Lead	P
Silver	Q
Chromium	R
Silicon	S
Tin	T
Yttrium	W
Antimony	Y
Zinc	Z

Figure 1.6: Abbreviation letters identified alloying elements in magnesium alloys. [39]

The designation of a typical magnesium alloy consists of four parts. For part 1, the initial alphabet of two main alloying elements makes two abbreviation letters, which represent the two main alloying elements arranged in order of decreasing percentage. If the percentages of the alloying elements are equal, the letters are arranged alphabetically.

For part 2, the amounts (in weight percentage terms) of the two main alloying elements are stated. It consists of two whole numbers, which corresponds to the alphabets. For part 3, it distinguishes between the different alloys with the same percentages of the two main alloying elements. It is made up of a letter of the alphabet assigned in order as compositions become standard, namely: A is original composition, B is second modification, C is third modification, D indicates high purity and E is high corrosion resistance. Finally, the fourth part, it is the temper designations that may be added to indicate in terms of heat treating, strain hardening, aging, etc. The temper designations are the same system as those used for aluminum [12].

For example, considering magnesium alloy AZ81A-T4:

AZ Indicates that aluminum and zinc are the two principal alloying elements

81 Indicates the percentages of aluminum and zinc (8 and 1, respectively), which are rounded-off to whole numbers

A Indicates that it is the first alloy standardized with 8% Al and 1%Zn as the principal alloying additions.

T4 Indicates that the alloy is solution heat-treated.

1.2.5 Corrosion failures in magnesium alloy

Causes of corrosion failures typically include heavy-metal contamination, blast residues, flux inclusions, and galvanic attack.

Heavy-metal contamination often results in general pitting attack that is unassociated with fasteners or dissimilar-metal attachments. The rate of attack on unpainted surfaces will be essentially unaltered by surface condition, that is, freshly sanded, machined, or acid pickled.

Blast residues can cause general pitting attack in saline environments. Attack is normally limited to un-machined surfaces of sand castings. Sanded or acid-etched (2% H_2SO_4 for 15 to 30s) samples will show vastly improved performance in saltwater immersion or salt-spray tests because of removal of the contaminant. Scanning electron microscopy and energy-dispersive x-ray analysis samples cleaned in chromic acid (H_2CrO_4) can be used to confirm and identify the presence of the contaminant, which is usually iron or silica.

Flux inclusions result in localized attack that is clustered or distributed randomly on machined surfaces of castings. Freshly machined surfaces exposed to 70 to 90% relative humidity will develop active corrosion sites overnight. Scanning electron

microscopy/energy-dispersive x-ray analysis of a freshly machined surface will reveal pockets of magnesium and potassium chloride, as well as possible traces of calcium, barium, and sulfur. In zirconium-bearing alloys, elemental zirconium and zirconium-iron compounds may also be associated with the deposits. Chromic-acid pickling followed by chemical treatment and surface sealing can alleviate the problem of inclusions in finished castings. With the use of sulfur hexafluoride (SF_6) rapidly replacing fluxes for the protection of melts during casting, this problem should be eliminated in the future.

Galvanic attack is usually observed as heavy localized attack on the magnesium, normally within 3.2 to 4.8 mm (1⁄8 to 3⁄16 in.) of fasteners or an interface with other parts of dissimilar metal. Proper design and assembly methods, especially in the area of joints, can minimize galvanic attack [10].

1.3 Corrosion

Corrosion is the deterioration of materials due to reactions with their environments. From a practical standpoint, the term materials refers to those substances used in the construction of machines, process equipment, and other manufactured products. These materials include metals, polymers, and ceramics. The environments are liquids or gases, although under special circumstances certain solid-solid reactions might be included as corrosion [35].

1.3.1 Basic reaction of metal in an environment

Generally, there are three reactions of a metal occurring, when a metal is immersed in an environment. These reactions are depicted schematically in figure 1.7 which represents a metal partially immersed in a corrosive environment.

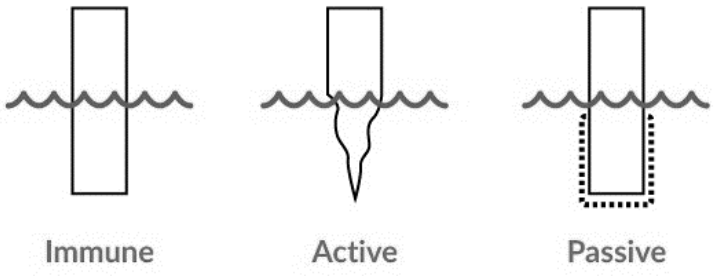

Figure 1.7: Typical corrosion behaviors of metal in an environment. [5]

Metals are, technically, organized into a list called the galvanic series which orders metals based on their electrode potentials, and consequently their tendency to corrode.

From this list, metals can be categorized into three general corrosion behaviors: immune, active, and passive.

Immune behavior is that the metal is immune in an environment, and also called noble metal. The metals represent this property such as gold, silver, and platinum. For a combination of metal and environment resulting in immune behavior, there is no reaction of the metal, and there is no corrosion of the metal.

Active behavior is that metal corrodes in the solution. When active behavior is noticed, the metal dissolves in solution. Corrosion or dissolution of the metal continues in this solution because the corrosion products do not prevent subsequent corrosion. Therefore, Active corrosion is described by high weight loss of the metal. Many metals are considered as active behavior, for example, Magnesium, tin and carbon steel.

Passive behavior is situation that the metal corrodes but a state of passive behavior is observed. On immersion of the metal in the solution there is a reaction, and the metal does corrode. However, protective corrosion-product film, also referred to as a passive film, is formed. This thin passive film prevents the reaction rate to very low levels. Some examples of metals that exhibit passivity are iron, chromium, titanium and nickel.

1.3.2 Galvanic series

The galvanic series is a ranking of metals from the most noble to the most active in a certain environment. Figure 1.8 depicts a galvanic series of several metals and alloys in seawater. As in the most noble, or cathodic, metals are listed at the top of the series. The ranking proceeds downward to the most active, or anodic, metals.

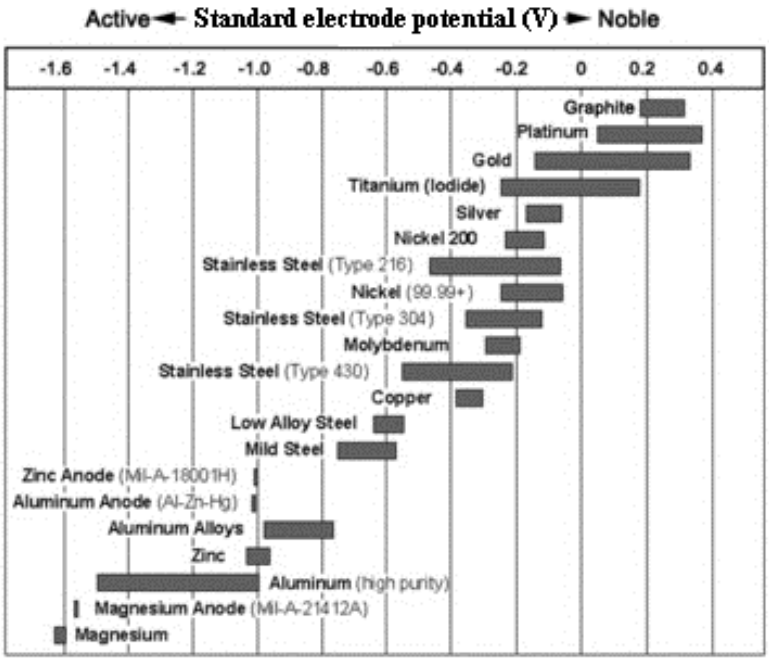

Figure 1.8: Galvanic series for common construction metals. [1]

When dissimilar metals are connected, considering the tendency of detrimental corrosion effect by using the galvanic series is very important. For example, a galvanic couple between platinum and magnesium is disastrous because the farther apart two metals are on the galvanic series, the more likely that detrimental galvanic corrosion will occur, whereas two metals are closer together in the galvanic series, the detrimental galvanic effect is lessened.

1.3.3 Corrosion reaction

Corrosion is a process through which metals in manufactured states return to their natural oxidation states [98]. This process is usually called an electrochemical reaction in which the metal is being oxidized by its surroundings.

The processes of an electrochemical reaction are that oxidation (the generation of electrons) and reduction (consumption of electrons) both happen, and there is an electron transfer from the anode to the cathode. The processes of an electrochemical reaction are illustrated by considering the behavior of iron in hydrochloric acid [23]. The reaction is:

$$Fe + 2H^+ + 2Cl^- \rightarrow Fe^{2+} + 2Cl + H_2 \qquad \text{(Eq. 1)}$$

The solid iron gradually disappears and a gas is evolved. This can be seen with the naked eye. The solution in the above reaction is ionized and contains positively and negatively charged ions. The HCl contains hydrogen ions (H^+) and chloride ions (Cl^-).

Likewise, ferrous chloride ions in solution can be considered as iron ions (Fe^{2+}) and chloride ions (Cl^-). Therefore, Eq.1 can be written as the following:

$$Fe + 2H^+ + 2Cl^- \rightarrow Fe^{2+} + 2Cl^- + H_2 \qquad \text{(Eq.2)}$$

The iron converted to an iron with two positive charges. By definition, the iron is said to have been oxidized (loss of electrons). On the other hand, the hydrogen ions have each gained an electron. By definition, they have been reduced. The overall reaction can be considered as two separate ones:

$$\text{Oxidation:} \quad Fe \rightarrow Fe^{2+} + 2e^- \qquad \text{(Eq.3)}$$

$$\text{Reduction:} \quad 2H^+ + 2e^- \rightarrow H_2 \qquad \text{(Eq.4)}$$

Eq.3 and Eq.4 both take place on the surface of the metal. The areas where oxidation occurs are defined as anodes, and those where reduction takes place are defined as cathodes. The electrons produced in Eq.3 flow through the metal to the cathode areas to take part in the reaction of Eq.4. Hydrogen ions in the vicinity of the anode areas are not needed there, and they flow to the cathode to sustain the reduction reaction as shown in figure 1.9.

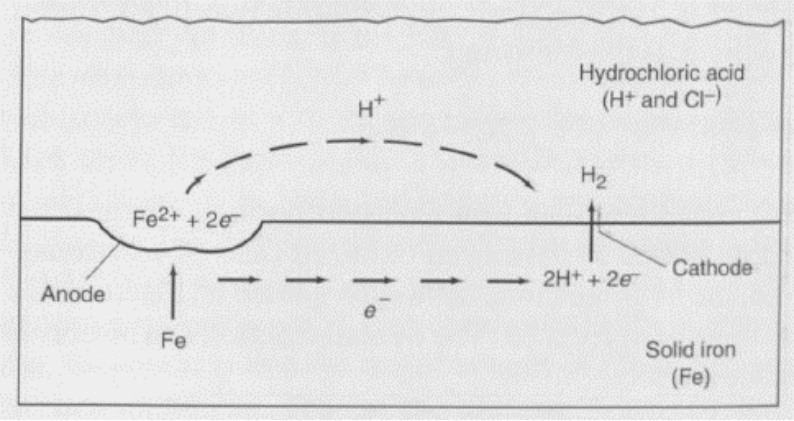

Figure 1.9: Corrosion of iron in hydrochloric acid. [23]

The corrosion reactions of other metals and corrodents are similar. In all cases of electrochemical corrosion, the anodic reaction consists of oxidation of the solid metal (M) to its ions in solution as follows:

$$M \rightarrow M^{n+} + ne^- \qquad \text{(Eq.5)}$$

1.3.4 Types of corrosion process

There are several types of corrosion, and they are based on identifying forms of corrosion by visual observations with either the naked eye or magnification. The common types of corrosion can be identified by their appearance of the corroded metal as follows.

1.3.4.1 Uniform corrosion

Uniform corrosion, which is also called general corrosion, corresponds to the corrosion attack with the greatest metal weight loss and is a common sight where steel structures are abandoned to rust as shown in figure 1.10. This corrosion is assumed to be most common form of corrosion and particularly responsible for most the materials loss. Traditionally, however it is not recognized as dangerous form of corrosion because the prediction of thickness reduction rate can be calculated by means of tests corresponding corrosion allowance, and using protection methods for preventing uniform corrosion on workpieces are usually so efficient, particularly in coating and cathodic protection [99].

Figure 1.10: Uniform corrosion occurs without protective coating. [5]

From a corrosion inspection point of view, uniform attack is relatively detectable and its effects are predictable; hence it is deemed to be less troublesome than other forms of corrosion unless the corroding material is hidden from sight. The internal corrosion of pipe line, for example, or the corrosion of hidden components and that of any other buried or immerged structures is a good example that even the simplest corrosion process needs to be monitored. Allowing for a corrosion allowance based on the possible loss of a material thickness is one of the simplest methods for dealing with uniform attack [80].

Designing in a system a corrosion allowance based on the possible loss of a material thickness is one of the simplest methods for dealing with uniform attack. Ultrasonic inspection has been used to measure the thickness of solid objects. A piezoelectric crystal serves as a transducer to oscillate at high frequencies, coupled directly or indirectly to one surface of the object whose thickness is to be measured. The thickness of the metal substrate is determined simply by the time of flight for the

ultrasonic signal to reach the back surface and return to the transducer measured using either signal T_2 or T_3 as illustrated in figure 1.11 [82].

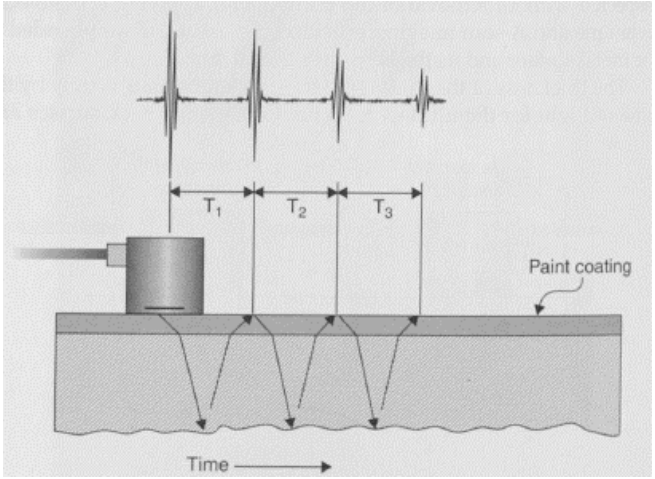

Figure 1.11: Thickness testing using longitudinal waves. [82]

1.3.4.1.1 Corrosion rate expressions and allowances

The term corrosion rate refers to the effect of uniform corrosion on a metal (or nonmetal) per unit of time. The type of corrosion rate expression used depends on the technical system and on the type of corrosion effect. Thus, corrosion rate can be expressed as (a) the mass of metal turned into corrosion products per unit area of surface per unit of time (weight loss), or (b) an increase in corrosion depth per unit time (penetration rate). The corrosion effect, which refers to a change in any part of the corrosion system (metal/environment combination), can vary with time and might not be the same at all points of the corroding surface. Reports of corrosion rates, therefore, should be accompanied by information on the type, time dependency, and location of the corrosion effect.

Weight-loss tests are the most common of all corrosion-test measurements for determining corrosion rates. A clean coupon is measured, weighed, exposed to the corrodent for a known time, removed, cleaned to remove corrosion products, and reweighed. The rate of metal removal due to corrosion is then calculated from [23]:

$$R = KW/ATd \quad \text{(Eq.6)}$$

Where R = Corrosion rate

K = Constant

W = Weight loss in (g)

A = Area to the nearest 0.01 cm^3

T = Time of exposure in hours to the nearest 0.01 hour

d = Density in g/cm^3

Many different units are used to express the corrosion rate (R). Using the preceding units for W, A, T, and d, the corrosion rate can be calculated in a variety of units with the appropriate value of K as listed in table 5.

Table 5: Constant number (K) calculated in different corrosion rate units. [23]

Corrosion rate units desired	Constant (K) in corrosion rate equation
Mils per year (mpy)	3.45×10^6
Inches per year (in./yr)	3.45×10^3
Inches per month (ipm)	2.87×10^2
Millimeters per year (mm/yr)	8.76×10^4
Micrometers per year (μm/yr)	8.76×10^7
Picometers per second (pm/s)	2.78×10^6

By knowing the expected general corrosion rate and the anticipated plant or service life of a part, the designer can calculate the extra wall thickness required for corrosion resistance of the process equipment being designed. After determining a wall thickness that meets mechanical requirements, such as pressure and weight of equipment, an extra thickness called a *corrosion allowance* is added to the wall thickness to compensate for the metal expected to be lost over the life of the equipment. Then, because the penetration depth can vary, a corrosion allowance is assigned a safety factor of 2 [82].

1.3.4.1.2 Prevention of uniform corrosion

Uniform corrosion can be prevented or reduced by proper materials selection, the use of coatings or inhibitors, or cathodic or anodic protection. These corrosion prevention methods can be used individually or in combination. Uniform corrosion is often treated by building a corrosion allowance into the structure. If the corrosion rate is 100 $\mu m/year$, then the addition of 500 μm to the thickness of metal will provide 5 years of operation.

The measure of uniform corrosion rate required for determination of the corrosion allowance is estimated from prior conditions in similar service, data presented in the corrosion literature, and experimental data determined from coupon exposure [23].

1.3.4.2 Pitting corrosion

Pitting corrosion as illustrated in figure 1.12 occurs under certain conditions, which leads to accelerated corrosion in specific areas rather than uniform corrosion throughout the workpiece. Such conditions include low concentrations of oxygen or high concentrations of chlorides that interfere with the alloy's ability to reform a passivating film. In the worst cases, most of the surface remains protected, but tiny fluctuations destroy the passive film in a few critical areas. Corrosion at these points is amplified and can cause pits.

Figure 1.12: Pitting corrosion. [21]

The highly localized form of corrosion is produced as sharply defined holes. These holes may be small or large in diameter, but in most cases, they are relatively small. Pits may be isolated from each other on the surface or so close together that they resemble a roughened surface. Variations in the cross-sectional shape of pits are shown in figure 1.13 [23].

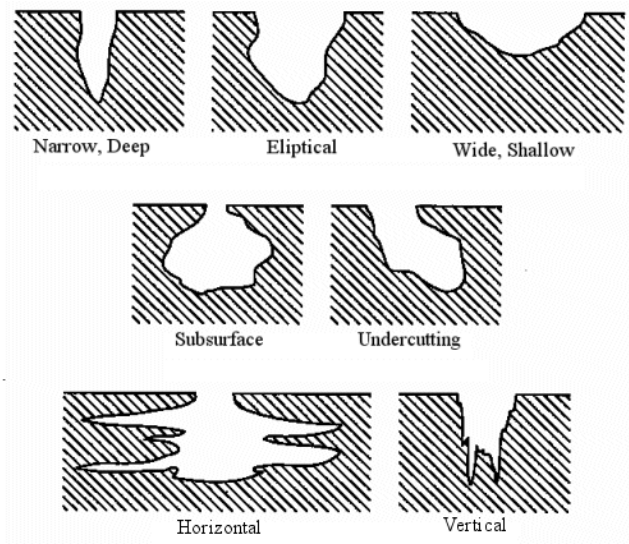

Figure 1.13: Variations in the cross-sectional shape of pits. [104]

Every engineering metal or alloy is susceptible to pitting. Pitting occurs when one area of a metal becomes anodic with respect to the rest of the surface or when highly localized changes in the corrodent in contact with the metal, as in crevices, cause accelerated localized attack.

Pitting corrosion can lead to unexpected catastrophic system failure. The split tubing in figure 1.14a was caused by pitting corrosion of stainless steel. A typical pit on this tubing is shown in figure 1.14b, and it also shows that pitting corrosion is quite small on the surface and very large below the surface.

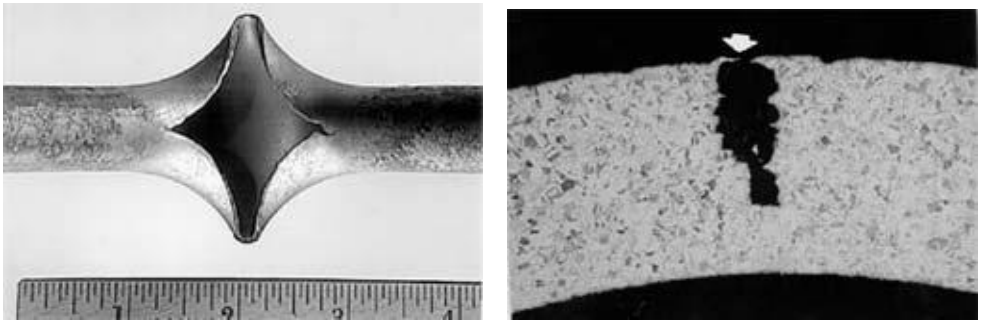

(a) *(b)*

Figure 1.14: Broken tubing by pitting corrosion (a), and cross section of a pit (b). [5]

1.3.4.2.1 Pitting initiation

An initial pit may form on the surface covered by a passive oxide film as a result of the following [41]:

- Mechanical damage of the passive film was caused by scratches. Anodic reaction starts on the metal surface exposed to the electrolyte. The passivity surrounding surface is act as the cathode.
- Particles of a second phase emerging on the metal surface. These particles precipitation along the grains boundaries may function as local anodes causing localized galvanic corrosion and formation of initial pits.
- Localized stresses in form of dislocations emerging on the surface may become anodes and initiate pits.
- Non-homogeneous environment may dissolve the passive film at certain locations where initial form.

1.3.4.2.2 Pitting growth

In presence of chloride ions pits are growing by autocatalytic mechanism. Pitting corrosion of a stainless steel is illustrated in the in figure 1.15a. The actual pitting corrosion phenomenon is shown on propeller shaft of high speed craft, and the pit depth was measured with dial gauge as shown in figure 1.15b.

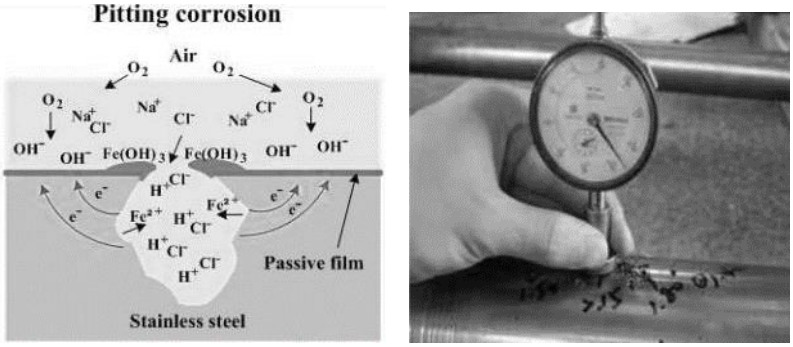

(a) *(b)*

Figure 1.15: Pitting corrosion, (a) pitting corrosion deep growth, (b) Measuring depth of pitting deep. [88]

1.3.4.2.3 Prevention of pitting corrosion

Typical approaches to minimizing pitting corrosion include the following [23]:

- Reduce the aggressiveness of the environment, for example, chloride ions concentration, temperature, acidity, and oxidizing agents.
- Upgrade the materials of construction, for example, use molybdenum containing (4 to 6% Mo) stainless steels, molybdenum + tungsten nickel-base alloys, over-alloy welds, and use corrosion-resistant alloy linings.

- Modify the design of the system, for example, avoid crevices and the formation of deposits, circulate/stir to eliminate stagnant solutions, and ensure proper drainage.

1.3.4.3 Crevice corrosion

In the past, crevice corrosion was used to describe only the attack upon oxide-passivated alloys by aggressive ions such as chloride in crevices or other shielded areas of a metal surface. Attack in similar circumstances upon non-passivated metals was called differential-aeration corrosion. Current practice has tended to neglect such distinctions, and consequently crevice corrosion has been given many other names. Differential-aeration and concentration cell corrosion are terms which arise because of aspects of the mechanism of corrosion in crevices. A good general definition of crevice corrosion is "the attack which occurs because part of a metal surface is in a shielded or restricted environment, compared to the rest of the metal which is exposed to a large volume of electrolyte" [96].

Crevice corrosion as shown in figure 1.16 is a localized form of corrosion usually associated with a solution on confined spaces (crevices) for example in nuts and rivet heads. When dust, sand and other corrosive substances are deposited on surfaces, they create an environment where water will accumulate and corrode the part. It can happen between two metals or between a metal and a nonmetal. This causes damage to the metallic part, which is initiated by the concentration gradient in chemicals [20].

Figure 1.16: Crevice corrosion on steel flange exposed to a chloride medium. [93]

1.3.4.3.1 Crevice corrosion propagation

The propagation of crevice corrosion is thought to involve the dissolution of metal and the maintenance of a high degree of acidity within the crevice solution by hydrolysis

of the dissolved metal ions [31]. The crevice corrosion propagation process is illustrated schematically in figure 1.17 for stainless steel corroding in a neutral aerated sodium chloride solution. The anodic metal dissolution reaction within the crevice, $M \rightarrow M^{n+} + ne^{-}$, is balanced by the cathodic reaction on the adjacent surface, $O_2 + 2H_2O + 4e^{-} \rightarrow 4OH^{-}$. The increased concentration of M^{+} within the crevice results in the influx of chloride ions (Cl^{-}) to maintain neutrality. The metal chloride formed, $M^{+}Cl^{-}$, is hydrolyzed by water to the hydroxide and free acid. The acid produced by the hydrolysis reaction keeps the pH to values below 2, while the pH of the solution outside the crevice remains neutral (pH7). In simple terms, the electrolyte present within an actively corroding crevice can be regarded as concentrated hydrochloric acid containing metal chlorides dissolved at concentrations near saturation [23].

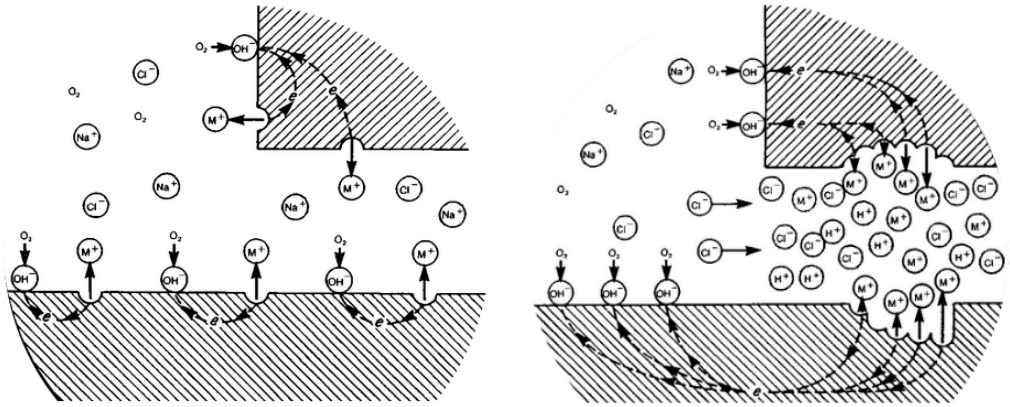

(a) *(b)*

Figure 1.17: The mechanism of crevice corrosion. (a) Initial conditions: corrosion occurs over the whole of the metal surface. (b) final conditions: metal dissolution occurs only inside the crevice where acidity increase, concentration of chloride ion increases, and the reaction becomes self-sustaining. [31]

Crevice corrosion is a very similar mechanism to pitting corrosion. It can be viewed as a less severe form of localized corrosion when compared with pitting. The depth of penetration and the rate of propagation in pitting corrosion are generally significantly greater than in crevice corrosion.

1.3.4.3.2 Prevention of crevice corrosion

Many of the factors must be considered if crevice corrosion is to be eliminated. Wherever possible, crevices should be minimized at the design stage. When unavoidable,

they should be kept as open and shallow as possible to allow continued entry of the bulk environment [23].

- As with pitting corrosion, a common way to protect against crevice corrosion is to select more corrosion-resistant materials (e.g., molybdenum containing, more highly alloyed stainless steels and nickel-base alloys). Welds overlays can also be employed.
- The influence of gasket material on nonmetal-to-stainless steel crevice formation should also be considered. Natural and synthetic elastomer type gaskets are less likely to promote crevice corrosion than polytetrafluoroethylene (PTFE) gaskets (with or without glass fiber) and para-aramid fiber + nitrile binder-type gaskets. While carbon and graphite-containing gaskets promote crevice, PTFE and para-aramid + nitrile promote even greater attack.
- Cleanliness is an important factor, particularly when conditions promote deposition on metal surfaces. Regular cleaning involving mechanical methods is commonly employed. Filters can also be employed to remove materials that can deposit on the metal surface. It is very important to try to avoid using hydrochloric acid to clean stainless steel systems. Chloride will concentrate in preexisting crevices during cleaning and may not be removed subsequently.

1.3.4.4 Galvanic corrosion

Galvanic corrosion (also called dissimilar corrosion or wrongly electrolysis) as shown in figure 1.18 refers to corrosion damage induced when two dissimilar materials are electrically coupled while in contact with an electrolyte. In this corrosion cell, the less noble material becomes the anode and tends to be corroded while the more noble material supports a cathodic reaction. For galvanic corrosion to occur, these conditions must be present; 1) electrochemically dissimilar metals must be present, 2) these metals must be in electrical contact, and 3) the metals must be exposed to an electrolyte [86].

Figure 1.18: Galvanic corrosion of stainless steel plate connected with carbon steel structure. [40]

Metallic materials in electrochemical contact can form a galvanic cell as illustrated in figure 1.19. In a galvanic cell, when two metals with different electrical potentials are connected, there is a potential difference across them. The metal with the higher electrical potential becomes the anode, and the metal with lower potential becomes the cathode. The anode dissolves or corrodes to form ions. These ions drift into the solution with other ions in the electrolyte.

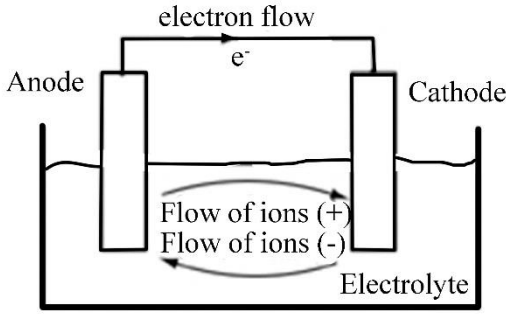

Figure 1.19: Galvanic cell. [40]

A very important factor to consider in galvanic corrosion is the area effect or the ratio of cathodic to anodic area. For example, stainless steel and copper tubes are routinely joined without causing problems, but accelerated corrosion of the copper tube is likely to occur when attached to a stainless-steel tank. The role of the surface area ratio between local anodes and cathodes origins from the simple fact that there is no possible net accumulation of charges during corrosion processes. When a piece of metal is freely corroding, the electrons generated at anodic areas flow through the metal to react at cathodic areas similarly exposed to the environment where they restore the electrical balance of the system. However, the absolute equality between the anodic and cathodic currents expressed in Eq.7 does not mean that the current densities for these currents are equal.

$$I_{anodic} = I_{cathodic} \quad \text{(Eq.7)}$$

When Eq.7 is expressed in terms of current densities in Eq.8 by considering the relative anodic (S_a) and cathodic (S_c) surface areas and their associated current densities i_a and i_c expressed in units of mA/cm^2, for example, it becomes clear that a difference in the surface areas occupied by each reaction will have to be compensated by inequalities in the current densities as expressed in Eq.9

$$I_{anodic} = i_a \times S_a = I_{cathodic} = i_x \times S_c \quad \text{(Eq.8)}$$

$$i_a = i_c \frac{S_c}{S_a} \quad \text{(Eq.9)}$$

The surface area ratio express in Eq.9 indicates that an anodic current may be greatly amplified when S_c/S_a is much greater than one (figure 1.20a) and stifled when it is much smaller than one (figure 1.20b). It is easy to understand that the effect of a certain amount of anodic current concentrate on a small area of metal surface will be much greater than when the effect of the same amount of current is dissipated over a much larger area [80].

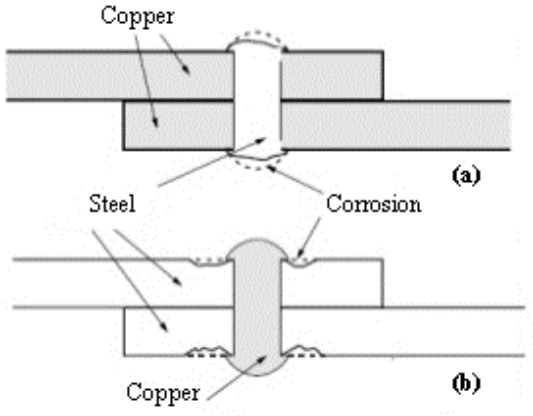

Figure 1.20: Galvanic coupling caused by riveting with dissimilar metal: (a) steel rivets on copper plates and (b) copper rivets on steel plates. [80]

1.3.4.4.1 Factors influencing galvanic corrosion behavior

Area effects – In galvanic corrosion involve the ratio of the surface area of the more noble to the more active members. When the surface area of the more noble metal or alloy is large in comparison to the more active member, an unfavorable area ratio exists for the prevailing situation in which a couple is under cathodic control. The anodic current density on the more active metal or alloy is extremely large; therefore, the resulting polarization leads to more pronounced galvanic corrosion. The opposite area ratio-large

active member surface, smaller noble member surface-produces only slightly accelerated galvanic effects because of the predominant polarization of the more noble material.

Effect of distance – Dissimilar metals in a galvanic couple that are in close physical proximity usually suffer greater galvanic effects than those that are farther apart. The distance effect is dependent on solution conductivity because the path of current flow is the primary consideration. Thus, if dissimilar pipes are butt welded with the electrolyte flowing through them, the most severe corrosion will occur adjacent to the weld on the anodic member.

Effect of geometry – The geometry of the circuit also enters into the effect to the extent that current will not readily flow around corners. This is simply an extension, in which the current takes the path of least resistance [23].

1.3.4.4.2 Prevention of galvanic corrosion

There are a number of ways that galvanic corrosion may be prevented. These can be used singly or in combination. All of these preventive measures follow directly from the basic mechanism of galvanic corrosion [82].

- Avoid the use of dissimilar metals wherever possible. If this is not practical, try to use metals which are close together in the galvanic series.
- Avoid an unfavorable area ratio whenever possible, particularly in the presence of an electrolytically conductive environment.
- If dissimilar metals are used, insulate these electrically from one another.
- If it is necessary to use dissimilar metals, and these cannot be insulated, then the more anodic part should be designed for easy replacement or should be constructed of thick materials to longer absorb the effects of corrosion.
- Coat the cathode (or both anode and cathode) near the junction to reduce the effective cathodic area. Never coat the anode alone since any pinhole would be the site of rapid anodic attack due to the large S_c/S_a surface area ratio.

1.3.4.5 Corrosion Fatigue

Corrosion fatigue is a term that is used to describe the phenomenon of cracking, including both initiation and propagation, in materials under the combined actions of a fluctuating, or cyclic stress, and a corrosive environment. Corrosion fatigue depends strongly on the interactions between the mechanical (loading), metallurgical, and environmental variables listed in table 6.

Table 6: Mechanical, metallurgical, and environmental variables influencing corrosion fatigue behavior. [23]

Variable	Type
Mechanical	Cyclic loading frequency
	Residual stress
	Crack size and shape, and their relation to component geometry
	Load interactions in variable-amplitude loading
Metallurgical	Alloy composition
	Distribution of alloying elements and impurities
	Microstructure and crystal structure
	Mechanical properties (strength, fracture toughness, etc)
Environmental	Types of environment: gaseous, liquid, liquid metal, etc.
	Electrical potential
	Temperature and pH
	Viscosity of the environment

Corrosion fatigue produces fine-to-broad cracks with little or no branching; thus, they differ from stress-corrosion cracks, which often exhibit considerable branching. They are typically filled with dense corrosion product as shown in figure 1.21. The cracks may occur singly but commonly appear as families or parallel cracks. They are frequently associated with pits, grooves, or some other form of stress concentrator.

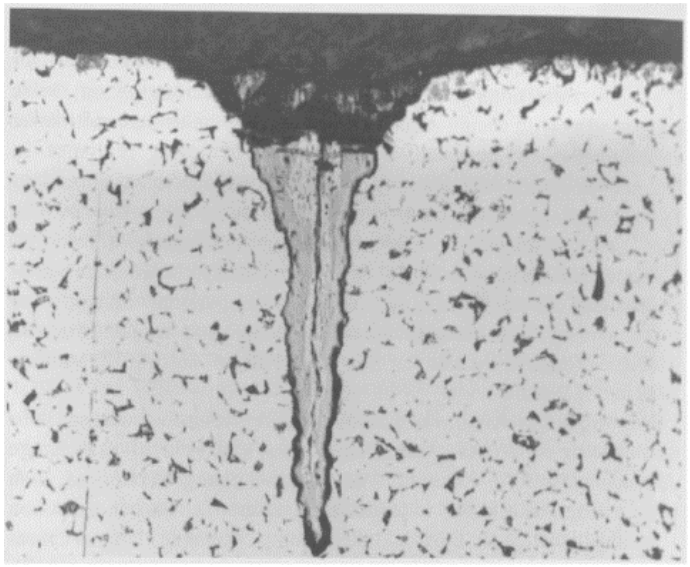

Figure 1.21: Wedge-shaped corrosion fatigue crack filled with corrosion product. [23]

1.3.4.5.1 Prevention of corrosion fatigue

All metals and alloys are susceptible to corrosion fatigue. Even some alloys that are immune to SCC, for example, ferritic stainless steels, are subject to failure by corrosion fatigue. Both temporary and permanent solutions for corrosion involve in following [19];

- Minimizing or eliminating cyclic stresses.
- Selecting a material or heat treatment with higher corrosion fatigue strengths.
- Reducing stress concentration or redistribute stress.
- Eliminating corrosion, or a combination of these procedures.
- Avoiding notches, accidental dents and rough surface finish.

1.3.5 Corrosion testing in simulators

Modern controls of quality and degradation in material research is necessary to check the effect of corrosion on material and product. Corrosion testing of materials in the accelerated laboratory test is the greatest advantage that researcher gets a quick result of the corrosion of the test specimens. Basically, Specific types of laboratory test in corrosion excluding electrochemical tests can be grouped into three categories:

1.3.5.1 Simulated atmosphere test

In simulated atmosphere test, wetting of the surface of test sample by condensing media in humid atmospheres is performed in closed cabinets (humidity-temperature chambers) under a variety of conditions ranging in temperature from freezing to 65 ‘C and in relative humidity from 20 to 100% as displayed in figure 1.22. The standard test procedure is to dry the samples and visually inspect them after a certain period (cycle), after which the test is repeated several time [23].

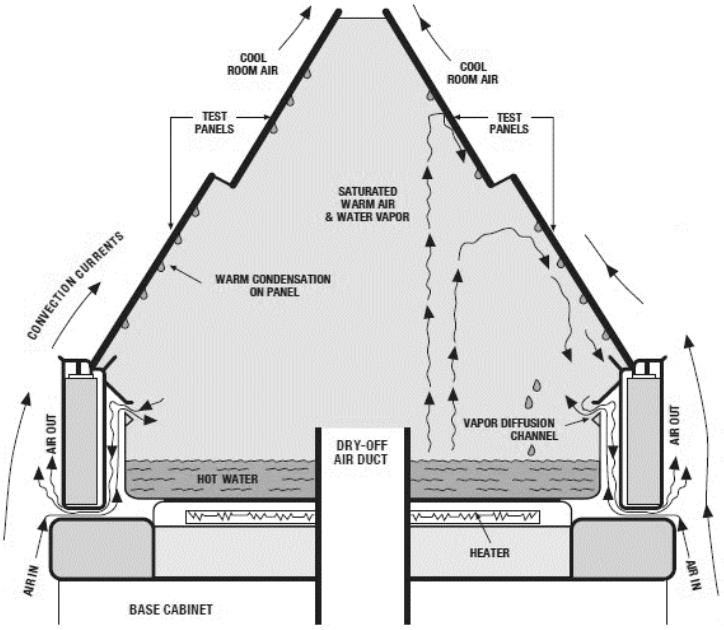

Figure 1.22: Cross section of simulated atmosphere tester. [81]

From figure 1.22, the water in the bottom of the test chamber is heated to generate hot vapor. The vapor mixes with air and fills the chamber, creating specific relative humidity. Because the test panels are the actual roof of the test chamber, the panels are cooled down by the room air on the outer sides. The resulting temperature difference causes the vapor to condense on the underside of the panels. Condensation occurs first as microscopic droplets. They coalesce into larger and larger drops until they finally run off. Under constant conditions, this droplet cycle will repeat, and constant condensation develops strong osmotic pressure across a coating, tending to pull pressure into the coating. Drying off the test specimen relieves this pressure. These dry-off periods are representative of many service conditions. Transition back and forth from wet to dry is very important. When a material is dry, very little deterioration occurs. A drying time of one to two hours is usually enough for cyclic operation [81].

1.3.5.2 Salt spray testing

The neutral salt spray (fog) test, spraying of aggressive media on test sample is implemented in order to determine the corrodibility of nonferrous and ferrous metal. The salt spray (fog) test is considered to be most useful as an accelerated laboratory corrosion test. This method describes the spraying of a 5% sodium chloride (NaCl) solution in the chamber at 35’C or 50 ‘C. The duration of this test can range from 8 to 3000 h, depending on the product type of coating. Acetic acid or copper chloride can be added to the NaCl solution to accelerate the reaction. The fine salt for condenses on the test samples and

initiates corrosion on test samples [58]. Typical salt spray chamber are shown in figure 1.23.

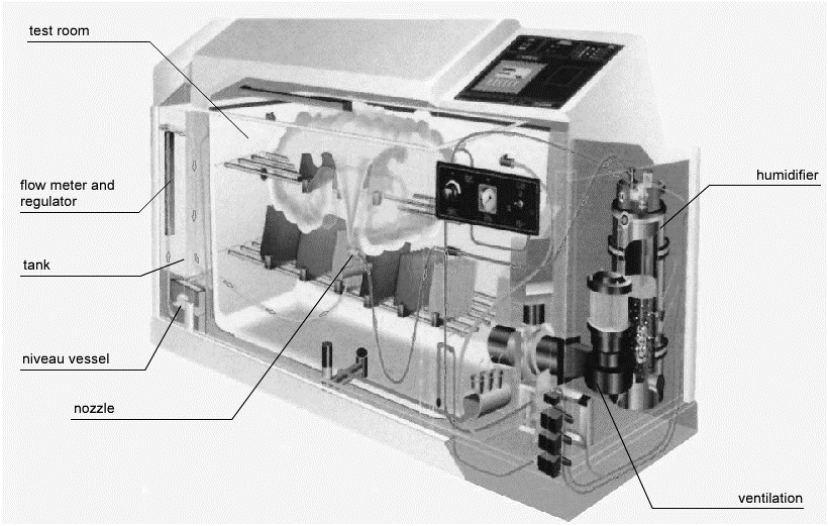

Figure 1.23: Common example of top-opening salt spray chamber. [26]

The apparatus for testing consists of a closed testing chamber, where a salt water (5% NaCl) solution is atomized by means of spray nozzles using humidified compressed air sucking the test solution from a constant level vessel. The fine salt fog is distributed evenly in the chamber by ventilation system that is used for ventilating, drying and cooling down of the test chamber and test samples. This produces a corrosive environment of dense salt water fog in the chamber, so that test samples exposed to this environment are subjected to severely corrosive conditions.

The acetic acid salt spray test, this simulator is also used for testing inorganic and organic coatings, but is particularly applicable to the study or testing of decorative chromium plate (nickel-chromium or copper-nickel-chromium) plating and cadmium plating on steel or zinc die-castings and for the evaluation of the quality of a product. This test can be as brief as 16 hours, although it normally ranges from 144 to 240 hours or more. As in the neutral salt spray test, 5% NaCl solution is used, but the solution is adjusted to a pH range of 3.1 to 3.3 by the addition of acetic acid, and again, the temperature of the salt spray cabinet is controlled to maintain 35+1.1 or -1.7 °C within the exposure zone of the closed cabinet [78].

The copper-accelerated acetic acid-salt spray test, this test which is also called CASS is primarily used for the rapid testing of decorative copper-nickel-chromium or nickel-chromium plating on steel and zinc die-castings. It is also useful in the testing of anodized, chromated, or phosphate aluminum. The duration of this test ranges from 6 to

720 hours. A 5% NaCl solution is used, with 1 g of copper II chloride ($CuCl_2$-$2H_2O$) added to each 3.8 L of salt solution. The solution is then adjusted to a pH range of 3.1 to 3.3 by adding acetic acid. The temperature of the CASS cabinet is controlled to maintain 49+1.1 or -1.7°C within the exposure zone of the closed cabinet [23].

1.3.5.3 Immersion tests

Immersion tests is the process of immersing the test sample into corrosive liquid directly. It can be divided into three types: total immersion, partial immersion, and alternate immersion. The type of test selected is determined mostly by the environmental conditions that must be simulated. Obvious differences in test procedures are the solutions used, agitation rates, and temperature. The environmental conditions that must be simulated and the degree of acceleration that is required often determine the choice of a laboratory test. In immersion testing, acceleration is achieved principally by [80].

- Lengthening the exposure to the critical conditions that are suspected to cause corrosion damage. For example, if a vessel is to be batch-processed with a chemical for 24 hours, laboratory corrosion exposure of 240 hours should be considered.
- By intensifying the conditions in order to increase corrosion rates, i.e., increasing solution acidity, salt concentration, temperature or pressure, etc.
- By provoking localized environmental changes that can result in the formation of acidic/high chloride conditions furthering the initiation and propagation of crevice corrosion of susceptible alloy.

One the environmental conditions have been determined and the test designed, it should be repeated a sufficient number of times to determine whether it meets the desired standard for reproducibility. Immersion tests can be divided into three categories [23].

1. Simple immersion tests. In these tests, small sections of the candidate material are exposed to the test medium and the loss of weight of the material is measured for a period of time. Immersion testing is a powerful method of screening and eliminating from further consideration those materials that should not be considered for specific applications. However, while these tests are quick and economical means for providing a preliminary selection of best suited materials, there is no simple way to extrapolate the results obtained from these simple tests to the prediction of system lifetime.

2. Alternative immersion tests. Another variation of the immersion test is the cyclic tests in which a test specimen is immersed for a period of time in a test environment, then removed and dried before being re-immersed to continue the cycle. Normally hundreds of these cycles have to be completed during the course of a test program. This condition is of practical importance because they simulate, for instance, the effects of the rise and fall of tidal water and the movements of corrosive liquids in chemical plants.

3. Immersion tests under load. The study of environmentally assisted cracking in its most basic sense involves the consideration and evaluation of the inherent compatibility between a material and the environment under conditions of either applied or residual stress. This is a very broad topic encompassing many possible combinations of materials and environments.

1.4 Welding of dissimilar materials

The joining of dissimilar materials requires precise knowledge of the properties of each material. When joining two dissimilar materials under the influence of heat, the intermetallic phase is created at the interface between the two materials. The more heat that is applied, the more extensive the intermetallic phase and the poorer the mechanical properties of the join will be. The different thermal expansion coefficients of the two materials create a stress field around the join. There is also a marked tendency for corrosion to form as a result of the large electrochemical potential difference of these materials.

1.4.1 Cold metal transfer welding

Extensive research in the field of welding processes indicated that arc welding was indeed a potential way of joining the two materials. Therefore, in 2004, Cold metal transfer (CMT) welding process was developed from the continuous adaptation of the pulsed metal inert gas welding (MIG) to resolve the problems posed by the joining of dissimilar materials, for example, welding steel with aluminum sheets [11].

CMT is completely new technology with respect to both welding application and welding equipment. CMT is not only completely new technology, but it also enhances pulsed metal inert gas welding (MIG) application areas, allowing the arc joining of steel to aluminum in a reproducible manner for the first time. CMT can be described as a Gas Metal Arc Welding (GMAW) process where heat input is low compared to the

conventional dip arc process [11]. In the CMT process the wire is not only pushed towards but also drawn back from the work piece and oscillating wire feeding with an average oscillation frequency up to 70 Hz is used [84].

1.4.2 Cold metal transfer welding operation

The CMT process provides many advantages points in welding technology, for example, assisting droplet detachment by means of the wire-motions incorporated in the digital process-control, reducing the thermal input by achieving almost current-free metal transfer, ensuring spatter-free metal transfer by controlling the short circuiting and welding of dissimilar materials as well as ultra-light gauge sheets from 0.3 mm. Typically, CMT system configuration consists of power source, remote-controlling unit, cooling unit, robot interface, wire feeder, welding torch, wire buffer and wire supply as depicted in figure 1.24.

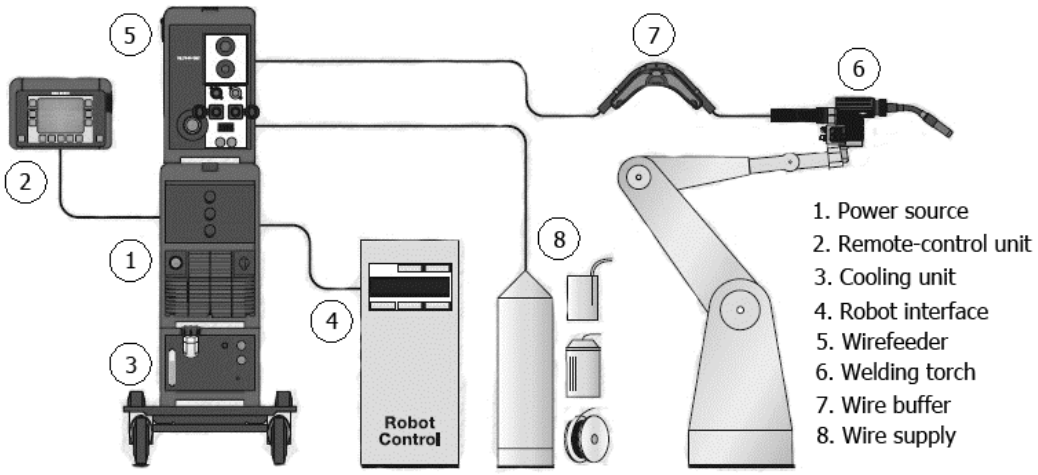

Figure 1.24: The components of CMT welding machine. [18]

Figure 1.25 illustrates the CMT arcing process, in this process, firstly, the filler metal is moved towards the weld pool (figure 1.25a, hot phase). When the filler metal dips into the weld-pool, the arc is extinguished and the welding current is lowered (figure 1.25b, cold phase). Afterwards, the backward movement of the wire assists droplet detachment during the short circuit and the short circuit current is kept small (figure 1.25c, cold phase). Finally, the wire motion is reversed and the process begins all over again (figure 1.25d, hot phase) [34].

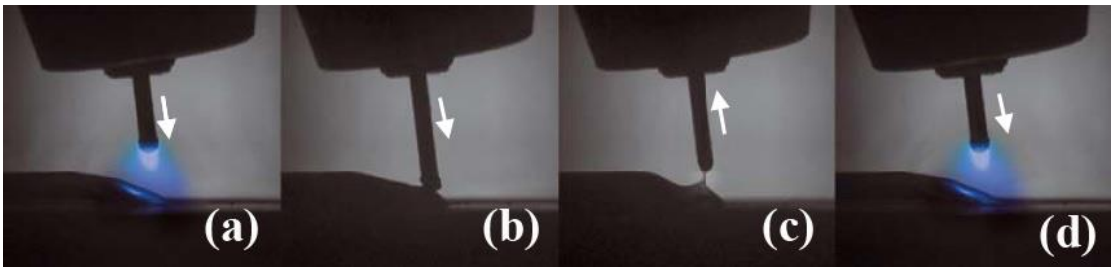

Figure 1.25: Movement of filler material during CMT arcing process. [34]

The important function of CMT process is controlling the motions of filler material, and this makes it possible to reduce the amount of heat during welding process. The reduced thermal input provides advantages such as low distortion and higher precision. Benefits include a higher-quality of welded, lower cost for rejection and post-weld machining, freedom from spatter as well as the ability to join both steel to aluminum and galvanized sheet. Figure 1.26 shows the welded steel and aluminum sheets by using CMT process [77].

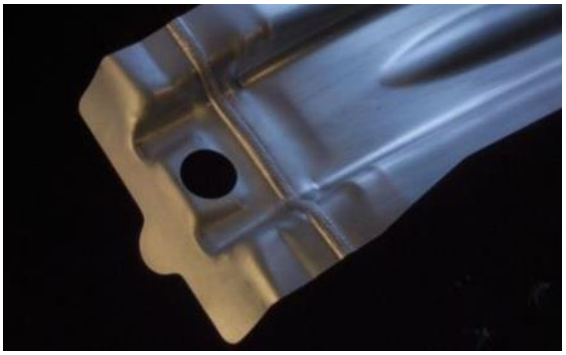

Figure 1.26: A workpiece after welded by CMT process. [29]

A general CMT weld cycle is shown in figure 1.27. It is described as the period required to deposit a droplet of molten electrode into the weld pool, and consists of two distinct phases of operation [79]:

Arcing phase. This is represented by a constant arc voltage which ignites the welding arc and heats both the workpiece and the wire electrode. The current is then reduced in order that droplet detachment is not initiated, but a molten globule remains attached to the end of the electrode and a weld pool is created.

Short circuit phase (S/C). The electrode is fed into the weld pool initiating an electrical short circuit represented by a reduction in arc voltage. The point of short circuit is sensed and the welding current is reduced to a minimum extinguishing the welding arc and limiting the thermal energy transferred to the workpiece. After a defined duration the

electrode is retracted pinching the molten droplet into the weld pool and breaking the short circuit. The arc is then reignited and the cycle repeats.

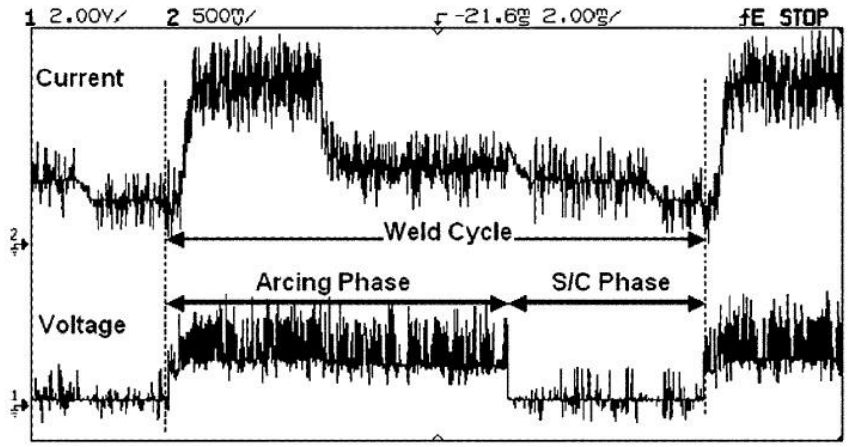

Figure 1.27: Electrical cycle of CMT welding process. [79]

Setting up the parameters of CMT process before start welding on a workpiece is very important to get the high quality of weldment. Normally, the welding quality can be inspected from the weld penetration, deposition rate and bead geometry of welded workpiece. This welding quality is usually affected by many CMT parameters consisting of welding current, arc voltage, travel speed, electrode extension, torch angle, and electrode diameter [6]. Therefore, controlling these parameters are necessary to consistently produce welds of acceptable quality. The effects of these parameters on deposit distribution is shown in table 7.

Table 7: Effect of changes in parameters on weld geometry. [6]

Welding parameters	**Effects of weld geometry**					
	Penetration		**Deposition rate**		**Bead size**	
	Increase	**Decrease**	**Increase**	**Decrease**	**Increase**	**Decrease**
Welding current	I	D	I	D	I	D
Arc voltage	NE	NE	LE	LE	LE	LE
Travel speed	NE	NO	LE	LE	D	I
Electrode extension	D	I	I	D	I	D
Electrode diameter	D	I	D	I	LE	LE

(I=increase, D=decrease, NE=No effect, LE=litter effect)

1.4.3 Joining dissimilar materials using CMT

Welding dissimilar materials is obviously more difficult than welding the same material or alloys with minor differences in composition. However, welding dissimilar materials has a lot of advantage points in development of structure, automotive and aerospace engineering. Thus, recently, many researches in welding various materials using CMT have been reported in following.

Examining the CMT joint between aluminum alloys and galvanized steel was reported by Cao R. et al. (2013). In this research, 1 mm thick aluminum alloys were joined to 1 mm thick mild steels as lap-shear joint by CMT welding. Various aluminum wires of 1.2 mm diameter were utilized as filler material. To reduce the formation of Fe-Al intermetallics in weld metal, they found that the optimum setting for welding of these aluminum-galvanized steel could be provided with an Al4043 wire, 100% argon shielding gas, a welding voltage of 12-14V, a deviation distance of 2-3.5 mm, a welding speed of 6-8 mm/s and a wire-feed speed of 4-6 m/min. Furthermore, the result was mentioned that the strength of aluminum galvanized steel-welded joint depends on the thickness of the intermetallics and softening of the aluminum heat affected zone.

Investigating cold metal transfer welding-brazing of titanium to copper was carried out by Cao R. et al. (2014) 3 mm pure titanium was welded with 3 mm pure copper by Cold Metal Transfer (CMT) welding with a 1.2 mm ERCuNiAl copper wire. In methodology, the three different shapes of Cu/Ti butt joints with various welding speed levels were tested. The effect of dissimilar groove angles of Cu side and wire feed speeds during weld process and mechanical properties of the joint were examined. Their results indicated the welding joint was formed at Cu all side, while brazing joint was formed in titanium alloy side. At the optimized welding configuration, the types of groove of Cu-Ti brazing interface had no effects on the mechanical properties of the joint and the Cu/Ti CMT butt joints at the optimized welding variables had the rupture point at Cu heat affected area (HAZ).

Weldment of AA6061 Al alloy and galvanized steel using cold metal transfer spot plug welding with aluminum 4043 as filler metal was performed by Cao R. et al. (2014). Mechanical testing of CMT spot plug welded joints was conducted. It was found that the strength of CMT spot welded AA6061-to-galvanized steel was determined primarily by the strength and area of the brazed interface. While, the strength of the galvanized steel-to-Al AA6061 joint was mainly dependent upon the area of weld metal. Therefore,

strength of CMT spot plug welded AA6061 to galvanized mild steel was significant stronger than that of CMT spot plug welded galvanized steel to AA6061 Al alloy. In short, it was recommended to choose the stacking sequence that the AA6061 Al alloy sheet was placed on the top of the steel.

Beytullah G. et al. (2014) used Pulsed Robotic Cold Metal Transfer (CMT) to weld both similar and dissimilar aluminum alloy plates with a thickness of 6 mm. Afterward, mechanical testing as destructive method such as tensile, bending, fatigue and microhardness tests were employed to characterize the mechanical properties of each welded joint. To examine the surface deformations of specimens, light optical microscopy (LOM) and scanning electron microscopy (SEM) were adopted. According to this results, CMT Pulse displayed higher welding speed and very low heat input as well as higher yield strength values than other welding methods previously reported in their literatures. Also, microhardness results for all welded joints were similar to characteristic hardness traverse across weldments, hardness drops were slightly close to the base metal.

Studying in the parametric effects of cold metal transfer welding on the microstructural aspects in AA6061 was performed by Kumar N.P. et al. (2016). The effect of welding current and welding speed on heat input and the geometry of weld bead was reported interestingly. According to their results, Pulsed-CMT showed a stable and spatter-free welding of aluminum alloy when current is maintained in 60-70 A and welding speed of 8-10 mm/s. For using filler material to weld aluminum alloy sheets, the author mentioned the filler material which was same composition of its base metals was better to prevent cracking, narrow heat affected zone and reduce intermetallic phase area on welded joints.

1.5 Non-destructive testing

Non-destructive testing, or NDT, is the use of noninvasive techniques to evaluate the integrity of a material, component or structure; or to quantitatively measure some characteristic of an object. In other words, NDT involves inspecting or measuring without harming the future usefulness of an object. Some NDT methods, such as X-ray and ultrasonic inspection, are familiar due to their use in the medical industry. Manufacturers widely use NDT to inspect incoming materials, to control manufacturing processes, to verify proper processing and assembly, and to inspect for in-service damage. The Main NDT method currently using can be listed as follows.

1.5.1 Visual inspection

Visual inspection (VI) is one of the most common and most powerful means of non-destructive testing. VI is also used to identify the bad condition of specimens before other more expensive or time-consuming forms of inspection are performed. Moreover, it is easy to apply, quick, and relatively inexpensive. VI requires adequate illumination of the test surface and proper eye-sight of the tester. To be most effective visual inspection does however, merit special attention because it requires training (knowledge of product and process, anticipated service conditions, acceptance criteria and record keeping) and it has its own range of equipment and instrumentation. Visual inspection can be classified as direct visual testing and remote visual testing (RVT) [4]. Often the direct visual testing equipment is showed in figure 1.28.

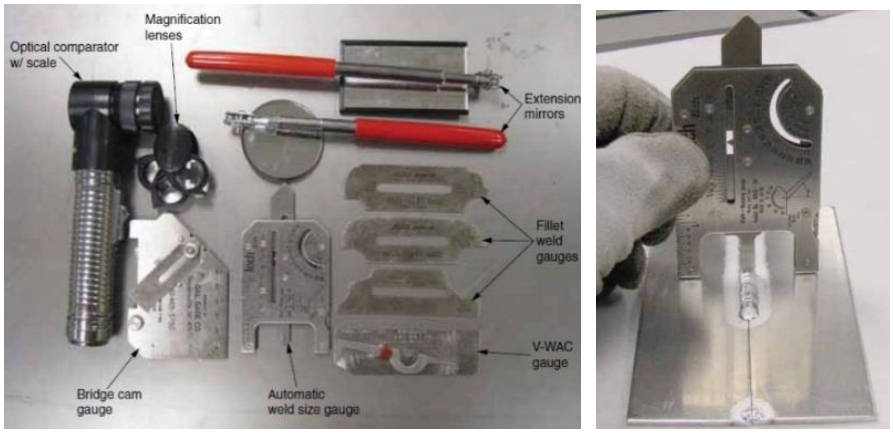

(a) *(b)*

Figure 1.28: Direct visual testing kit for weldment inspection. [37]
(a) visual testing kit (b) crown gauge is used to check the height of the weld bead.

Figure 1.29 shows remote visual testing equipment that is a cost-effective inspection technique used to capture real-time views and images from inside tubes, pipes, rotating machinery, engines, heat exchangers, refractory-lined vessels and enclosed structures that are difficult to monitor the condition of specimens by using other methods [43].

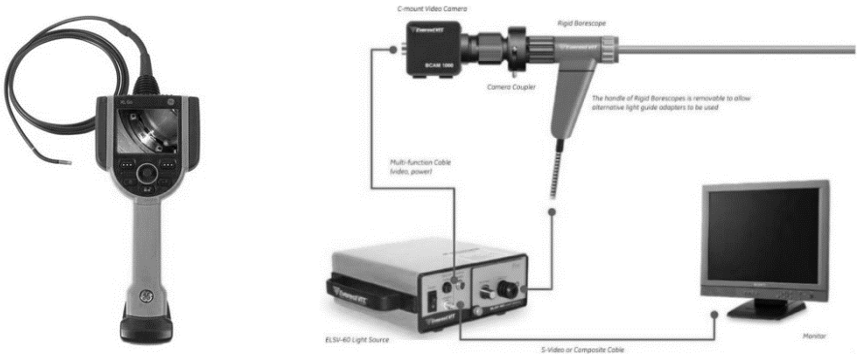

(a) Flexible borescopes *(b) Rigid borescopes*

Figure 1.29: Remote visual testing equipment. [24]

1.5.2 Penetrant testing

One of the most common ways to enhance visual testing (VT) is through the introduction of highly visible penetrating liquids. These specially prepared liquids, characterized by low a viscosity, easily enter voids open to the surface when the part is dipped into or sprayed by the penetrant. Relatively simple, inexpensive and reliable, liquid penetrant testing (PT) is only used for detecting discontinuities open to the surface. With the correct application, it will detect discontinuities ranging in size from the large to the microscopic. This Non-Destructive Testing Method involves applying a liquid to the surface of a material and leaving it to rest for a pre-determined period of time. The liquid can be either a color that is easily visible under normal lighting conditions or a yellow/green fluorescent color that requires special lighting conditions to be effective. During the liquid penetrant testing, the liquid dye enters into discontinuities that are open to the surface of the material through a phenomenon known as ‘capillary action’. This capillary action takes place through the resting time and the discontinuity retains this dye when the excess is cleaned from the surface. A certain type of developer is then applied to the surface of the material and the dye that is trapped inside the surface discontinuities is blotted back out on to the surface and forms an indication. This indication is then interpreted by a qualified interpreter. The liquid penetrant testing method, also known as dye penetrant examination is suitable on most non-absorbent materials [94].

Liquid penetrant inspections are the simplest, most effective way to verify and identify open to the surface discontinuities. Penetrants can be used on almost any material, such as plastic, glass, ceramics, carbon steels, stainless steels, aluminum, exotic alloys, etc.

The particular penetrant liquid, usually a red dye or a fluorescent dye when using a black light, is applied to generally non-ferrous materials. It is also advantageous to use a low sulphur and hallogen dye. The area to be tested must be clean. The dye is applied and left for approximately 1/2 hour or longer on the surface which enables the dye to be drawn by capillary action, into a surface breaking indication. The excess dye is removed by either water or solvent soaked cloth and developer is applied, a further waiting period of up to approximately 15 minutes or longer is required where the colored dye will contrast with the white developer enabling the technician to identify any discontinuities. The process is illustrated in figure1.30.

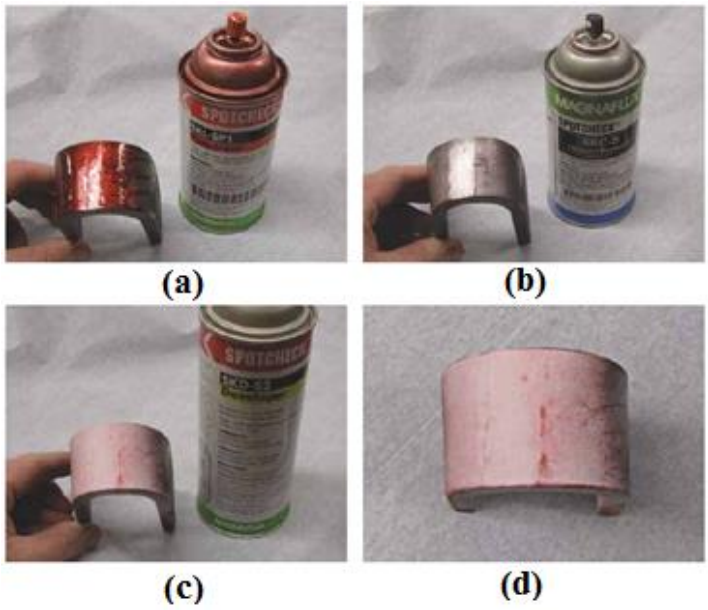

Figure 1.30: Penetrant testing (a) apply dye developer, (b) remove excess dye penetrant with remover, (c) apply developer over the surface, (d) defects will be detected in red color. [24]

1.5.3 Magnetic particle testing

Magnetic particle testing is used for the testing of materials which can be easily magnetized. This method is capable of detecting open to surface and just below the surface flaws. In this method the test specimen is first magnetized either by using a permanent or an electromagnet or by passing electric current through or around the specimen. The magnetic field thus introduced into the specimen is composed of magnetic lines of force. Whenever there is a flaw which interrupts the flow of magnetic lines of force, some of these lines must exit and re-enter the specimen. These points of exit and re-entry form opposite magnetic poles. Whenever minute magnetic particles are sprinkled

onto the surface of such a specimen, these particles are attracted by these magnetic poles to create a visual indication approximating the size and shape of the flaw [97]. Figure 1.31 illustrates the basic principles of this method.

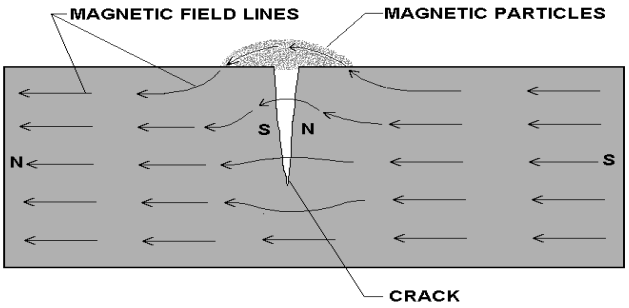

Figure 1.31: Basic principle of magnetic particle testing. [72]

1.5.4 Eddy current testing

One of the more widely practiced NDT techniques is eddy current testing. The flow of eddy currents is affected by fissures, constrictions or other discontinuities that cause distortions in the cross section through which the current is made to flow. Thus, the eddy current technique is useful for detecting the wall thickness of thin materials as well as measuring localized discontinuities. The thickness of the part must be within the depth of penetration (referred to as the skin depth) of the eddy currents and is dependent upon material properties and operating frequency. It is usually less than 0.635 cm (0.25 in.) and may be very much less, particularly for ferromagnetic materials [76].

Eddy currents are created through a process called electromagnetic induction. When alternating current is applied to the conductor, such as copper wire, a magnetic field develops in and around the conductor. This magnetic field expands as the alternating current rises to maximum and collapses as the current is reduced to zero. If another electrical conductor is brought into the close proximity to this changing magnetic field, current will be induced in this second conductor. Eddy currents are induced electrical currents that flow in a circular path. They get their name from “eddies” that are formed when a liquid or gas flows in a circular path around obstacles when conditions are right. Eddy current examination has been covered a broad range of products and inspection requirements. Conducting eddy current tests to check conductivity, heat treatment condition, sorting of materials, crack and coating thickness at leading and trailing edge of turbine blades, bolt holes and fastener inspections using hand held probes, tubing inspection of both ferromagnetic and non-ferromagnetic material for heat exchangers and boiler tubes. Figure 1.32 represents the basic principles of eddy current testing.

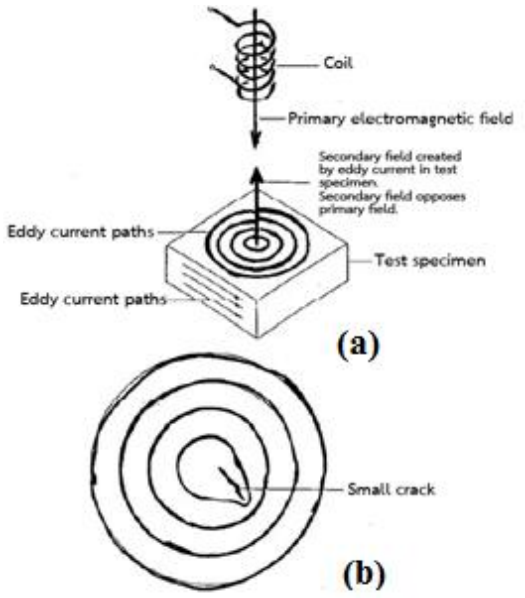

Figure 1.32: Eddy current testing, (a) generation of eddy currents in the test specimen, (b) distortion of eddy currents due to defect. [42]

There are three types of probes (figure 1.33) used in eddy current testing. Internal probes are usually used for the in-service testing of heat exchanger tubes. Encircling probes are commonly used for the testing of rods and tubes during manufacturing. The uses of surface probes include the location of cracks, sorting materials, measurement of wall and coating thickness, and case depth measurement.

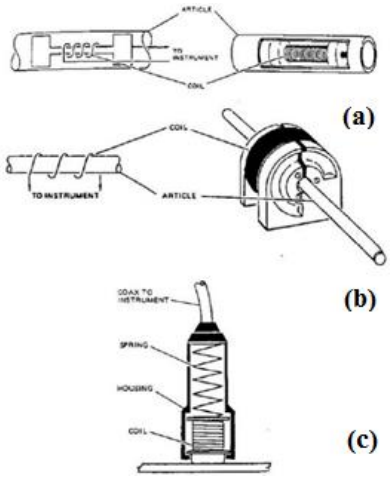

Figure 1.33: Types of probes used in eddy current testing. (a) internal coil, (b) encircling coil, (c) surface probe. [42]

1.5.5 Radiographic testing

Radiographic testing (RT) as a non-destructive testing (NDT) is based on the same principle as medical radiography in a hospital. A piece of radiographic film is placed on

the remote side of the material under inspection and radiation is then transmitted through from one side of the material to the remote side where the radiographic film is placed. The radiographic film detects the radiation and measures the various quantities of received over the entire surface of the film. This film is then processed under dark room conditions and the various degrees of radiation received by the film are imaged by the display of different degrees of black and white. This is termed the film density and is viewed on a special light emitting device. Discontinuities in the material affect the amount of radiation being received by the film through that particular plain of the material. Qualified inspectors can interpret the resultant images and record the location and type of defect present in the material. The conventional radiography can be used on most materials and product forms, e.g. welds, castings, composites etc. Radiographic testing provides a permanent record in the form of a radiograph and provides a high sensitivity of the internal structure of the material [90].

The forms of radiation either x-ray or gamma rays from a radioactive source are utilized to test a component exposing a photographic film placed on the opposite side of the radiation source. The placing of the radioactive source will depend on the geometry of the piece being examined. After processing, the film obtained is a permanent record of the weld showing the majority of internal imperfections. The use of ionizing rays (x-rays, gamma rays) to create a shadow object in the film. Radiography is generally used to look opaque object, such as in the welded pipe or any welded joints connections [47]. This process can be illustrated in figure 1.34.

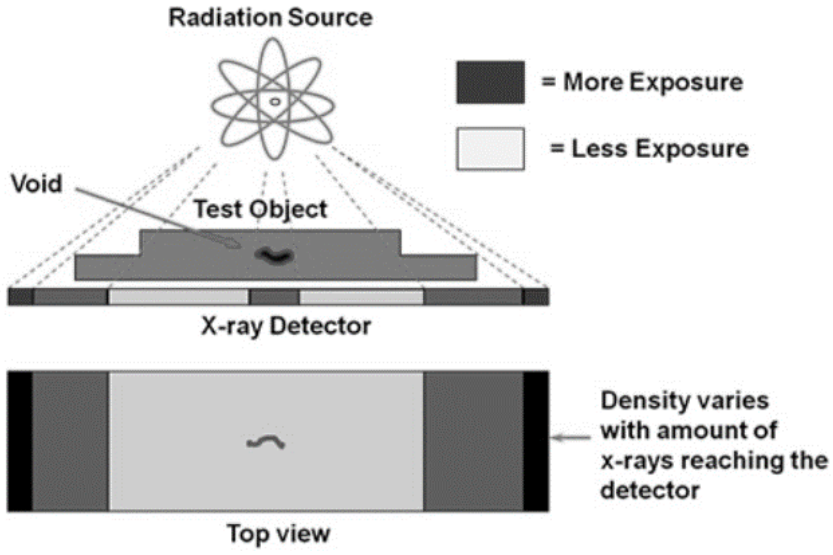

Figure 1.34.: Arrangement for radiographic testing method. [47]

1.5.6 Ultrasonic Testing

Ultrasonic testing as a non-destructive testing (NDT) employs high-frequency sound pulses that are emitted from a transducer and also it has a superior penetrating power than radiography and can detect flaws deep in the test specimen (say up to about 6 to 7 meter of steel). The sound wave is induced into the material through a probe which is usually in contact with the material. These sound waves propagate through the material, and are reflected back to the probe when they reach an interface. The reflected waves are transmitted back through the probe and connecting leads to a detector which can be either analogue or digital. The sound waves are then displayed as a series of signals on a monitor and the qualified inspector can measure and interpret these signals to allow accurate evaluation of the internal structure of the material. Ultrasonic testing can be used not only to indicate a surface or subsurface flaw but also to determine the depth, size and type of flaw. Another advantage of using ultrasonic testing is the accurate measurement of the thickness of the material. The method can be applied to most materials provided those materials can transmit sound waves. Ultrasonic testing is considered to be a fast and effective way of inspection, ensuring high-sensitivity results [71].

Ultrasonic testing (UT) is used in the testing of nearly all solid materials, such as fine-grained aluminum, steels and alloys, composites and plastics – practically any solid material where detection of internal discontinuities or thickness measurements are of most common concern. It is also used in the detection of interlaminar separations and regions that have been improperly processed or damaged in layered composite structures. This technique is less effective with highly inhomogeneous and coarse- grained materials (such as concrete and stainless steel castings) and non-elastic materials (such as rubber and soft plastics) that tend to absorb or scatter ultrasonic energy at relatively short distances. The basic principle of ultrasonic testing is illustrated in figure 1.35.

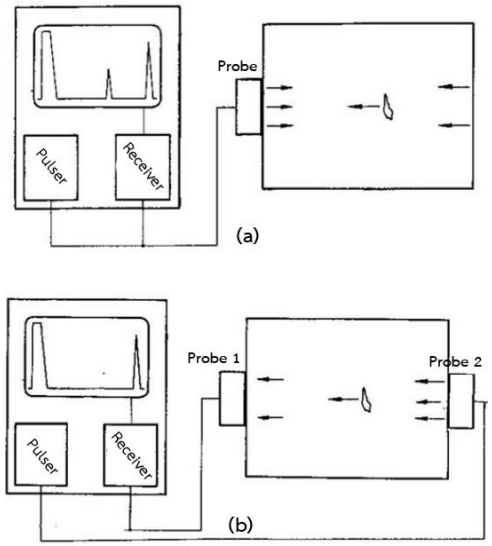

Figure 1.35: Basic components of an ultrasonic flaw detection system, (a) pulse echo method, (b) through transmission method. [42]

1.5.7 Acoustic emission testing

The main purpose of acoustic emission testing (AET) is the detection of growing defects of tanks, pressure vessels, reactors and piping systems during elevated pressurization. The detection of defects is performed by measuring and analyzing acoustic emission signals, typically within the frequency range of 20 kHz to 2 MHz, which are emitted when cracks grow or other rapid local dislocations within the stressed structure occur.

Many specific applications have been developed using acoustic emission because it is an extremely powerful technology that can be deployed within a wide range of usable applications of non-destructive testing, for instance, detecting discontinuities formed during welding, detecting undesired tool contact during automated machining, and detecting wear and loss of lubrication in rotating equipment. Other types of application are shown as follows:

- Non-destructive testing of heavily mechanically stressed components or complete structures of fiber-reinforced plastics or composites, as used in the aerospace industry.
- Investigation of material properties, breakdown mechanisms, and damage behavior.

- Inspection and quality assurance, for example, monitoring of welding and wood drying processes, series inspection of ceramic components, scratch tests and more.
- Real-time leakage test and location within various components, ranging from a small valve up to a tank bottom with diameter of 100m.
- Geological and micro-seismic research.
- Detection and location of high-voltage partial discharges in large transformers.

1.5.7.1 Principle of acoustic emission testing

AET is considered quite unique among the non-destructive testing method (NDT). Basically, the different NDT techniques can be distinguished passive and active techniques. Figure 1.36 illustrates the idea behind the terms “active” and “passive” in NDT. In active methods, the source emitting the waves is generally applied to the material as scanning techniques, for example, ultrasound method. On other hand, in passive methods, the emissive sources are produced within test material. Therefore, AET should be considered to be a passive non-destructive technique, because it detect emissive sources radiated by a growing fracture of test material.

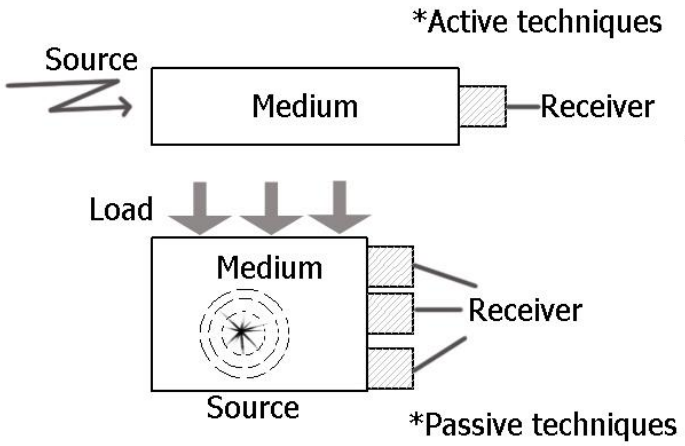

Figure 1.36: Comparison of NDT using active or passive techniques. [38]

1.5.7.2 Burst (transient) and continuous signals

Normally, there are two types of acoustic emission (AE) signals which are burst (transient) and continuous signals. For burst signals, their start and end point signals clearly differ from background noise as illustrated in figure 1.37a. For continuous signals, they show amplitude and frequency variations of signal, but the signal never ends as displayed in figure 1.37b.

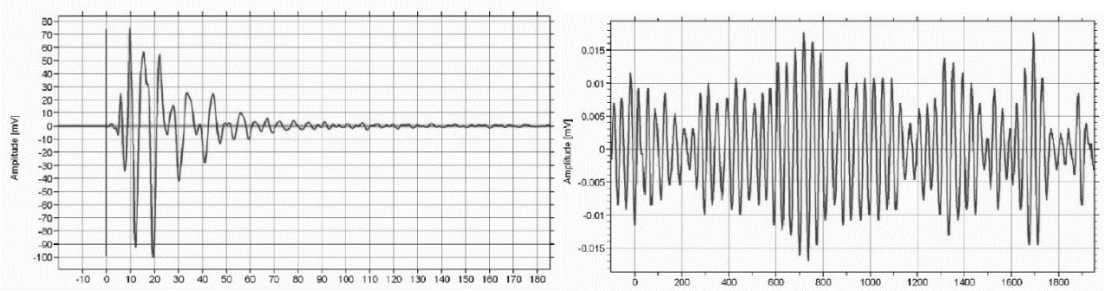

(a) *(b)*

Figure 1.37: The signal characteristics of burst (a), and continuous signals (b). [102]

The useful signals for AE testing with large pressure vessels are burst type signals, e.g. originating from fracture or crack growth. Continuous signals are mostly unwanted signals (noise) such as friction or flow noise. But even burst signals can be interfering signals, e.g. short friction noise or electrical spikes. At best the background noise is just the electronic noise of the preamplifier or the sensor [100].

1.5.7.3 Acoustic emission signal parameters

The electrical signal identified as an AE signal is generated by fracture phenomena. Therefore characteristics of AE parameters have been studied to infer fracture of physical phenomena. The definitions of AE parameters are importantly illustrated in figure 1.38 and described their meanings below.

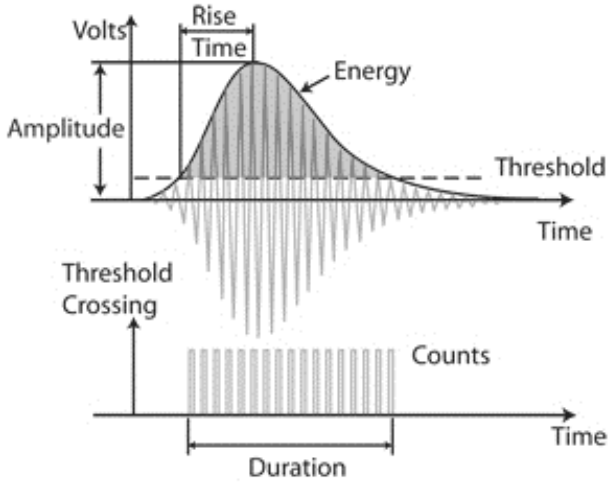

Figure 1.38: Conventional AE signal features. [68]

Threshold, a voltage level as an electronic comparator will only recognize and process the signals which have amplitudes larger than this voltage level. The voltage threshold may be adjustable, fixed, or automatic floating.

Duration, a time interval between the triggered time of one AE signal (waveform) and the time of disappearance is assigned. The duration is expressed generally on microseconds, which depends on source magnitude and noise filtering.

Count, the number of times within the duration, where the acoustic emission signal exceeds a present threshold.

Hit, the number obtained by counting each discerned acoustic emission event once.

Rise time, a time interval between the triggering time of AE signal and the time of the peak amplitude is assigned. The rise time is closely related to the source-time function, and applied to classify the type of fracture or eliminate noise signals.

AE amplitude, a peak voltage of the signal attained by the signal waveform an emission event.

Energy, a presented parameter equal to the energy under the curve, one of the best ways to measure AE activity.

AE signal, it is short rapid, release of energy in the form of a transient elastic wave.

RMS, root mean square of the continuous background noise before the burst will be detected.

1.5.7.4 Acoustic emission system components

The AET is associated with the detection and conversion of high frequency elastic waves to electrical signals. This is accomplished by directly coupling piezoelectric transducer (AE sensor), which can be either resonant and bandwidth types, on the surface of the structure under test and loading as shown in figure 1.39. Sensor is coupled to the structure and the output of piezoelectric sensor is amplified through a low-noise preamplifier. Then, the signals pass through a filter to remove any extraneous noise [68]. After that, the signals are amplified by the main amplifier again before being sent to the signal conditioner. Finally, the AE signals are subtracted and stored in a computer for further analysis. During investigations, other parameters, such as, load, deformation, pressure, and temperature, can also be recorded as other parametric inputs.

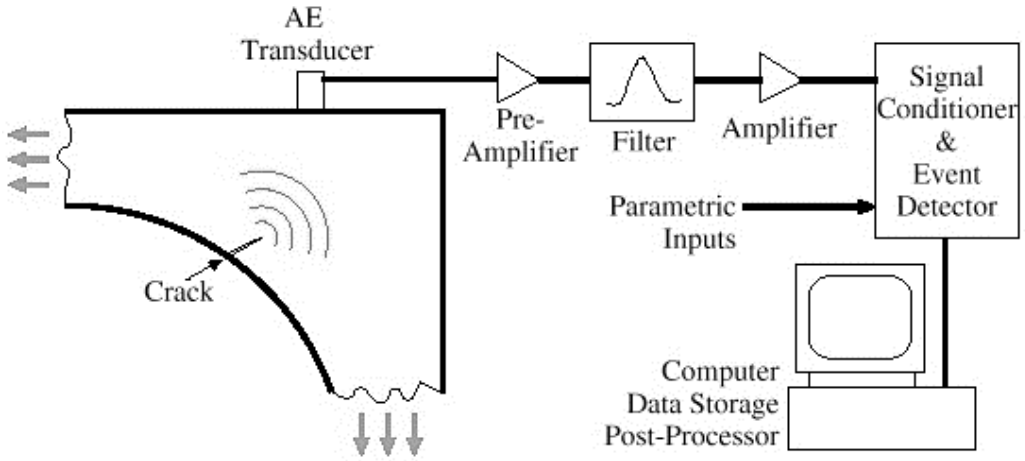

Figure 1.39: A typical AE system setup. [92]

1.5.7.5 AE Transducer types

Basic transduction mechanisms can be used to achieve a transducer's functions: the detection of surface motion and the subsequent generation of an electrical signal. Capacitive transducers have been successfully used as acoustic emission transducers for special laboratory tests. Such transducers can have good fidelity, so that the electrical signal very closely follows the actual dynamic surface displacement. However, the typical minimum displacement measured by a capacitive transducer is on the order of 10^{-10}m. Such sensitivity is not enough for actual acoustic emission testing.

1.5.7.6 Piezoelectric transducers

Acoustic emission testing is nearly always performed with transducers that use piezoelectric elements for transduction. The element is usually a special ceramic such as lead zirconate titanate and is acoustically coupled to the surface of the test item so that the dynamic surface motion propagates into the piezoelectric element. The dynamic strain in the element produces a voltage-versus-time signal as the transducer output. Because virtually all acoustic emission testing is performed with a piezoelectric transducer.

1.5.7.7 Frequency range

The majority of acoustic emission testing is based on the processing of signals with frequency content in the range from 30 kHz to about 1 MHz. In special applications, detection of acoustic emission at frequencies below 20 kHz or near audio frequencies can improve testing and conventional microphones or accelerometers are sometimes used. Attenuation of the wave motion increases rapidly with frequency and, for materials with higher attenuation (such as fiber reinforced plastic composites), it is necessary to sense

lower frequencies to detect acoustic emission hits. At higher frequencies, the background noise is lower; for materials with low attenuation, acoustic emission hits tend to be easier to detect at higher frequencies.

Acoustic emission transducers can be designed to sense a portion of the whole frequency range of interest by choosing the appropriate dimensions of the piezoelectric element. This, along with its high sensitivity, accounts for the popularity of this transduction mechanism. In fact, by proper design of the piezoelectric transducer, motion in the frequency range from 30 kHz to 1 MHz can be transduced by a single transducer. This special type of transducer has applications (1) in laboratory experiments, (2) in acoustic emission transducer calibration and (3) in any tests where the actual displacement is to be measured with precision and accuracy [101].

1.5.7.8 AE transducer design

Figure 1.40 is a schematic diagram of a typical AE transducer mounted on a test object. The transducer is attached to the surface of the test object and a thin intervening layer of couplant is usually used. The couplant facilitates the transmission of acoustic waves from the test object to the transducer. The transducer may also be attached with an adhesive bond designed to act as an acoustic couplant.

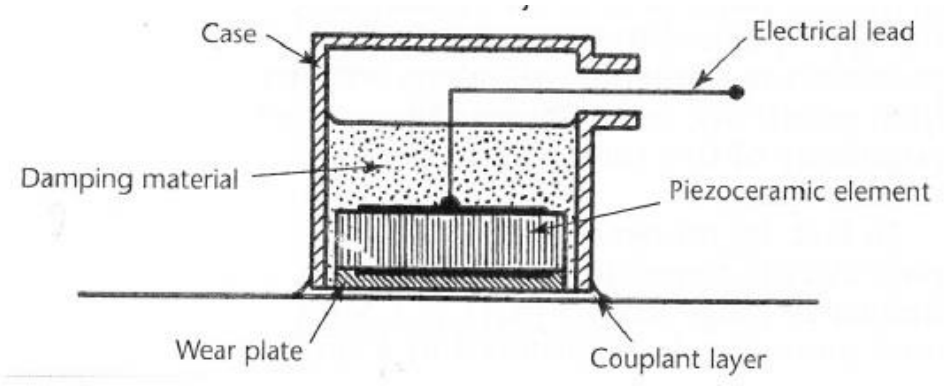

Figure 1.40: Schematic diagram of a typical acoustic emission transducer mounted on a test object. [83]

An acoustic emission transducer normally consists of several parts. The active element is a piezoelectric ceramic with electrodes on each face. One electrode is connected to electrical ground and the other is connected to a signal lead. A wear plate protects the active element. Behind the active element is usually a backing material, often made by curing epoxy containing high density tungsten particles. The backing is usually designed so that acoustic waves easily propagate into it with little reflection back to the

active element. In the backing, much of the wave's energy is attenuated by scattering and absorption. The backing also serves to load the active element so that it is less resonant or broader band. Less resonance helps the transducer respond more evenly over a somewhat wider range of frequencies.

The typical acoustic emission transducer also has a case with a connector for signal cable attachment. The case provides an integrated mechanical package for the transducer components and may also serve as a shield to minimize electromagnetic interference. There are many variations of this typical transducer design, including (1) designs for high temperature applications, (2) transducers with built-in preamplifiers or line drive transformers, (3) transducers with more than one active element and (4) transducers with active elements whose geometry or polarization is specifically shaped [83].

1.5.7.9 Acoustic emission testing in metal corrosion processes

Acoustic emission is based on measuring acoustic sound waves that are emitted during the growth of microscopic defects, such as stress corrosion cracks, pitting corrosion, and crevice corrosion. It is the flaw growth or even plastic deformation that generates the sound waves that are detected by the acoustic sensors. Secondary emissions from crack breaking of corrosion pocket can also be employed for the detection of flaws [80].

Discriminating initiation and propagation steps of pitting corrosion by using acoustic emission testing was discussed by Fregonese M. et al. (2001). A particular polarization method was performed to establish the pitting corrosion in each step on AISI 316L stainless steel separately. The outcomes of this experiment showed that the initiation step of pitting corrosion did not generate a lot of AE signals, whereas the propagation step was characterized by the numerous emission of AE signal. The friction phenomenon of the evolving hydrogen bubbles inside the pits was also proposed to be the emissive source during corrosion process. Furthermore, the opening of the pits on specimen surface could be induced to be uniform corrosion owning to more sever electrochemical conditions.

Kim Y.P. et al. (2003) studied on monitoring of crevice corrosion process on 304L austenitic stainless steel using acoustic emission technique. Crevice assembly, which was tool for put test specimen into electrochemical corrosive solution, was particularly designed for working acoustic emission sensor in order to effectively detect AE signals

on test specimen during initiation, propagation, and re-passivation of crevice corrosion process. From this study, they discovered that AE parameters, which were rise time, counts number, duration, and cumulative energy of AE signals were directly affected by crevice development, especially in propagation phase, and all AE parameters recorded in this study was highly similar with AE parameters generated by pitting corrosion on austenitic stainless steel as well.

Determining the location and types of corrosion process by acoustic emission was proposed by Jomdecha C. et al. (2007). In this study, AISI304 austenitic stainless steel was chosen as test materials. Corrosive solution and the electrochemical method were prepared for control corrosion processes. AE source-location system was employed to detect AE signals established from deterioration sources. Their interesting results revealed uniform, pitting, crevice, and stress corrosion cracking could be distinguished by the correlations of their AE parameters, for instance, counts versus amplitude, hits versus amplitude, and cumulative counts versus time. Furthermore, it was noticed that pitting and crevice corrosion had acoustic emission characteristics similarly.

Studying in correlation between corrosion rate and AE signal in an acidic environment for mild steel was justified by Kasai N. et al. (2009). In this experiment, several electrochemistry measurements and AE measurements were simultaneously carried out to clarify the mechanism of AE signals under a strong acid environment. Based on these experimental results, it was found that a lot of AE signals were generated under a low-pH environment more than being in a high-pH environment due to the rupture of hydrogen gas on the surface of the test pieces and polarization conductance and calculated weight loss values did not only explain the corrosion rate of a test specimen during experiment, but they also had the correlation with the AE signals relatively.

Studying acoustic emission signals generated from pitting and uniform corrosion was reported by Jirarungsatian C. et al. (2010) Electrochemical polarization methods were employed for corrosion control on test specimen which was stainless steel sheet and AE device was also used for investigation AE signals of test specimen. The relevant result was presented that duration and frequency of AE signals as AE parameters were chosen to correlate with corrosion phenomena because they exhibited high correlation with pitting and uniform processes. Moreover, the authors found that pitting corrosion process could be separated into three states using selected AE parameters and two categorization for uniform corrosion.

Jian X. et al. (2010) tried to correlate AE activity with corrosion rate of 304 stainless steel in H_2SO_4 solutions by using electrochemical corrosion method, which could estimate in terms of hydrogen evolution rate, weight loss, surface damage, or applied current density. The interesting results were reported that three electrochemical processes generating the main AE sources during corrosion process clearly were oxygen bubbles, hydrogen bubbles evolution, and transpassive dissolution. The AE signals associated with each process were described by their AE activity. To monitor corrosion processes in this experiment easily, a concept of potential (E) – pH – AE diagram was proposed by them to assess the corrosion condition of the test material. Additionally, due to transpassive dissolution, the breakdown of passive films was believed to be the AE source mechanism generated by larger pores and some small pores simultaneously.

Xu J. et al. (2011) reported on their interesting article about acoustic emission during pitting corrosion of 304 stainless steel being under H_2SO_4 solutions with various pH values and Cl^-. In this study, potentiostat device, AE measurement, and a long-distance microscope were employed to simulate electrochemical reaction on test specimen and observe the surface of specimen throughout this study. As results of this study, they were mentioned that detecting AE signals during pitting corrosion could be discriminated between low rise time, counts number, duration and higher ones. It appeared that duration and amplitude were better to range different pitting corrosion steps. Moreover, they proposed that hydrogen bubbles evolution was the AE sources during pitting corrosion.

Woonggi H. et al. (2015) used AE testing to monitor the stress corrosion cracks in a type 304 stainless steel tube. To make corrosion process on test specimen, test specimen was filled with specific corrosive liquid and heated on its outer surface with high pressure of 73 bar to simulate a corrosive environment over experimental time. Based on the study results, AE method could be utilized to detect initial and propagating cracks causing from stress corrosion in test tube. The variation of cumulative acoustic emission counts revealed that corrosion stages of test specimen could be separated into four stages as following; chemical stabilization stage, stress corrosion crack initiation and propagation stage, passive film rupture stage, and crack propagations stage, respectively.

1.6 Fatigue failure in metals

Fatigue failure is defined as the tendency of a material to fracture by means of progressive brittle cracking under repeated alternating or cyclic stresses of an intensity considerably below the normal strength. Although the fracture is of a brittle type, it may take some time to propagate, depending on both the intensity and frequency of the stress cycles [28].

Fatigue failure occurs in many different forms. Fluctuations in externally applied stresses or strains result in mechanical fatigue. Cyclic loads acting in association with high temperatures cause creep-fatigue; when the temperature of the cyclically loaded component also fluctuates, thermomechanical fatigue is induced. Recurring loads imposed in the presence of a chemically aggressive or embrittling environment give rise to corrosion fatigue. The repeated application of loads in conjunction with sliding and rolling contact between materials produces sliding contact fatigue and rolling contact fatigue, respectively, while fretting fatigue occurs as a result of pulsating stresses along with oscillatory relative motion and frictional sliding between surfaces. The majority of failures in machinery and structural components can be attributed to one of the above fatigue processes. Such failures generally take place under the influence of cyclic loads whose peak values are considerably smaller than the 'safe' loads estimated on the basis of static fracture analyses [89].

1.6.1 Major factors affecting the fatigue strength of a metal

The fatigue strength of a metal or alloy is affected by factors other the chemical composition of the metal itself. Some of the most important of these are [27]:

Stress concentration, fatigue strength is greatly reduced by the presence of stress raisers such as notches, holes, keyways, or sharp changes in cross sections. For example, the fatigue failure shown in figure 1.41 started at the end of keyway in steel shaft at the points B and progressed to final rupture at C. Fatigue failures can be minimized by careful design to avoid stress raisers whenever possible.

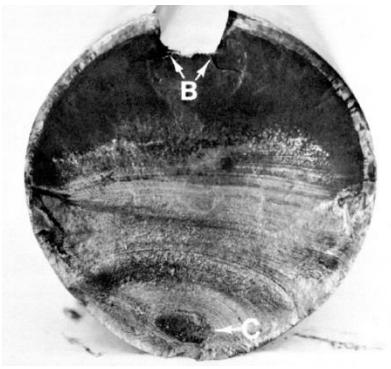

Figure 1.41: Fatigue fracture of a drive shaft. [8]

Surface roughness factor, in general, the smoother the surface finish on the metal sample, the higher the fatigue strength. Rough surfaces create stress raisers that facilitate fatigue crack formation.

Surface condition factor, since most fatigue failures originate at the metal surface, any major change in the surface condition will affect the fatigue strength of the metal. For example, surface-hardening treatments for steels, such as carburizing and nitriding, which harden the surface, increase fatigue life. Decarburizing, on the other hand, which softens a heat-treated steel surface, lowers fatigue life. The introduction of a favorable compressive residual stress pattern on the metal surface also increases fatigue life.

Environment factor, when a corrosive environment is present during the cyclic stress of a metal, the chemical attack greatly accelerates the rate at which fatigue cracks propagate. The combination of corrosion attack and cyclic stresses on a metal is known as corrosion fatigue.

1.6.2 Basic structural changes occurring in ductile metal in the fatigue process

When a specimen of a ductile homogeneous metal is subjected to cyclic stresses, the following basic structural changes occur during the fatigue process [86]

Slip-band crack growth state, Crack initiation occurs because plastic deformation is not a completely reversible process. Plastic deformation in one direction and then in the reverse direction causes surface ridges and grooves called slipband extrusions and slipband intrusions to be created on the surface of the metal specimen as well as damage within the metal along persistent slipbands as displayed in figure 1.42. The surface irregularities and damage along the persistent slipbands cause cracks to form at or near the surface that propagate into the specimen along the planes subjected to high shear stresses. The rate of the crack growth is in general very low.

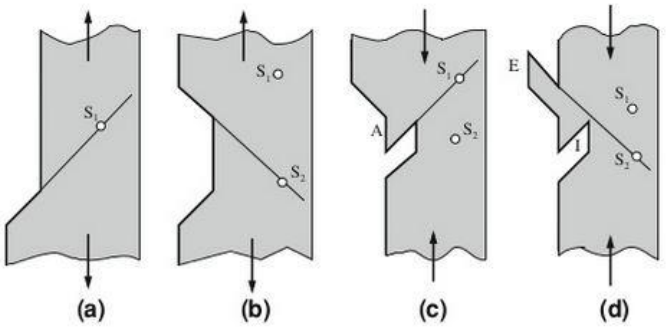

Figure 1.42: Mechanism for the formation of slipband extrusions and introusion. [46]

Crack growth on planes of high tensile stress, during stage of slipband crack growth, the crack may grow in a polycrystalline metal only a few grain diameters before it changes its direction to be perpendicular to the direction of the maximum tensile stress on the metal specimen. In this stage, a well-defined crack propagates at a relatively rapid rate (i.e., micrometers per cycle), and fatigue striations are created as the crack advances across the cross section of the metal specimen. These striations are useful in fatigue failure analysis for determining the origin and direction of propagation of fatigue cracks.

Ultimate ductile failure state, finally, when the crack covers a sufficient area so that the remaining metal at the cross section cannot support the applied load, the sample ruptures by ductile failure.

1.6.3 The S-N curve

Before a microstructural understanding of fatigue processes was developed, engineers had developed empirical means of quantifying the fatigue process and designing against it. Perhaps the most important concept is the S-N diagram as illustrated in figure 1.43 in which a constant cyclic stress amplitude S is applied to a specimen and the number of loading cycles N until the specimen fails is determined [69]. An example in figure 1.43, a fatigue stress below 49 kpsi will not induce failure.

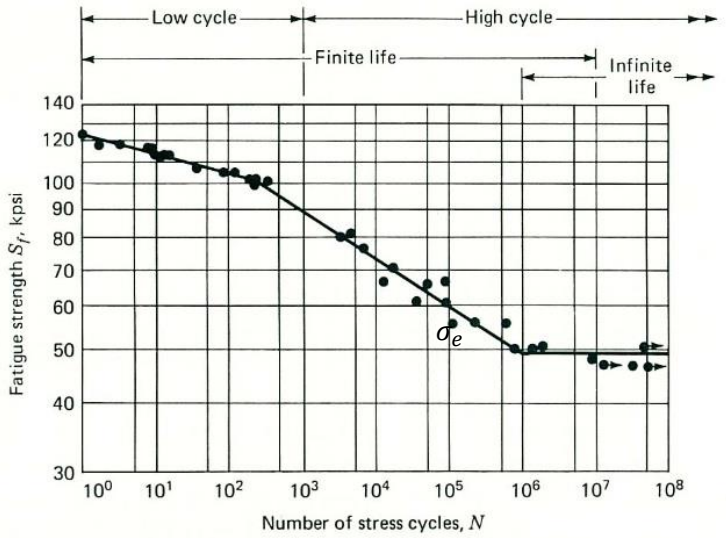

Figure 1.43: S-N diagram plotted from the results of reversed axial fatigue tests. [70]

In some materials, notably ferrous alloys, the S-N curve flattens out eventually, so that below a certain endurance limit (σ_e) failure does not occur no matter how long the loads are cycled. Obviously, the designer will size the structure to keep the stresses below σ_e by a suitable safety factor if cyclic loads are to be withstood. For some other materials such as aluminum, no endurance limit exists and the designer must arrange for the planned lifetime of the structure to be less than the failure point on the S-N curve [69].

One significant limitation of the S-N curve is that the resulting plot is highly dependent on the test conditions such as, sample geometry, sample surface condition, and material. Using an S-N curve to predict real-world life when conditions do not match the test conditions under which the curve was developed is dubious. This severely limits the use of S-N curves in product design. On the other hand, the ease of construction makes the S-N curve a simple and valuable tool in making relative comparisons between materials or process variations [70].

1.6.4 Fatigue crack initiation

Fatigue is one of the primary reasons for the failure of structural components. The life of a fatigue crack has two parts; initiation and propagation. Dislocations play a major role in the fatigue crack initiation phase. It has been observed in laboratory testing that after a large number of loading cycles dislocations pile up and form structures called persistent slip bands (PSB). An example of a PSB is displayed in figure 1.44a.

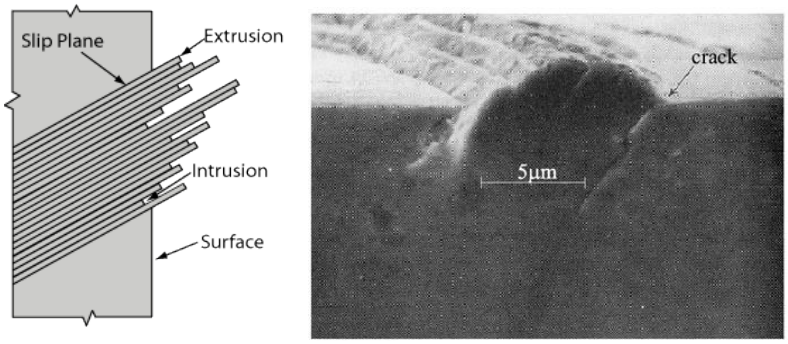

(a) *(b)*

Figure 1.44: Fatigue crack initiation, (a) Typical PSB feature, (b) PBS photo by SEM. [70]

PSBs are areas that rise above (extrusion) or fall below (intrusion) the surface of the component due to movement of material along slip planes. This leaves tiny steps in the surface that serve as stress risers where fatigue cracks can initiate. A crack at the edge of a PSB is shown in figure 1.44b taken with a scanning electron microscope (SEM) [70].

1.6.5 Characterization of crack growth

The rate of growth of a fatigue crack subjected to constant amplitude stress reversals is expressed in terms of the crack length increment per cycle, The crack growth (da/dN) is obtained by taking the derivative of crack length (a) versus cycle (N) [95]. Value of da/dN for different loading conditions are determined from experimentally determined changes in crack length over a number of elapsed fatigue cycles. When the applied stress range is held constant, the rate of growth of a fatigue crack generally increases with increasing number of fatigue cycles. Figure 1.45 schematically shows a typical fatigue crack growth curve.

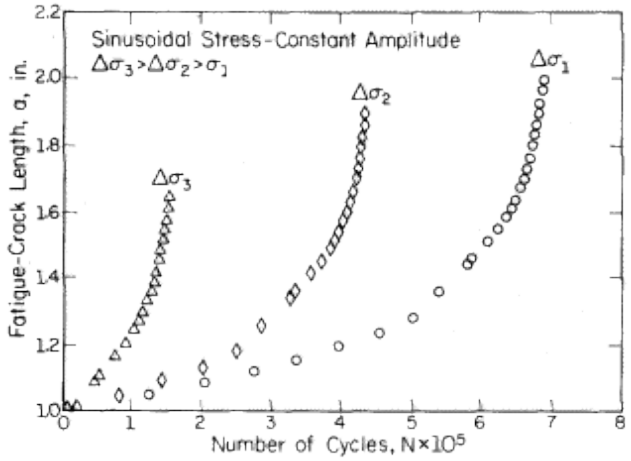

Figure 1.45: Typical crack growth behavior in constant amplitude fatigue loading. [95]

The crack growth rate for materials under cyclic stress that behave as indicated in figure 1.45 indicates the following relationship [86].

$$\frac{da}{dN} \propto f(\sigma, a) \qquad \text{(Eq.10)}$$

For many engineering alloys, the fatigue crack growth rate expressed as the differential da/dN can be related to the stress-intensity range ΔK for a constant-amplitude fatigue stress by the equation.

$$\frac{da}{dN} = A\Delta K^m \qquad \text{(Eq.11)}$$

Where da/dN = fatigue crack growth rate, mm/cycle or in./cycle

ΔK = stress-intensity factor range ($\Delta K = K_{max} - K_{min}$), $MPa\sqrt{m}$ or $ksi\sqrt{in.}$

A, m = constants that are a function of the material, environment, frequency, temperature, and stress ration

Note in Eq. 11 that we use the stress-intensity factor K_I (mode I) and not the fracture toughness value K_{IC}. Thus, at the maximum cyclic stress, the stress-intensity factor $K_{max} = \sigma_{max}\sqrt{\pi a}$, and at the minimum cyclic stress, $K_{min} = \sigma_{min}\sqrt{\pi a}$. For the range of stress-intensity factor, $\Delta K(range) = K_{max} - K_{min} = \Delta K = \sigma_{max}\sqrt{\pi a} - \sigma_{min}\sqrt{\pi a} = \sigma_{range}\sqrt{\pi a}$. Since the stress-intensity factor is not defined for compressive stresses, if σ_{min} is in compression, K_{min} is assigned zero value. If there is a Y geometric correction factor for the $\Delta K = \sigma_r\sqrt{\pi a}$ equation, the $\Delta K = Y\sigma_r\sqrt{\pi a}$.

1.6.6 Fatigue life calculation

Sometimes in designing a new engineering component using a particular material, it is desirable to obtain information about the fatigue life of the part. One type of equation for calculating fatigue life can be developed by integrating Eq.11 between an initial crack size (a_0).

And the critical crack size (a_f), which is produced at fatigue failure after the number of cycles to failure (N_f).

Considering Eq.11 with following ΔK.

$$\Delta K = Y\sigma\sqrt{\pi a} = Y\sigma\pi^{1/2}a^{1/2} \qquad \text{(Eq.12)}$$

$$\Delta K^m = Y^m\sigma^m\pi^{m/2}a^{m/2} \qquad \text{(Eq.13)}$$

$$\frac{da}{dN} = A(Y\sigma\sqrt{\pi a})^m = A(Y^m\sigma^m\pi^{m/2}a^{m/2}) \qquad \text{(Eq.14)}$$

After rearranging Eq.14, integrating the crack size from the initial crack size (a_0) to the final crack size at failure (a_f) is conducted and the number of fatigue cycles from zero to the number at fatigue failure (N_f) is [86];

$$\int_{a_0}^{a_f} da = AY^m \sigma^m \pi^{m/2}.a^{m/2} \int_0^{N_f} dN \qquad \text{(Eq.15)}$$

$$\int_0^{N_f} dN = \int_{a_0}^{a_f} \frac{da}{A\sigma^m \pi^{m/2} Y^m a^{m/2}} = \frac{1}{A\sigma^m \pi^{m/2} Y^m} \int_{a_0}^{a_f} \frac{da}{a^{m/2}} \qquad \text{(Eq.16)}$$

Using the relationship of

$$\int a^n da = \frac{a^{n+1}}{n+1} + c \qquad \text{(Eq.17)}$$

Integrating Eq.16 and then letting $n = -m/2$

$$\frac{1}{A\sigma^m \pi^{m/2} Y^m} \int_{a_0}^{a_f} \frac{da}{a^{m/2}} = \frac{1}{A\sigma^m \pi^{m/2} Y^m} \left(\frac{a^{-(m/2)+1}}{-m/2+1} \right) \Big|_{a_0}^{a_f} \qquad \text{(Eq.18)}$$

Thus

$$N_f = \frac{a_f^{-(m/2)+1} - a_0^{-(m/2)+1}}{A\sigma^m \pi^{m/2} Y^m [-(m/2)+1]} \qquad m \neq 2 \qquad \text{(Eq.19)}$$

1.6.7 Different regimes of fatigue crack growth

Usually fatigue crack length versus stress-intensity factor range data are plotted as log da/dN versus log stress-intensity factor range (ΔK). These data are plotted as a log-log plot since in most cases a straight line or close to a straight-line plot is obtained. The basic reason for the straight-line plot is that the da/dN versus ΔK data closely obey the $da/dN = A\Delta K^m$ relationship, and so if the log is taken of both sides of this equation, it will be:

$$log \frac{da}{dN} = \log(A\Delta K^m) \qquad \text{(Eq.20)}$$

$$log \frac{da}{dN} = m\ log\ \Delta K + logA \qquad \text{(Eq.21)}$$

Which is an equation of a straight line of the form $y = mx + b$. Thus, plot of log (da/dN) versus log ΔK produces a straight line with a slope of m [86].

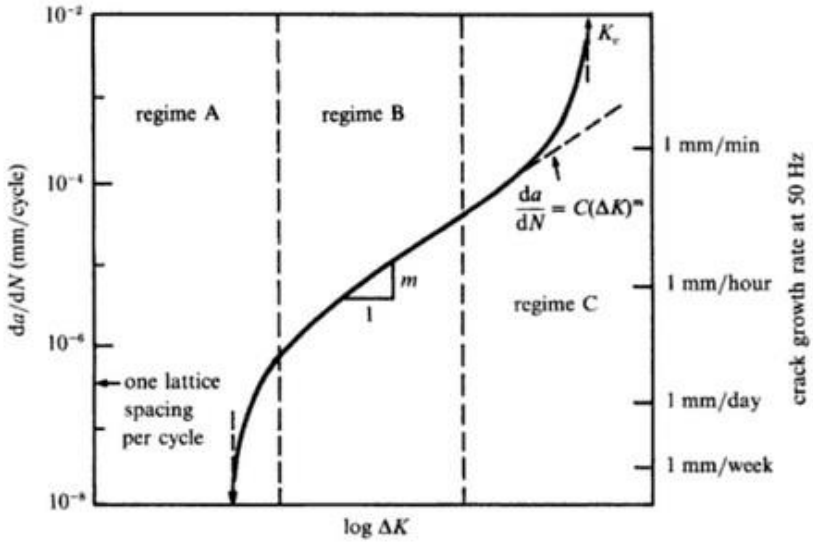

Figure 1.46: Schematic illustration of the different regimes of stable fatigue crack propagation. [89]

For most engineering alloys, a plot of log da/dN against log ΔK exhibits a sigmoidal variation, as shown schematically in figure 1.46. In this plot, there distinct regimes of crack growth can be identified [89]: regime A is the fatigue threshold region where the ΔK is too low to propagate a crack. Regime B encompasses data where the rate of crack growth changes roughly linearly with a change in stress intensity fluctuation. In regime C, small increases in the stress intensity amplitude, produce relatively large increases in crack growth rate since the material is nearing the point of unstable fracture causing catastrophic failure [75].

1.6.8 Monitor of acoustic emission signals in fatigue failure

Liskutin P. et al. (2008) studied in the fatigue life stages of AlMg Alloys by using application of non-destructive testing methods which were acoustic emission method and x-ray diffraction analysis. The electro magnetic resonance fatigue machine was used to make loading frequency on test specimens. The results of this study was reported that AE method proved a possibility of basic identification of individual stages of fatigue processes in AlMg alloy specimens but it was difficult to exactly specify the reason of changing AE signals. However, using AE method with x-ray diffraction analysis in this study would be better to expect the exact identification of AE source in each stages of fatigue failure processes.

Measurement of fatigue properties of Al Alloys, EN AW-6082/T6 and EN AW-7075/T6, was conducted by Mazal P. et al. (2010). In this study, the RUMUL cracktronic

(Russenberger Prüfmaschinen AG) which was bending fatigue machine was used to find the fatigue properties of test specimens, and acoustic emission test was simultaneously utilized to record the occurrence of AE signal from test specimens during bending fatigue test. The outcomes of this study indicated that the microstructural dissimilarities of test specimens had no a fundamental effect on fatigue properties in general observation, and using the acoustic emission method for examining the rise of micro-cracks and short crack in test specimens due to cyclic loading was a great potential method.

The investigation of bending fatigue behavior of Ti-6Al-4V alloy in high-cycle fatigue by using fatigue device which was RUMUL cracktronic was performed by Vlasic F. et al. (2013). They reported the influence of structural orientation of investigating materials was less distinctive, and the structural orientation actor did not play the main role of fatigue failure. For detected AE signals during fatigue tests, it was considered that the AE signals produced from source damage mechanisms of test material due to fatigue could be differentiated into three stages. These regions corresponded to slip plane formation stage, crack nucleation stage, and crack propagation stage.

Mazal P. et al. (2015) performed the experiment in the fatigue failure of 15CH2NMFA steel and Inconel 713LC by using AE method with RUMUL cracktronic. In this experiment, their experimental results clarified that fatigue process was able to be described by AE data, particularly in the plot of count rate and cumulative AE hit versus time. The AE behavior was characterized by three features corresponding to different stages of the fatigue failure. Large numbers of counts were emitted in the first period of fatigue life due to the movement and interaction of dislocations and persistent slip band formation. At the second period, the crack nucleation stage was characterized by low activity of AE signal with occasional peaks. And at near-fracture period, strong increase of AE activity was observed due to the macro-crack growth.

CHAPTER 2: OBJECTIVE OF THE DISSERTATION

The objective of the dissertation aims to present the application of acoustic emission method that is used for evaluating the degradation of metal materials subjected to welding process, corrosion process, and mechanical testing processes. In the experiments, aluminum alloy, magnesium alloy, and galvanized steel are chosen to be the test materials. The testing procedures presented in this dissertation will be mainly divided into two parts as following;

1. Utilizing acoustic emission method for monitor of cold metal transfer welding process, inspection of corrosion process of CMT-welded specimens, and examination of mechanical deformation of CMT-welded specimens.

2. Evaluation of degradation process of magnesium alloys loaded under high cycle fatigues by means of acoustic emission method.

The experiment results will be discussed and reported to provide the useful knowledge of using acoustic emission method in manufacturing process and maintenance process as well as inspection process in order to prevent the unsuitable conditions regarding the degradation process that can encounter in the metal materials.

CHAPTER 3: MATERIALS AND METHODS

3.1 Studied materials

Studying the degradation of metal materials used in agricultural technology was mainly concentrated in this dissertation. In order to clearly understand the degradation processes of materials, one of non-destructive testing (NDT), acoustic emission technique (AET), was implemented to find the possibility how acoustic emission system could be useful method to evaluate the quality of material during the deformation of materials. Therefore, the general information of studied materials were described as following.

3.1.1 Magnesium alloy

AZ31B Magnesium alloy was chosen to be the first material for being tested in the experiments because magnesium alloy has the great mechanical properties such as, light weight, high strength, and good castability. In general, magnesium alloy is produced in wide variety of shapes from sheet to bar forms. AZ31B is a wrought magnesium alloy with good room-temperature strength and ductility combined with corrosion resistance and weldability. Its quality finds application in wide variety of uses including aircraft fuselages, cell phone, and laptop cases. The typical chemical compositions and mechanical properties of AZ31B are listed in table 8, and 9, respectively.

Table 8: Chemical compositions of AZ31B. [9]

Element	Content (%)
Magnesium, Mg	97
Aluminum, Al	2.5 - 3.5
Zinc, Zn	0.6 - 1.4
Manganese, Mn	0.2
Silicon, Si	0.1
Copper, Cu	0.05
Calcium, Ca	0.04
Iron, Fe	0.005
Nickel, Ni	0.005

Table 9: Mechanical properties of AZ31B. [9]

Property	Metric
Tensile strength	260 MPa
Yield strength (strain 0.2%)	200 MPa
Shear modulus	17 GPa
Elastic modulus	44.8 GPa
Poisson's ratio	0.35
Elongation at break	15 %

3.1.2 Aluminum alloy

EN AW 6065 or Al6065 aluminum alloy was selected to be the second material that was studied the degradation process of its. Technically, Al6065 is an age hardenable alloy, the mechanical properties of which being mainly controlled by the hardening precipitates contained in the material. When the material is subjected to a solution heat treatment followed by quenching and a tempering treatment, its mechanical properties reach their highest level and become very good compared to other aluminum alloys. The interesting characteristic of the Al6065 is its good weldability, excellent joining characteristic, and high resistance to corrosion. The description of chemical compositions and mechanical properties of Al6065 are specified in table 10, and 11.

Table 10: Chemical compositions of Al6065. [63]

Element	Content (%)
Aluminum, Al	94.4 – 98.15
Bismuth, Bi	0.5 – 1.5
Chromium, Cr	0.15
Copper, Cu	0.15 – 0.4
Iron, Fe	0.7
Lead, Pb	0.05
Magnesium, Mg	0.8 – 1.2
Manganese, Mn	0.15
Silicon, Si	0.4 – 0.8

Table 11: Mechanical properties of Al6065. [63]

Property	Metric
Tensile strength	310 MPa
Yield strength (strain 0.2%)	276 MPa
Shear modulus	26 GPa
Elastic modulus	68.9 GPa
Poisson's ratio	0.33
Elongation at break	17 %

3.1.3 Galvanized steel

DX51D galvanized steel was third material used for being tested in the experiments of this dissertation. Normally, DX51D is the hot-dip galvanized steel according to EN 10346. In production process of galvanized steel, the steel is dipped into a bath of molten zinc that has been heated to around 460°C. The steel is then removed from the bath and left to cool in a quench tank. When the cooling process is complete, the zinc coting is then chemically bonded to the steel. The thickness of the zinc coating varies depending on consumers' requirements. Generally, its applications are widely used for the production of steel structures, roofs, and household appliances. The chemical compositions and mechanical properties of DX51D are described in table 12, and 13.

Table 12: Chemical compositions of DX51D. [63]

Element	Content (%)
Iron, Fe	Balance
Manganese, Mn	1.5
Silicon, Si	0.5
Titanium, Ti	0.3
Carbon, C	0.2
Phosphorus, P	0.12
Magnesium, Mg	0.8 – 1.2
Sulfur, S	0.045

Table 13: Mechanical properties of DX51D. [63]

Property	Metric
Tensile strength	380 MPa
Yield strength (strain 0.2%)	275 MPa
Elastic modulus	200 GPa
Elongation at break	16 %

3.2 Acoustic emission monitor of cold metal transfer welding

3.2.1 Description of the implemented CMT welding

To prepare the test specimens for doing experiments properly, the cold metal transfer (CMT) welding process was employed to join the dissimilar metal sheets together. Figure 3.1 shows the *CMT Advanced 4000* welding machine was composed of weldment-controlling unit, robotic-welding arm, and specimen-welding table. This type of welding machine is known as the best welding technique for connecting the thin sheet metal in present. In process of creating the test specimens, all test specimens were accomplished by *FRONIUS* company in Prague, Czech Republic. The technical specification of CMT welding machine used for welding the test specimens in experiment is listed in table 14.

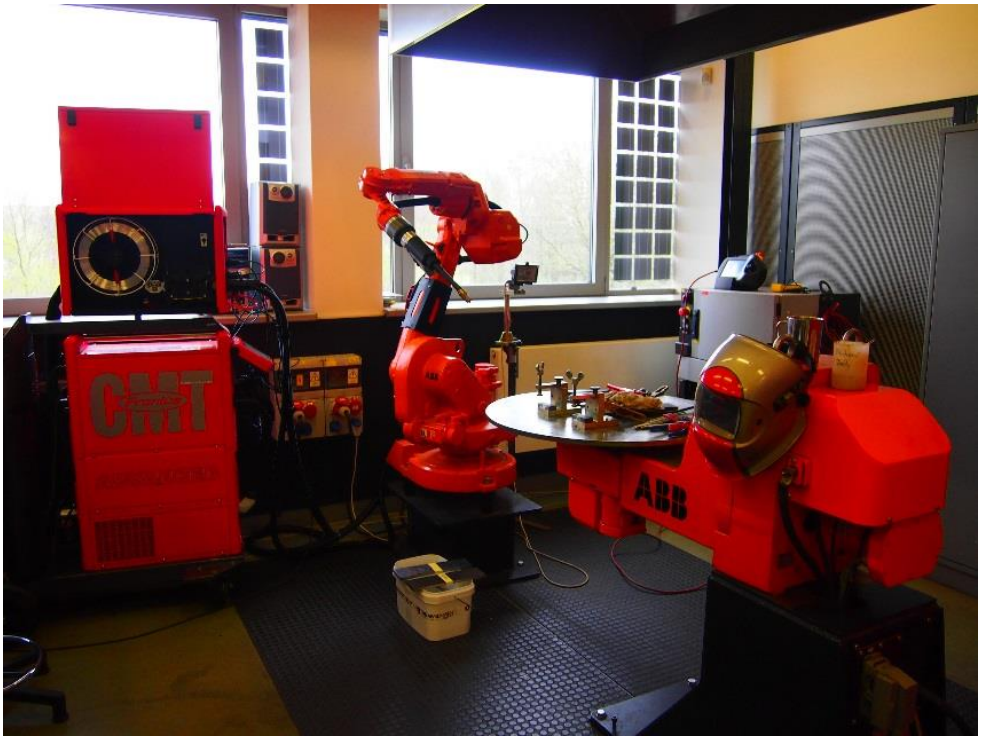

Figure 3.1: CMT welding process devices.

Table 14: Technical specification of used CMT welding unit. [33]

CMT Advanced 4000	
Mains voltage	3x400V +/-15%
Mains frequency	50/60 Hz
Main fuse protection	35 A
Degree of efficiency	88%
Welding current range	3 – 400 A
Working voltage	14.2 – 34 V
Protection class	IP 23
Weight	54.2 kg

3.2.2 Preparation of CMT-welded specimens

3.2.2.1 Types of welded materials

The materials mainly used in experiment were magnesium alloy (AZ31B), aluminum alloys (Al6065), and galvanized steel (DX51D). In order to establish test specimens, the three different CMT-welded specimens were fabricated as following;

1) The first type of CMT-welded specimen was welding AZ31B sheet with Al6065 sheet using AlMg 4.5 Mn of 1.2 mm diameter as filler material.

2) The second types of CMT-welded specimen was Al6065 sheet welded with DX51D sheet using 1.1 mm diameter CuSi3 as filler material.

3) The third type of CMT-welded specimen was welding Al6065 sheet with DX51D sheet using AlSi3 of 1.2 mm diameter as filler material.

Table 15 demonstrates the chemical compositions of all filler materials used in the test specimens.

Table 15: Chemical compositions of filler materials (w%). [59]

	Al	**Be**	**Cu**	**Fe**	**Mg**	**Mn**	**Si**	**Sn**	**Ti**	**Zn**
AlSi3	B	0.0003	0.3	0.6	0.05	0.05	6.0	-	0.2	0.1
AlMg 4.5 Mn	B	-	0.02	0.14	5	0.65	0.09	-	0.02	0.03
CuSi3	-	-	B	-	-	1.0	3.0	0.1	-	0.1

B = Balance

3.2.2.2 Shape of welded specimen

In progress of welding specimens, the lap-shear joint configuration was fabricated by two pieces of 300 mm x 80 mm x 1 mm sheet metal as shown in figure 3.2b. The arrangement of the sheet metals with respect to the weld torch is illustrated in figure 3.2a. Welding AZ31B sheet with Al6065 sheet, Al6065 workpiece was placed on the top of AZ31B workpiece in a lap configuration with an overlap distance of 30 mm. For Al6065 sheet welded with DX51D sheet, Al6065 workpiece was also placed on the top of DX51D workpiece with an overlap distance of 30 mm. The angle between the welding torch and the normal to the direction of weldment was 45° from the surface of base workpieces.

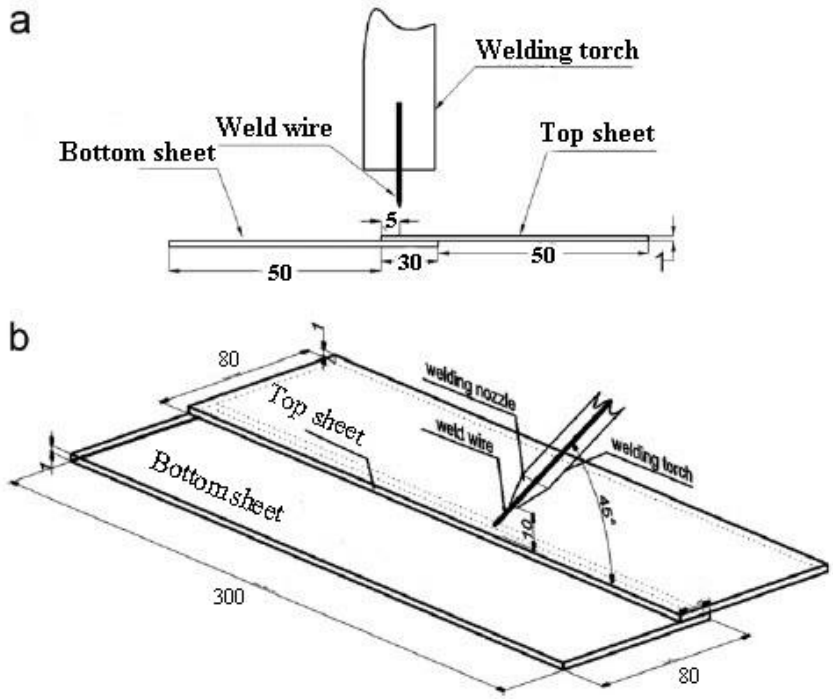

Figure 3.2: Schematics of lap-shear joint configuration of test specimen: (a) welding torch and workpieces layout, and (b) workpiece configuration.

3.2.2.3 Experimental configurations of CMT welding

Setting up the configuration of CMT welding process was indispensable to fabricate the test specimen. To examine the qualities of the CMT joint after welded by CMT welding, the several configurations of a CMT welding machine were employed to weld the specimens in different parameters as shown in table 16 listing the relevant configurations of CMT weldment used for welding the test specimen in this experiment. A *Fronius* arc welding system (*CMT Advanced 4000*) with 100% argon shielding gas at a flow rate of 15L/min was welding machine that was used to connect the sheet metals.

Table 16: Specified configurations of weldment in each sample.

Specimen number	Material	Welding current (A)	Welding velocity (m/min)	Filler material	Shielding gas
1	AZ31B – Al6065	73	4.6	AlMg4.5Mn	Argon
2	Al6065 – DX51D	110	6	CuSi3	Argon
3	Al6065 – DX51D	73	4.1	AlSi3	Argon
4	Al6065 – DX51D	61	3.8	AlSi3	Argon

3.2.3 Detection of acoustic emission signal during CMT welding process

In order to investigate the characteristics of elastic wave signals occurred during CMT welding process, the application of acoustic emission monitoring was considered to be used for detecting the acoustic emission signals in real-time during a test specimen being welded by CMT welding. The diagram of experimental equipment is illustrated in figure 3.3. The piezoelectric sensor, or acoustic emission transducer used in this experiment was broadband sensor which its specification is given in Appendix section. This sensor with type number of IDK-09-MU14 was manufactured by *DAKEL* (Czech Republic). The piezoelectric sensor was mounted on the test specimen as displayed in figure 3.3. To minimize the loss of detected signals, the counplant with high-temperature resistance was slightly coated on surface between piezoelectric sensor and surface of test specimen.

The acoustic emission signals monitored during welding process were magnified by the preamplifier, operated by the signal conditioner and then transferred to the data acquisition unit for analyzing the data. Technically, prior to measuring the signals using this equipment, it is very important to set up the configurations of acoustic emission devices and its software to function properly with the condition of experiment in order to record AE signals more effectively and precisely. Therefore, Hsu-Nielsen method, or Pentest must be conducted before beginning the experiment. The details of Hsu-Nielsen is described in the section of 3.6.6.

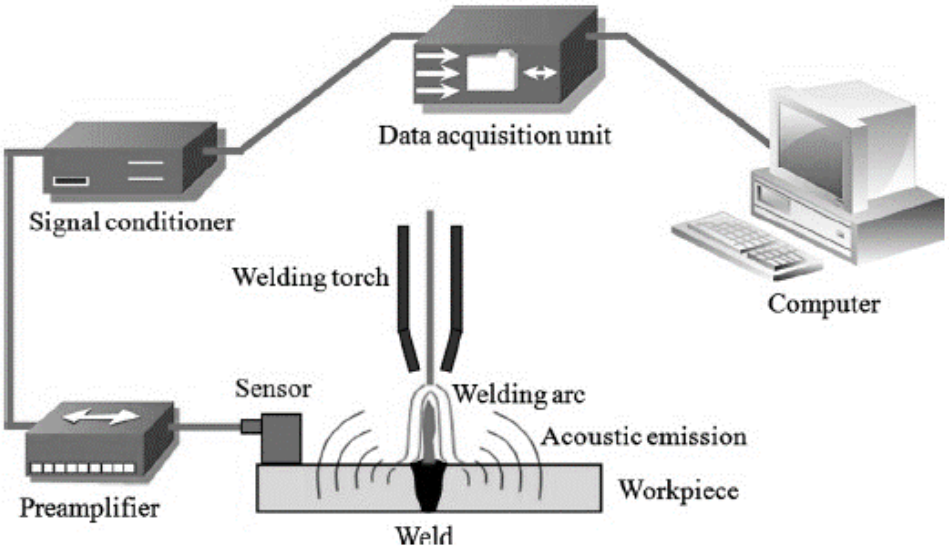

Figure 3.3: Schematic diagram illustrating the experimental equipment. [61]

A primary objective of this experiment was to monitor the elastic wave signals generated from the test specimen during both welding phase and cooling phase continuously. The time period of detecting the acoustic emission signals in cooling phase was approximately three minutes after welding phase was done.

Considering the position of an acoustic emission transducer mounted on the test specimen, for all specimens, the transducer was placed on the clean surface of a bottom specimen at the middle position and its location was away from the welding zone approximately 4 cm as shown in figure 3.4.

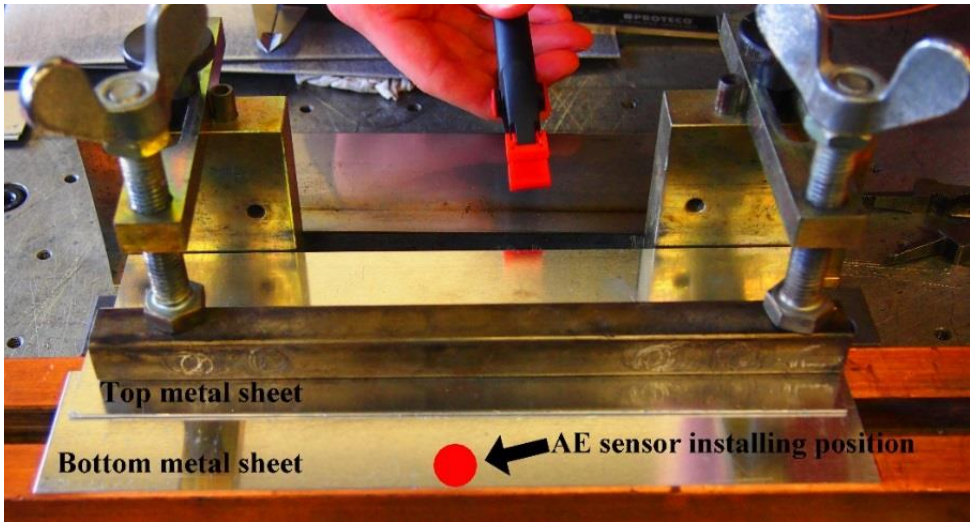

Figure 3.4: Showing the position of AE sensor placing on the specimen.

3.3 Evaluation of corrosion process using acoustic emission system

3.3.1 Description of artificial atmosphere simulator

In this study, to accelerate the corrosion process, salt spray chamber was employed to make the corrosive environment on the test specimens. Typically, salt spray test are suitable as corrosion protection test for rapid analysis for discontinuities, pores, and damage in organic and inorganic coating. It has been used for more than 90 years as accelerated tests in order to determine the corrodibility of nonferrous and ferrous metals as well as the degree of protection afforded by coating on a metallic base (Davis J. R. 2003).

According to ISO 9227, the corrosion test in artificial atmosphere in salt spray test, the salt solution was prepared by dissolving 5 ± 1 parts by weight of sodium chloride in 95 parts of distilled water, and the pH of the salt solution was provided in range of 6.5 to 7.2. The temperature of the salt spray chamber was controlled to maintain 35°C ± 2°C within the exposure zone of the closed chamber. Such condition of salt spray chamber was provided to test with all specimens in this experiment. The period of exposure of test specimens was defined to 96 hours continuously without interruption for periodic visual examination of specimens.

Figure 3.5 shows the general salt spray chamber used in this experiment which is comprised of 1) mist dispersion tower, 2) atomizer, 3) cover, 4) test chamber, 5) test specimen, 6) test-specimen support, 7) fog collector, 8) chamber, 9) air saturator, 10) air compressor, 11) solenoid valve, 12) pressure gauge, 13) solution tank, 14) temperature controls, 15) exhaust-treatment disposal, 16) air-outlet port, 17) drain-treatment disposal, 18) salt tray, and 19) heating elements.

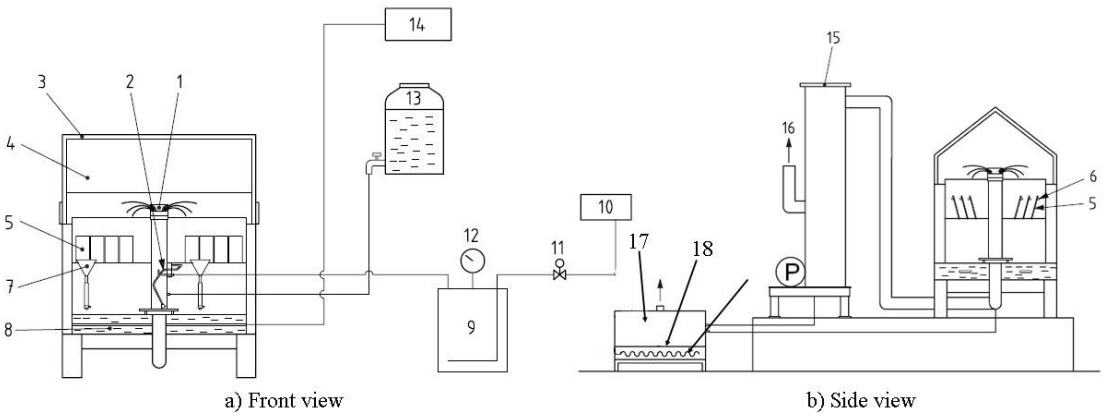

Figure 3.5: Schematic diagram showing typical salt spray chamber. [48]

In consideration of the location of test specimens placed in salt spray chamber, Test specimens were placed on a support which was made of inert material such as plastic. This support inclined test specimens with an angle of 20°±5°from the vertical, and make the unprotected face in each specimen.

3.3.2 Preparation of corrosion-tested specimens

After welding the test specimens by using CMT welding was complete, all welded sheet metals were cut into a small workpiece with dimensions of 80 mm x 20 mm x 1mm as represented in figure 3.6. Then, these small specimens were placed in the salt spray chamber for being the test specimens in order to check their corrosion process by using acoustic emission system.

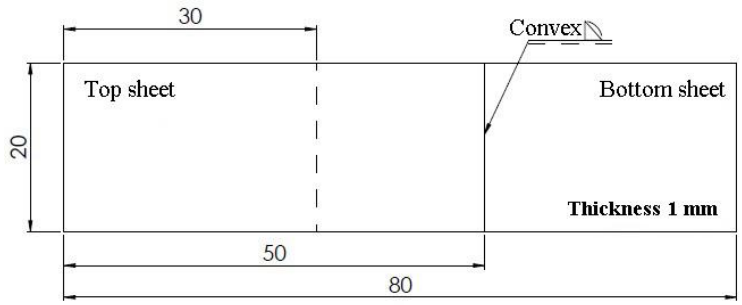

Figure 3.6: A photo illustrating dimensions of CMT-welded specimen tested in salt chamber.

All specimens were thoroughly cleaned with specific solution before tested in salt spray chamber, a hydrocarbon solvent with a boiling point between 60 °C was used for removing all evidence of dirt, oil, or other foreign matter influencing the result of the corrosion process from the test specimens. After cleaning, all specimens were rinsed with fresh solvent and then dried by hot air.

3.3.3 Acoustic emission monitor of corrosion process

To study the development of corrosion process of test specimens by using the non-destructive testing, acoustic emission technique was employed to investigate and study the characteristics of acoustic emission signals generated from CMT-welded specimens during corrosion testing. Figure 3.7 shows both the acoustic emission equipment and the salt spray chamber that were used for testing all specimens in this experiment. This testing progress was implemented in non-destructive testing laboratory at Department of

Technology and Automobile Transport, Faculty of AgriSciences, Mendel University in Brno.

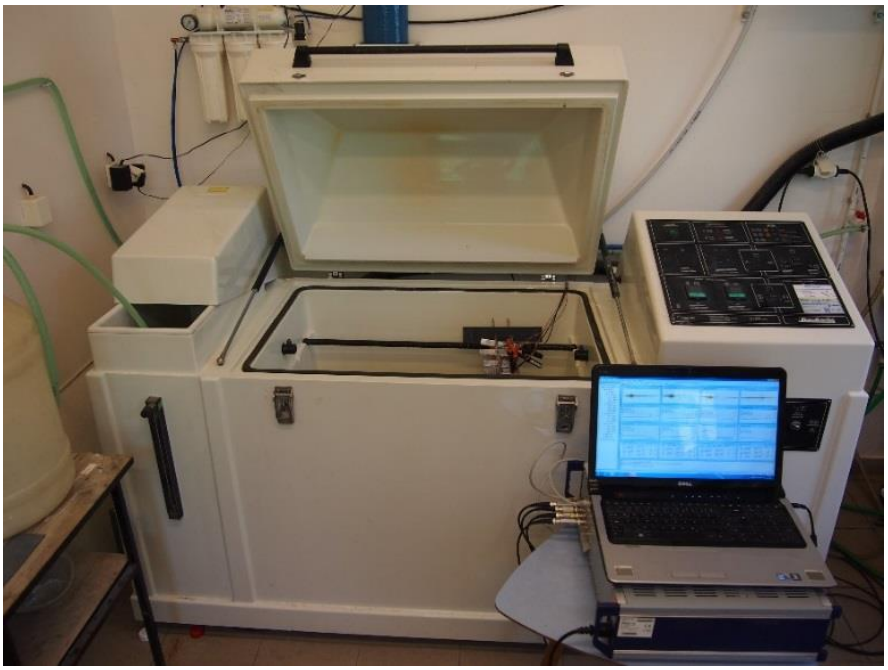

Figure 3.7: Setting up acoustic emission system with salt spray chamber for testing the test specimen.

Due to the sensitive of acoustic emission equipment to corrosive environment, particulary in acoustic emission sensor, protecting the sensor during testing was thoroughly considered in order to not only prevent the damage of senosor, but also keep it functioning properly. Therefore, in order to forbidden unexpecting situations happening on the sensor, the high corrosive resistant substance was employed to cover the area of acoustic emission sensor that was directly exposured to the corrosive solution during corrosion testing as depicted in figure 3.8a.

For installing acoustic emission sensor on the surface of test specimen in this experiment, it is very important to select the properly position where the sensor, or transducer can detect the signals from test specimen effectively and precisely. Because of each CMT-welded specimen consisted of two different materials, therefore, the sensor was mounted on the surface of material which was more anode metal, because the electropotential difference between the dissmilar metals is the driving force for attacking on the anode member of the galvanic couple. The anode metal dissolves into the eletrolyte, and deposit collects on the cathodic metal.

(a) AE sensors covered protection substance. (b) Installing the sensor on specimen.

Figure 3.8: Using and mounting AE sensor on test specimens.

Figure 3.8b shows installing acoustic emission sensor on the surface of test specimen in this experiment. A plastic gripper was used to maintain the position of the sensor on the surface of test specimen througout experiment period. From our previous experiments, it indicated that using a plastic gripper for keeping the position of the sensor during corrosion testing of salt spray chamber was effect way to detect acoustic emission signals from the test specimen over experimental time.

3.4 Tensile test of CMT-welded specimens with AE monotoring

3.4.1 Description of tensile testing machine

Investigating the mechanical properties of CMT-welded specimens was carried out by means of uniaxial tensile testing, which is the most commonly used for obtaining the mechanical characteristics of isotropic materials. In this part of experiment, both CMT-welded specimens with corrosive condition and CMT-welded specimens without corrosive condition were tested in tension test by using the *ZDM5/51* universal testing machine as shown in figure 3.9. This machine can provide a maximum tension load of 50 kN with serveral speed rates of tension. However, to couduct the experiment properly, the speed rate of tension test was specified to be 20 mm/min for all test specimens.

Figure 3.9: Used tension machine in this experiment.

To function the tension machine effectively, personal computer with *M-Test 1.77* software was utilized to record and display the mechanical property data of test specimens in real-time. Technically, load vs. displacement curves was obtained during the experiment until test specimen reached its rupture point. Afterward, the raw data from *M-Test 177* software was converted into the text file format (.txt) in order to be the compatible file for operating with *DAESHOW* software, which is the result-displaying program of acoustic emission monitoring system, to integrate between tension force data and acoustic emission data together as result chart. To achieve this study, the experiment of tension test was completely implemented in Department Wood Science, Faculty of Forestry and Wood Technology, Mendel University in Brno.

3.4.2 Preparation of specimens for tensile testing

In preparing the test specimens, the main intention of this study was to compare the mechanical properties of the test specimens which were corrosive specimens and non-corrosive specimen. Therefore, the test specimens were divided into two groups; first was the corrosive specimens, and second was the non-corrosive specimens. Preparation of

both specimens was already mentioned in 3.3.2 section. The ten pieces of test specimens being corroded in salt-spray chamber for 96 days were tested by tension test, and the ten pieces of non-corrosive specimens were directly performed with tension test.

3.4.3 Description of AE monitoring in tensile testing

In order to detect acoustic emission signals during tensile test in both corrosive and non-corrosive specimens, the acoustic emission signals generated during tensile deformation were recorded by using AE system supplied by *DAKEL* company (Czech Republic). Schematic of the experimental set up is illustrated in figure 3.10. A piezoelectric sensor being a broadband frequency, a preamplifier with 35 dB gain, and as acquisition were used to record the AE signals from the test specimen during tension test. The sensor was tightly fixed on the surface of test specimen close to its welding zone by using a gripper. The silicon grease was used as couplant to reduce the attenuation of AE signals between acoustic emission sensor and specimen surface. The threshold was chosen not to record external noise during the test. The AE signals were digitized at a sampling rate of 4 Mega sample per second.

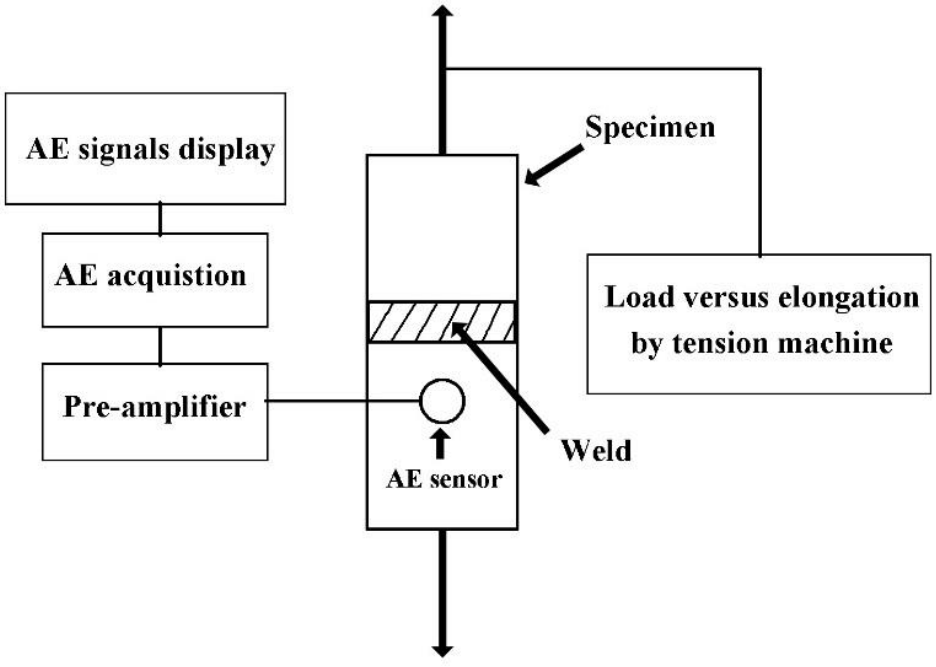

Figure 3.10: Schematic illustrating acoustic emission system set up with tension test.

3.5 Evaluation of fatigue behavior of magnesium alloy

3.5.1 Description of high cycle fatigue testing machine

Studying high cycle fatigue behavior of AZ31B magnesium alloy was conducted to particularly investigate the fatigue strength of magnesium alloy. Thus, resonant testing machine or *CRACKTRONIC* (*RUMUL*, Switzerland) as depicted in figure 3.11a was used to test the magnesium specimens by using dynamic bending load with operating frequencies of 40 – 80 Hz. This machine is a dynamic testing machine operating in full resonance. The concept of the drive produces an oscillating motion of rotation. The test specimen itself is part of the spring/mass system and influences with its stiffness and the additional masses.

In the experiment, the test specimens were individually loaded under bending stress amplitudes of 60, 80, 90, 119, 139, and 156 MPa with alternating symmetric cycle which had the stress ration of -1.

Moreover, in order to monitor acoustic emission during fatigue testing, acoustic emission device *XEDO* (*DAKEL*, Czech Republic) as shown in figure 3.11b was performed to record the signal generated from test specimens. Both acoustic emission device and high cycle fatigue testing machine were mainly implemented at Department of Condition Monitoring, Faculty of Mechanical engineering, Brno University of Technology.

(a) *(b)*

Figure 3.11: Experimental set up for high cycle fatigue testing (a) Resonant testing machine (cracktronic) (b) AE system with cracktronic machine.

3.5.2 Material preparation of fatigue testing

The fatigue specimens of magnesium alloy were thoroughly machined with shape characteristics which maximize the fatigue life of a metal. Figure 3.12 represents the dimensions of a fatigue specimen in direction of front view with section C-C, and isometric view. The diameter and radius of curvature at the middle part of the fatigue specimen were 10 mm and 35 mm, respectively. To have the good condition of the test specimen, the metal surface at middle part of fatigue specimen was highly polished to provide the surface condition which enabled the best fatigue life.

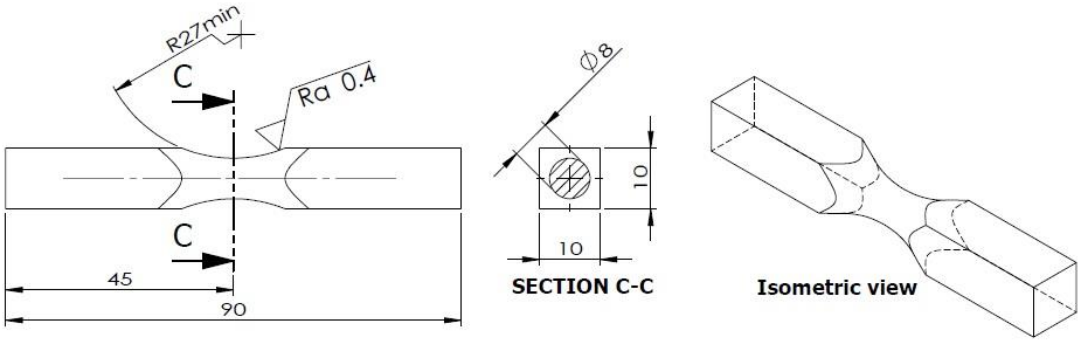

Figure 3.12: Dimensions of magnesium alloy specimen.

In the fatigue testing, the total number of fatigue specimens were 18 pieces and they were separated into three groups as following;

1) Six pieces of fatigue specimen without exposing corrosion process.
2) Six pieces of fatigue specimen with exposing corrosion process for two days.
3) Six pieces of fatigue specimen with exposing corrosion process for four days.

The salt spray chamber was used to accelerate the corrosion process for second group and third group of test specimens. The test condition of salt spray chamber was configured the same condition as described in section of 3.3.1. After corrosion process was complete, all fatigue specimen were tested by high cycle fatigue testing machine in order to create the S-N curve in each group of fatigue specimens.

3.5.3 Description of AE monitoring in fatigue testing

Monitoring acoustic emission signals from test specimens during fatigue testing was implemented by using an acoustic emission sensor IDK-09-MU14 (*DAKEL*, Czech Republic). After the specimen was fixed on gripping unit of fatigue testing machine as represented in figure 3.13b, an acoustic emission sensor was then mounted on an one end of test specimen by using glue as shown in figure 3.13a. In acoustic emission process,

detected signals from acoustic emission sensor was amplified by 35 dB preamplifier and then analyzed by acquisition unit *XEDO* (*DAKEL*, Czech Republic). Normally, *XEDO* analyzer operates its system in frequency range of 80 – 550 kHz approximately and this property makes the system suitable for monitoring in different sources of acoustic emission signal.

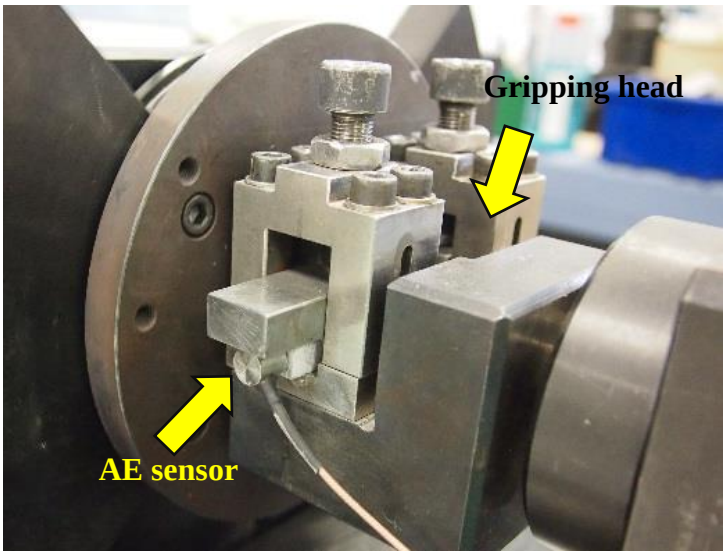

(a) Location of AE sensor

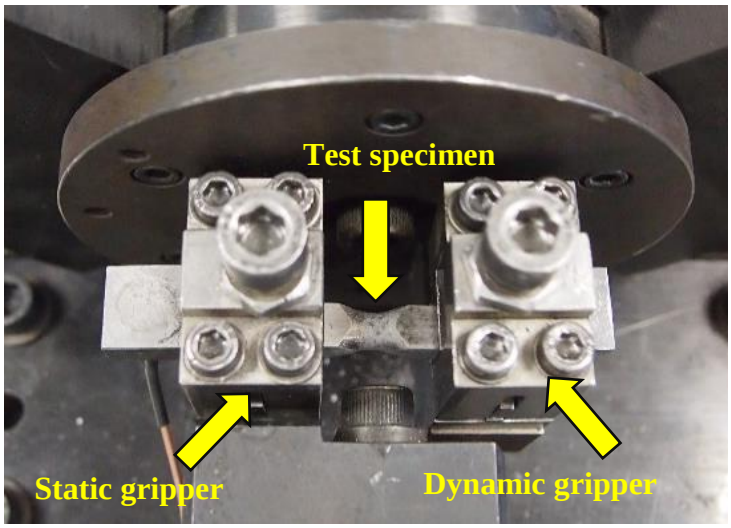

(b) Location of test specimen

Figure 3.13: Positioning the sensor on a test specimen during fatigue testing.

The interesting data from bending fatigue testing operating with acoustic emission monitoring were comprised of two parts; first part was the data getting from high cycle fatigue testing that consisted of loading frequency data of test specimen and the number of cycle of test specimen. Second part was the data recorded from acoustic emission device that showed the accumulative event number of signal, count number and root mean

square (RMS) of detected signal. Both two parts of data eventually were used to estimate the relation between deformation of test specimen and detected signals of test specimen due to bending fatigue testing.

3.6 Acoustic emission system

3.6.1 Acoustic emission acquisition

To analyze and evaluate the acoustic parameters properly, Modular system *DAKEL-XEDO* (Czech Republic) as shown in figure 3.14 was mainly used as AE acquisition unit in order to convert the electrical signal into digital signals. Technically, It can be used as a single unit or multiple units (up to 15 various input cards) depending on the type of investigation process. *XEDO* measurement module is designed to have the Ethernet 100 interface with 1 μs accuracy for easy communicating of both passive piezoelectric and other active sensors with integrated 12/24 V preamplifier. The sampling rate of signals from a sensor is usually operated at 2 – 8 MHz with 12 bit resolution and it is completely digital processing. Changing the gain of AE signal can be done by computer software comfortably.

The relevant parameters of AE signal getting from the *DAKEL-XEDO* basically consist of Root Mean Square (RMS), first counts number, second counts number, accumulative event number, and AE sample with arrival time, rise-time, duration time, etc. all these parameters are the main value to be analyzed in the experiments.

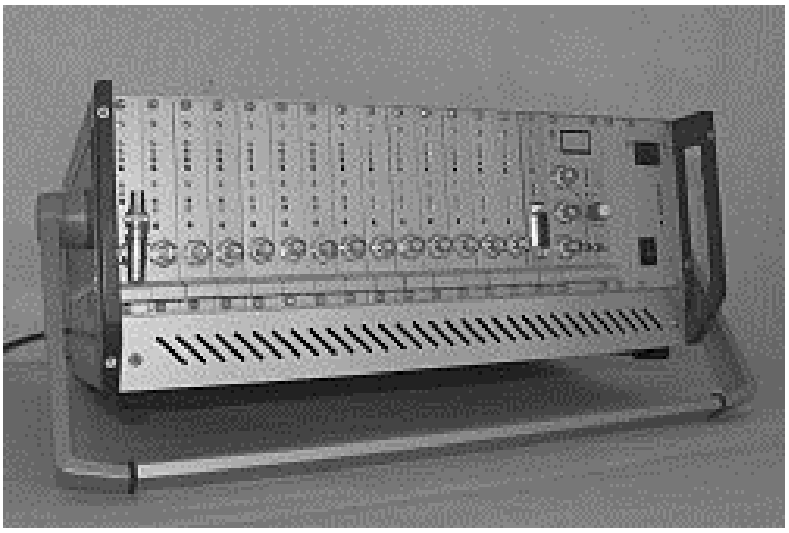

Figure 3.14: Acoustic emission acquisition unit utilized in the experiment. [22]

3.6.2 Acoustic emission sensor

Selecting acoustic emission sensor is very important to detect the acoustic emission signals properly from the signal resources. Therefore, IDK-09-MU14 acoustic emission sensors were used to monitor the AE signals from all experiments in this dissertation, since this type of AE sensor provided the wide beneficial for monitoring the elastic wave signals in different tasks. The general technical specifications of used acoustic emission sensor in the experiments are listed in table 17.

Table 17: Specification of IDK-09-MU14 AE sensor. [22]

Item	description
Model	IDK-09
Case material	Stainless steel
Diameter / Height	9 / 9 mm
Face material	Ceramic
Contact area	6 mm
Output	Coaxial cable of 1.7 mm dimension with BNC connector
Piezoceramic material	PZT class 200
Operating temperature	-20°C to +95°C
Recommended applications	Laboratory and industrial using on small objects
Integrated preamplifier	N/A
Mounting Methods	Glue-hold, magnetic holder

Technically, the sensitivity of the acoustic emission sensor is depended on the frequency range of detected elastic weave signal. Thus, knowing the frequency range of signal-generating resources before running the experiment can be useful for operators to choose the suitable acoustic emission sensor.

The frequency response of IDK-09-MU14 acoustic emission sensor used in the experiments is detailed in appendix section of dissertation. It obviously shows that the used AE sensor is capable of detecting AE signals effectively in frequency range of 50 – 500 kHz.

Figure 3.15a represents the typical appearance of IDK-09-MU14 acoustic emission sensor used in the experiments. Occasionally, it is important to use the acoustic

emission sensor with extension cable because the cable of acoustic emission sensor is rather short. Therefore, using extension cable will be useful when monitoring the signals is distant measurement. General extension cable used in experiment is shown in figure 3.15b.

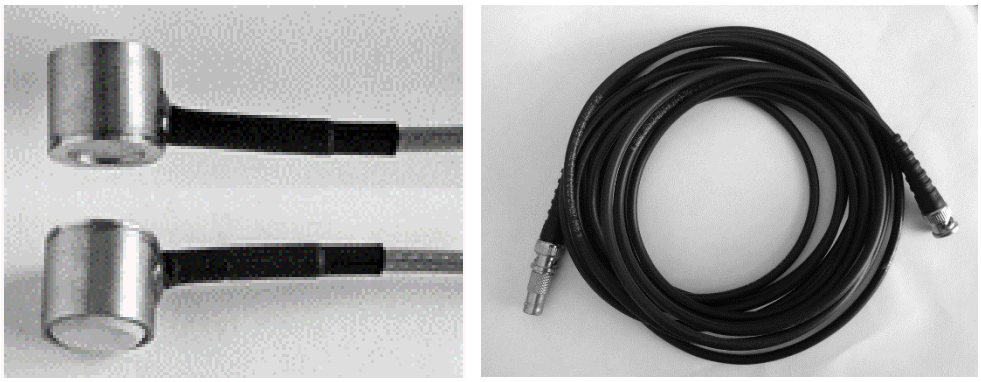

a) AE sensor used in the experiment. *b) extension cable.*

Figure 3.15: Typical acoustic emission sensor and extension cable.

3.6.3 Acoustic emission preamplifier

Practically, acoustic emission sensor produces a high impedance alternating current (AC) signal unsuitable for transmission over long cable. Therefore, preamplifier transforms the high impedance signal to a low impedance signal. Furthermore, the detected signal of sensor is amplified to a voltage range suitable for the acoustic emission acquisition.

To obtain the high quality of acoustic emission signals, a preamplifier of 35 dB manufactured by *DAKEL* company (Czech Republic) was mainly integrated into IDK-09-MU14 sensor to magnify and improve the detected signals. Table 18 represents the technical specification of the preamplifier used in the experiment.

Table 18: Technical parameters of the preamplifier. [22]

Item	Description
Gain	Approximately 35 dB
Power voltage	12 VDC to 35 VDC
Mode of power feeding	Via output coaxial cable
Current consumption	3 mA at 12V, 7 mA at 35V
Working temperature range	-20°C - 85°C
Input / output	BNC female / BNC female or male

3.6.4 Acoustic emission monitoring software

The specific software named *DAEMON* was completely used to record and display the detected signals monitored from acoustic emission resources in real-time. It have been developed by *DAKEL* company (Czech Republic). In general, this software is operated with OS windows with standard drivers and with sockets 2 extension [22].

Figure 3.16 demonstrates the graphical user interface of *DAEMON* software with displaying acoustic emission signals detected during experiment. The main display windows are comprised of map system window, oscilloscope window, count number and RMS window, signal trend window, and another parameter window. This software not only supports a monitor of an individual sensor, but also it is provided for working with multiple sensor system. The important step of using this system is setting up the configuration of the system for each experiment.

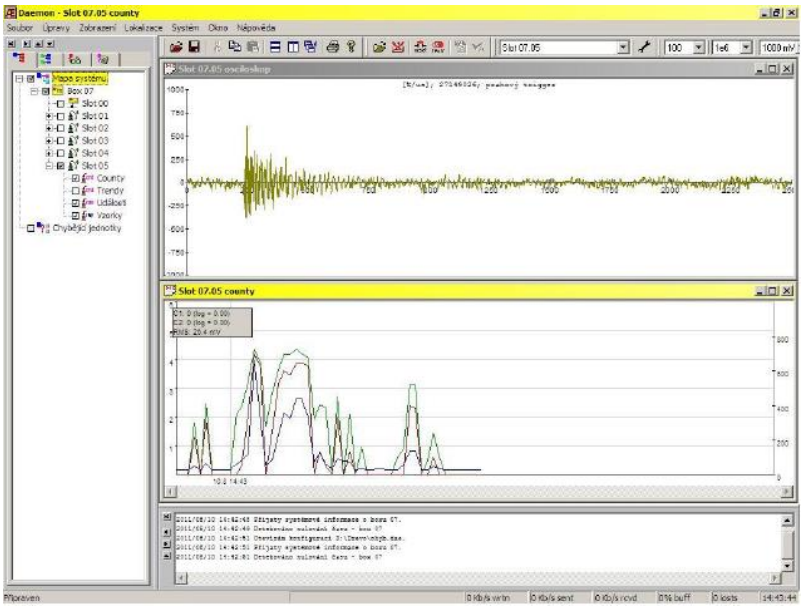

Figure 3.16: Graphical interface of DAEMON software. [102]

In consideration of the configuration system in *DAEMON* software, it is essential to set up the parameters in configuration window as shown in figure 3.17 to be suitable with the experimental condition. Practically, prior to do the actual measurement, Pentest method as described in 3.6.6 is conducted on test specimen in order to find the suitable parameters in configuration system. The necessary parameters in configuration window consist of digital amplifier, count thresholds, saving interval, sampling rate, etc.

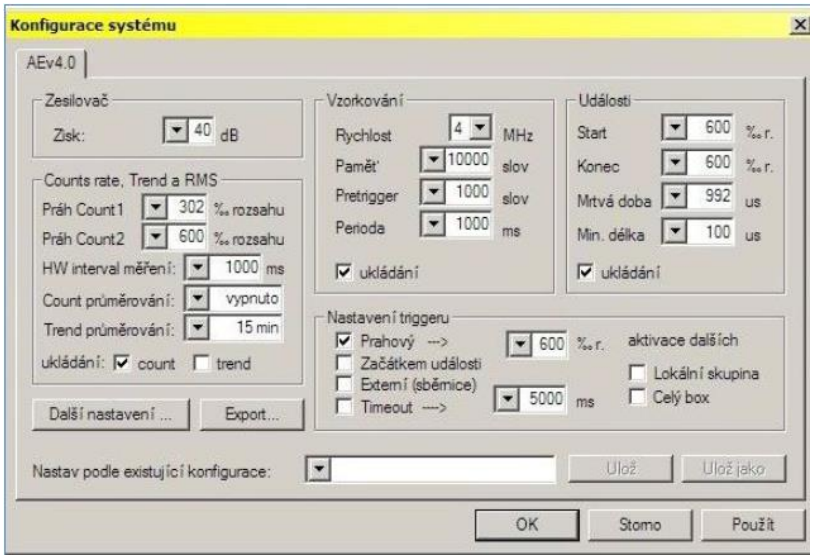

Figure 3.17: Photo showing AE configuration window. [102]

Technically, the adjusting the gain of detected signals is based on the density of the acoustic emission signal. The available value of magnifying the gain is ranged 0-100dB. Sampling rate value is changeable within 2MHz-8MHz. For Count 1 and Count, they can be set their values in either mV or ‰.

3.6.5 Acoustic emission analyzer software

To analyze and display the experimental results, acoustic emission analyzer software called *DAESHOW* (*DAKEL*, Czech Republic) was used to evaluate the acoustic emission data recorded by the *DAEMON* software.

The functions of *DAESHOW* can be divided into three modes: continuous data analysis, sample analysis, and events (localization) as illustrated in figure 3.18, and figure 3.19. In general, the data structure for any of these is as simple as follows: Project/Directory/Box/Slot/Property. Principle *DAESHOW* features include [102]:

- Export of binary files into plain text format that is most widely used for other analysis softwares, e.g. *MatLab*, *Grapher*, *Maple*, etc.
- Time-dependent plots of individual properties: Counts, RMS.
- Spectral analysis of samples produced by the *XEDO* analyzer units. Several transformations are available including the PSD (Power Spectral Density). Custom transformations may be implemented using DLL (Dynamic Link Library) modules.

- Localization of acoustic emission events within a specific body. Again, default linear localization methods can be easily enhanced with custom DLL modules.
- Output graphics can be exported as images (Windows metafile) and inserted into word processing program similar to Windows Wordpad, From there, the files are saved in common Rich Text Format (.RTF). The output can be pasted into other applications (MS Word, MS Excel, MS PowerPoint) using Windows clipboard.

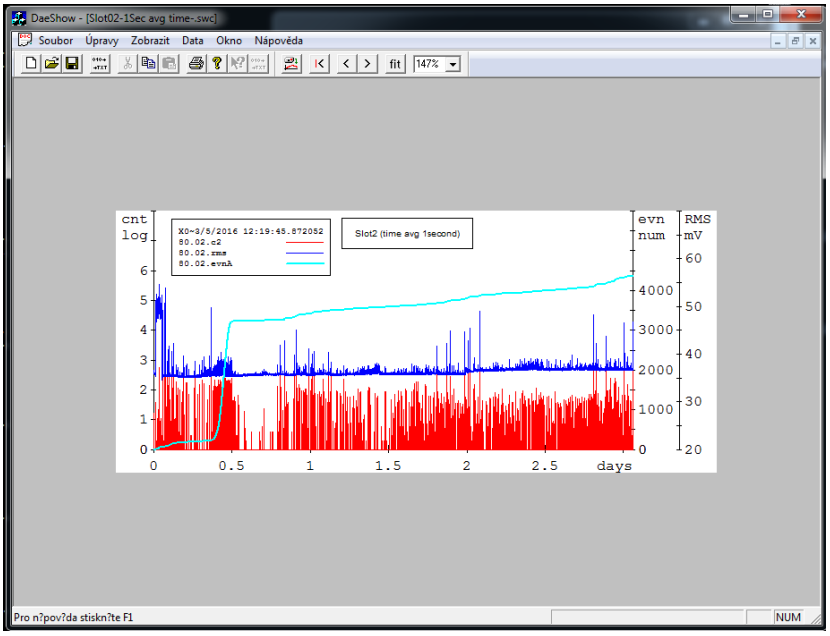

Figure 3.18: Continuous data mode displayed in DAESHOW software.

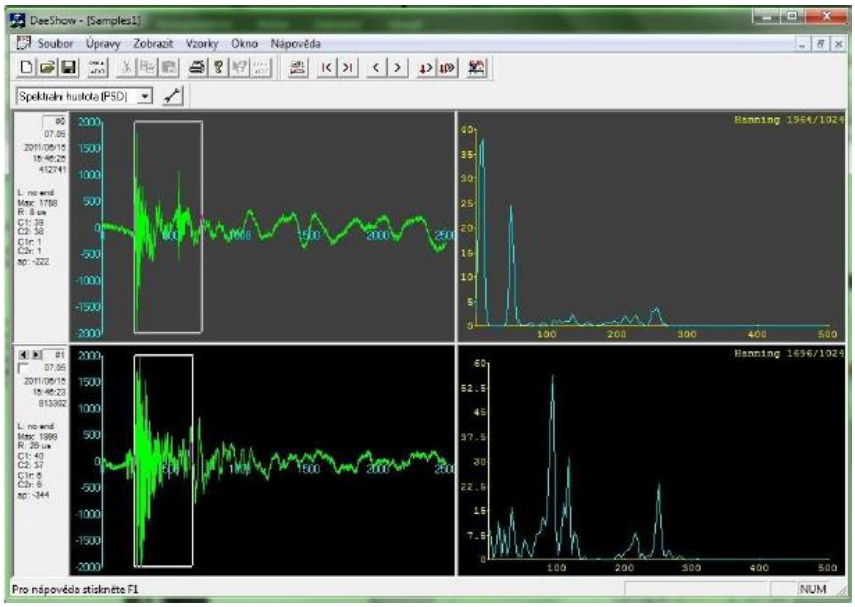

Figure 3.19: Signal sample mode shown in DAESHOW software. [102]

3.6.6 Calibration of acoustic emission system

Prior to measure the elastic wave signals by using an acoustic emission sensor, calibrating the sensor before actual measurement is very necessary to verify that the used sensor is in well contact with the surface of test sample being monitored as well as examining the system of acoustic emission device to be ready for being operated.

Therefore, to calibrate the sensor and acoustic emission system, Hsu-Nielsen method, or Pentest was firstly implemented to simulate an individual acoustic emission event by using the fracture of a brittle graphite lead in a suitable fitting as shown in figure 3.20a. As can be seen from figure 3.20b, the 2H pencil lead having a dimension of 0.5mm (alternatively 0.3mm) with length of 3±0.5mm from its tip is pressed against the surface of test specimen in order to generate the acoustic emission signals. Consequently, the characteristics of these generated AE signals are used for considering to set up the configuration of acoustic emission monitoring software (*DAEMON*) in order to eliminate the unwanted signals such as, environmental noise, and also get the suitable recorded signals in each experiment.

As aforementioned description, setting up the configuration in acoustic emission monitoring software (*DAEMON*) is depended on the situation and condition of each experiment. Therefore, it is very important to conduct Pentest all the times before the real test would be implemented. The details of the used configurations of *DAEMON* in each experiment were described in the result sections.

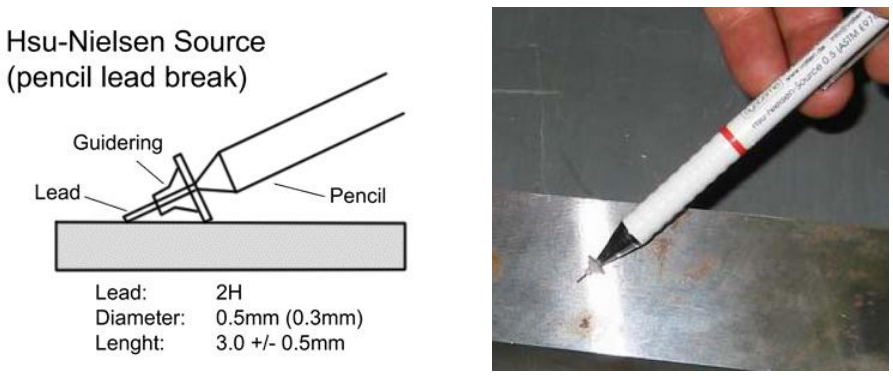

(a) Schematic diagram of Hus-Nielsen test. (b) Testing Hsu-Nielsen on test sample.

Figure 3.20: Hsu-Nielsen calibration method. [25]

CHAPTER 4: RESULTS AND DISCUSSIONS

4.1 Examinations of CMT-welded specimens and CMT process

4.1.1 Welded joints in different welding parameters

The weld appearances of CMT-welded specimens were observed after CMT welding process was done. Figure 4.1 represents macro-photographs of specimens welded in different welding parameters. The welding parameters used are already listed in table 16 in third chapter. As can be seen in figure 4.1a, it was found that welding AZ31B sheet to Al6065 sheet with AlMg4.5Mn as filler material was not successful. The AZ31B sheet was suddenly melted during welding process. It was expected that welding temperature used in this specimen was much higher than the melting point of AZ31B sheet (470 °C), and this might mainly cause incomplete fusion occurring on this specimen. Moreover, the back surface of Al6065 sheet welded with AZ31B sheet was completely deformed along welded zone as shown in bottom view of figure 4.1a.

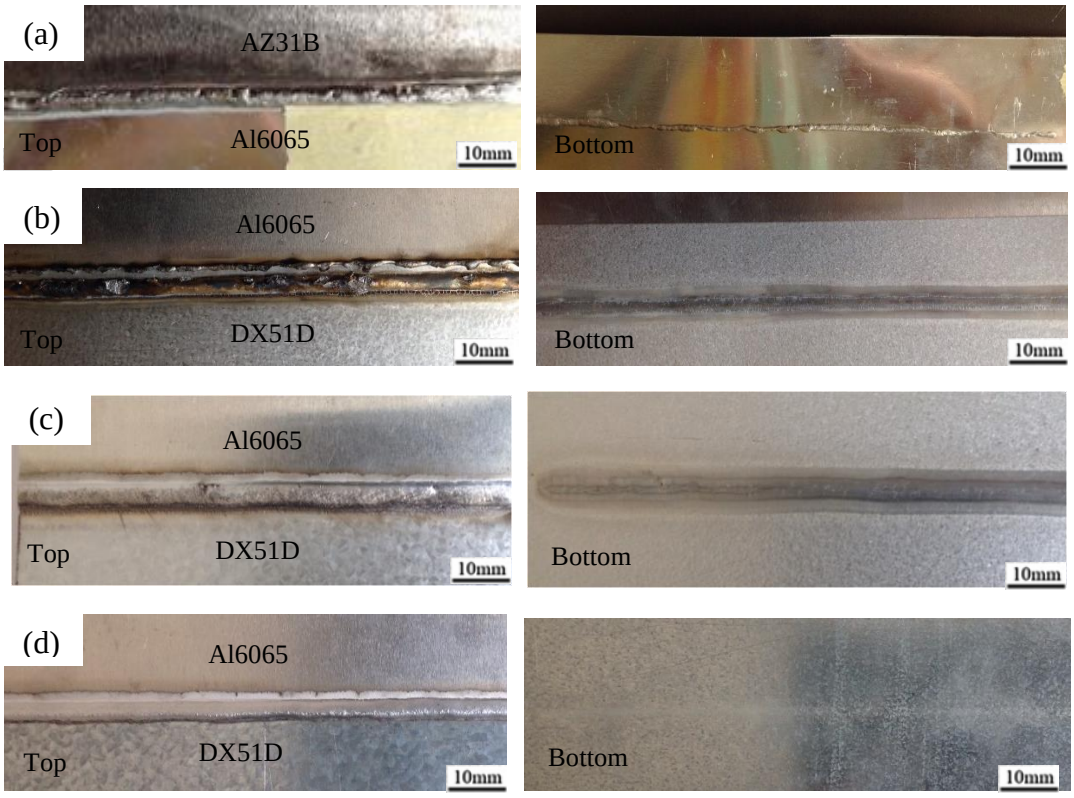

Figure 4.1: Macro-photographs of the welds in different welding parameters.

For jointing Al6065 sheet to DX51D sheet using CuSi3 as filler material, it was noticed that the weldment of this specimen was totally destroyed because of using

extreme electric current in welding process. As can be observed in figure 4.1b, the burning color appeared on weld surface, which indicated that weld was oxidized and burned severely, especially in the Al6065 sheet that had melting point value less than the melting point value of DX51D sheet. In opposite side of specimen, the zinc protection layer of specimen became thinner as shown in bottom view of figure 4.1b because of using too high current for welding the specimen.

In case of welding Al6065 sheet to DX51D sheet using AlSi3 as filler material, there were two different welding configurations used to prepare these welded specimens. Their results could be demonstrated that welding the specimen with welding configuration that had the welding current of 61 A, and welding speed of 3.8 m/min was suitable for welding Al6065 sheet to DX51D sheet in this experiment, because the good formation of weld metal was established on the weld surface, and also the zinc protection layer on the back site of specimen did not appear to be damaged as shown in figure 4.1d. On the other hand, the specimen welded with current of 73A, and welding speed of 4.1m/min did not show good condition after passed welding process, because the weld beads had a large amount of porosity and burned area around the surface of weld metal as shown in figure 4.1c and figure 4.2a. Moreover, the zinc protection surface on its back site of weldment was also destroyed as represented in figure 4.2b and this made it difficult to be a good weldment.

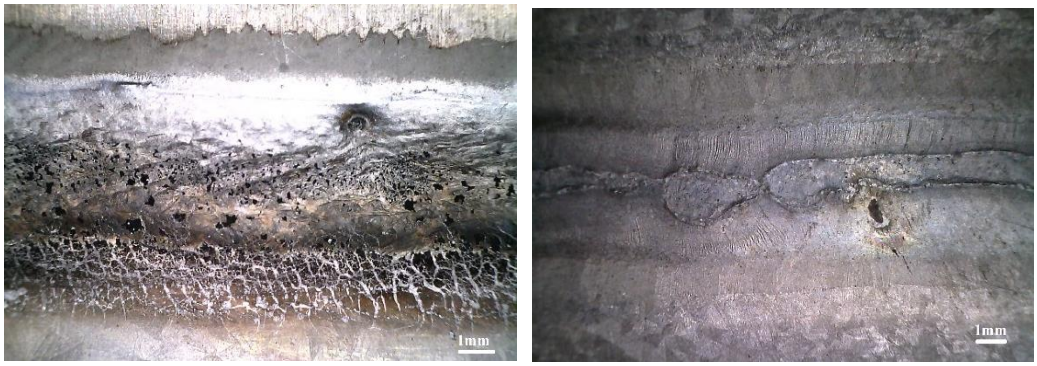

(a) *(b)*

Figure 4.2: Micro-photographs of welding Al6065 to DX51D sheet at 73A welding current and 4.1m/min welding speed, (a) top surface of weldment, (b) back site of weldment.

According to the appearances of specimens after welded in different welding configurations, the experimental results indicated that setting up the welding configurations on welding machine, particularly in welding current, was important factor

for joining the dissimilar metals. With high welding current, the welded specimen tended to be damaged by excessive temperature, resulting in the strength of welded specimen decreased and the protection layer of welded specimen destroyed. Therefore, selecting the welding parameters was first thing that the users must be aware in order to avoid and prevent the improper conditions occurring on the welded specimen.

4.1.2 Characteristics of AE signals detected during CMT welding

Prior to measure acoustic emission activity during CMT welding process, it is very important to find the suitable configuration for being configured in *DAEMON* software, Therefore, Hsu-Nielsen method, or Pentest was conducted. After performing the Pentest, the suitable acoustic emission configuration inputs for detecting the signals in this study were arranged in table 19. These parameters were configured into the *DEAMON* software in order to record and store acoustic emission data properly.

Table 19: Relevant used parameters in the DAEMON software.

AE configuration input	Value
Gain (amplifier)	45
Data-saving interval	100 ms
Threshold level of count 1	400 ‰.r
Threshold level of count 2	500 ‰.r
Sampling frequency	4 MHz
Threshold level of AE event	350 ‰.r

4.1.2.1 AE signals detected from welding AZ31B to Al6065 sheet

Test weld 1 was intended to weld AZ31B to Al6065 sheet by using AlMg45Mn as filler material. After welding process was complete, the quality of weld was unacceptable because the weld was not incomplete fusion. Considering AE response of welding process in Test Weld 1, the acoustic result was revealed that there was a high value of acoustic emission signal generated in welding phase, and acoustic emission gain was gradually decreased in cooling phase as illustrated in figure 4.3.

Many difficulties were encountered with monitoring acoustic emission signal in welding phase. The result of welding phase showed that the acoustic activity at high signal gain was generated throughout whole welding period. It was supposed that this high signal occurred from several reasons such as, the high cyclic movement of welding wire

during operating process, the electric arc between welding wire and surface of specimen, and the material deformation of both welded specimen and weld metal. This could not be easily differentiated each of them from whole acoustic emission activities of the weldment using the available device. However, the characteristic of detected signals in cooling phase of Test Weld 1 indicated that it was more likely to be success to monitor acoustic emission signals during cooling phase, because, in cooling phase of Test Weld 1, the base metal, especially in magnesium sheet, was severely damaged from excessive welding temperature. From this damage, it was supposed that the hot cracking of base metal could be the main consequence of generating acoustic emission signals during cooling phase.

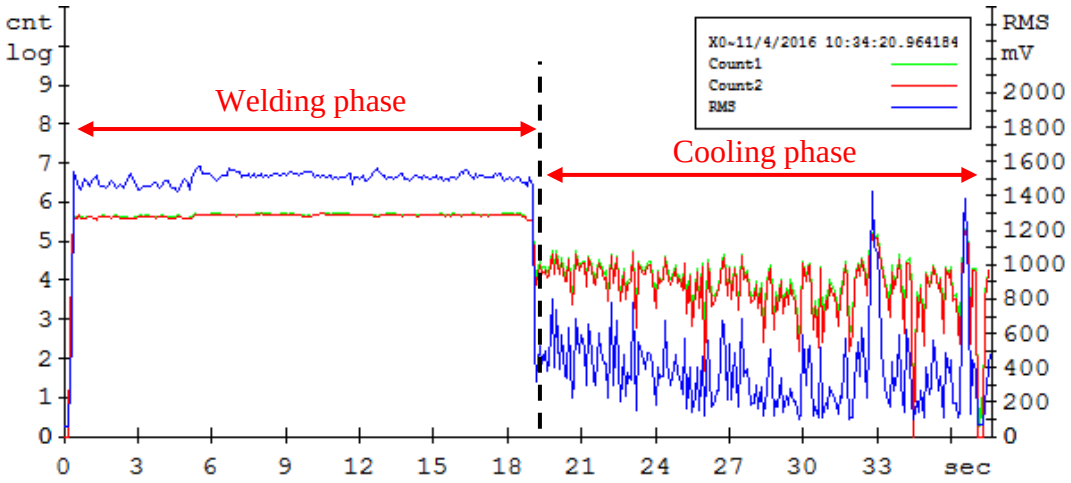

Figure 4.3: Pattern of acoustic emission signals detected from Test Weld 1.

According to acoustic emission signals detected in Test Weld 1, the analysis of time domain and frequency domain of detected signals were considered to more understand the details of acoustic emission signals emitted from CMT welding process. Normally, the time domain plot represents time in x-axis against amplitude of detected signal in y-axis. For frequency domain plot, the PSD (Power Spectral Density) function was used to characterize the frequency versus amplitude of spectrum of detected signals.

Figure 4.4a represents the time domain plot of a random detected acoustic emission signal in welding phase of Test weld 1. It was indicated that most of the detected acoustic emission signals in welding phase were continuous signal with high amplitude ranged from 500 mV up to 2000 mV. Figure 4.4b shows the result of power spectral density, or frequency domain analysis from the detected signal in figure 4.4a. As can be seen from frequency domain plot, the maximum power spectral density value of this continuous signal was equal to 3250 $Volt^2/Hz$ at signal frequency of 80 kHz, and also

there were other signals with low power spectral density value appearing in range of 125 kHz, and 280 kHz.

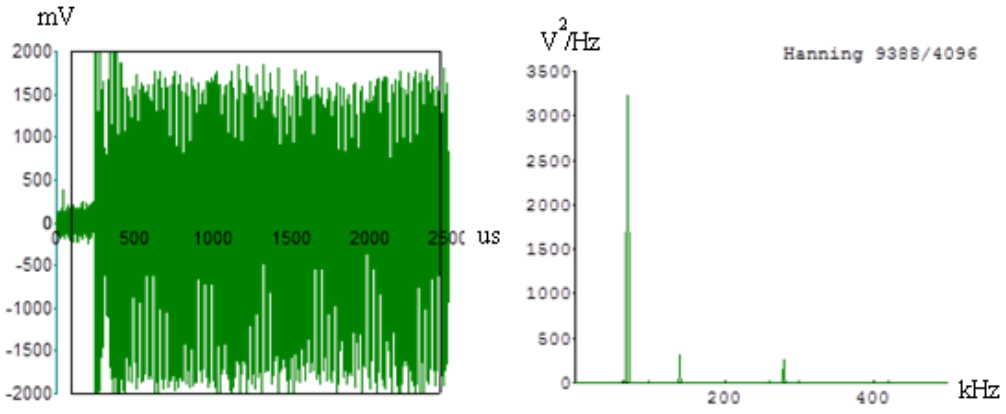

(a) *(b)*

Figure 4.4: Time domain (a) and frequency domain (b) of a random AE signal during welding phase of Test Weld 1.

For acoustic emission signal detected in cooling phase of Test Weld 1, the characteristic of this detected signal was completely different shape from the detected signal in welding phase as mentioned above. Figure 4.5a illustrates the typical signal emitted from Weld Test 1 during cooling phase. Most of detected signals in cooling phase show the characteristic of burst signal, and the frequency domain of this signal are shown in figure 4.5b. The frequency of this signal could be monitored from 100 kHz to 450 kHz. The maximum amplitude of spectrum of the detected signal was about 120 $Volt^2/Hz$ at signal frequency of 220 kHz.

Based on the acoustic emission results of Test Weld 1, it was obviously shown that the characteristic of detected signals in both welding process and cooling process was different. However, these detected signals were generated from the incomplete fusion weldment. Therefore, it will be useful to use this information to compare with the result of acoustic emission signal emitted from the successful weldment.

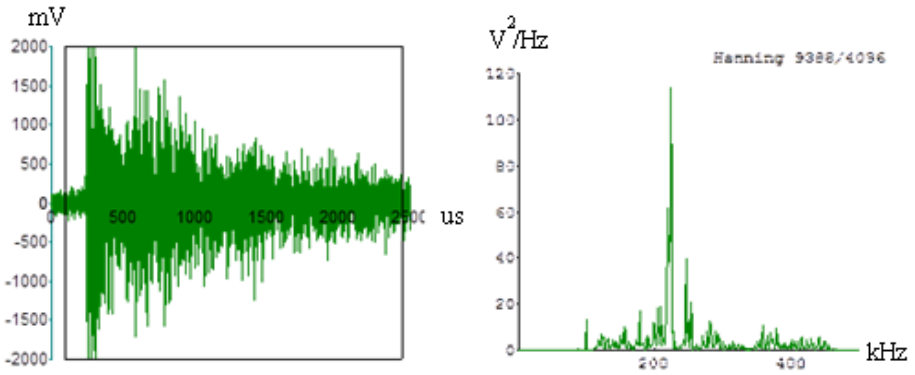

(a) *(b)*

Figure 4.5: Time domain (a) and frequency domain (b) of a random AE signal during cooling phase of Test Weld 1.

4.1.2.2 AE signals detected from welding Al6065 to DX51D sheet

In welding Test Weld 2, jointing Al6065-DX51D using CuSi3 as filler material was conducted with high welding current. The weldment of Test Weld 2 was not also successful. Acoustic emission signal recorded from Test Weld 2 during welding process is illustrated in figure 4.6. In welding phase of Test Weld 2, the detected acoustic emission gain, which is RMS, showed unstable value between 1000 mV and 1400 mV. For cooling phase of Test Weld 2, the time for monitoring the signal was defined to be three minutes after the welding phase was complete. At the beginning period of cooling phase, signal of acoustic emission suddenly dropped from the end of welding phase, and then the detected signal gradually decreased over the time. However, it was very interesting that there were still a lot of acoustic emission signals generated in cooling phase, even though the welding process was completely done.

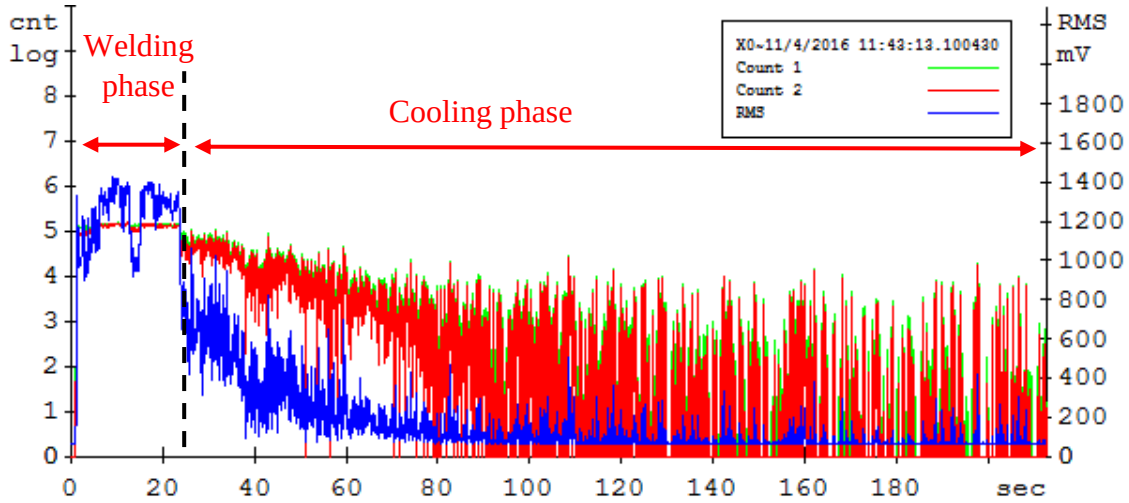

Figure 4.6: Acoustic emission signals emitted from Test Weld 2.

Considering the time domain and frequency domain plots of acoustic emission signals detected from Test Weld 2 in welding phase, figure 4.7a represents a random acoustic emission signal emitted. This detected signal obviously was a continuous signal form that had maximum amplitude of 1800 mV at the detected initial frequency of signal, and a remaining frequency of signal had maximum amplitude averaged of 750 – 950 mV. Figure 4.7b shows the frequency domain from the detected signal in figure 4.7a. This frequency domain plot represents that maximum amplitude of power spectral density of detected signal was equal to 950 Volt^2/Hz at signal frequency of 80 kHz, and there were other tiny value of power spectral density detected at signal frequency of 140 kHz, and 380 kHz.

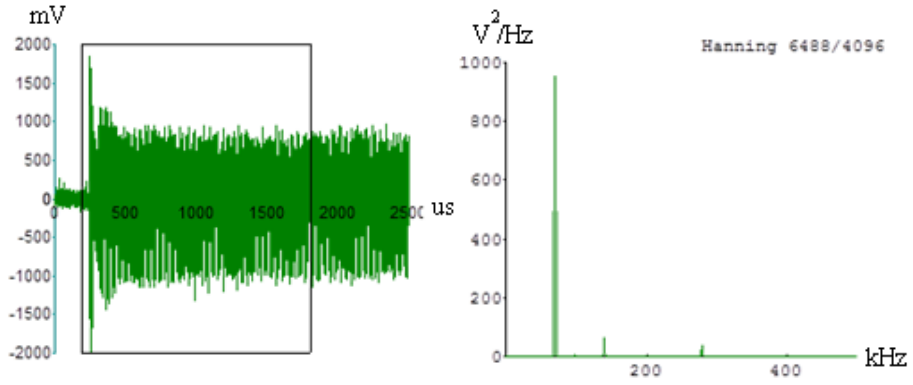

(a) *(b)*

Figure 4.7: Time domain (a) and frequency domain (b) of a random AE signal during welding phase of Test Weld 2.

Figure 4.8a, and figure 4.8b show the time domain and frequency domain plots of a random detected signal of Test Weld 2 in cooling phase. As can be noticed from those figures, the characteristic of the detected signal was a burst signal with high amplitude, and the frequency of the detected signal was ranged from 50 to 500 kHz with the maximum amplitude of spectrum of the detected signal occurring at signal frequency of 220 Volt^2/Hz.

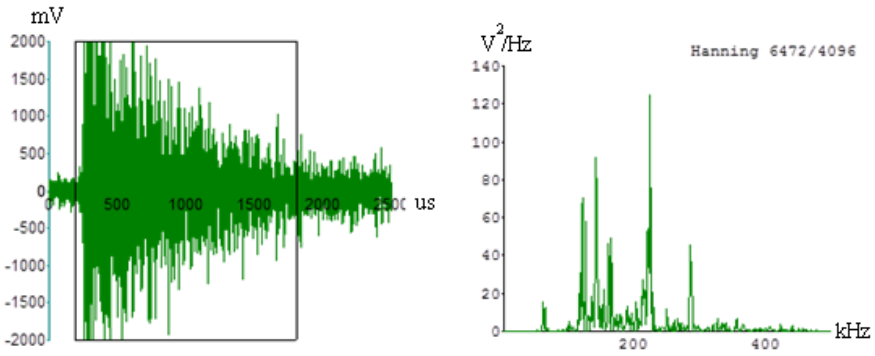

(a) *(b)*

Figure 4.8: Time domain (a) and frequency domain (b) of a random AE signal during cooling phase of Test Weld 2.

4.1.2.3 AE signals detected from welding Al6065 to DX51D sheet

4.1.2.3.1 Welded specimen with first configuration

Test Weld 3 was welding Al6065 to DX510 using AlSi3 as filler material with welding configuration that was welding current of 73 A, and welding velocity of 4.1 m/min. From welding achievement of Test Weld 3, the characteristic of acoustic emission signals detected in this welding process is demonstrated in figure 4.9. From figure 4.9, detected acoustic emission activity was obviously stable signal throughout welding phase. For cooling phase, a number of acoustic emission signals were detected from welded specimen, but the detected signals were not a large amount of signals when comparing with acoustic emission signals detected in cooling phase of both Test Weld 1 and Test Weld 2. Moreover, it was interesting that acoustic emission signal gradually dropped, and could not be detected after two minutes of cooling phase.

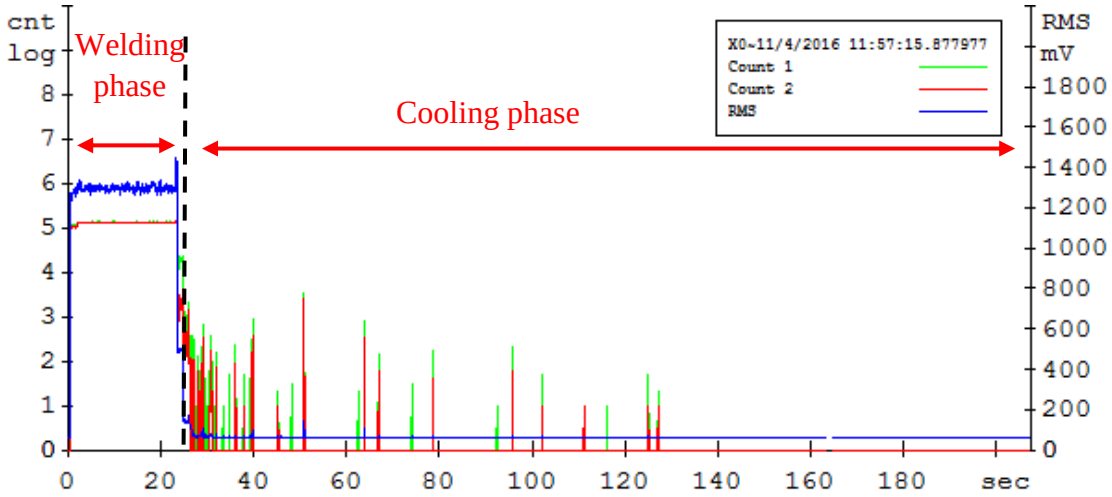

Figure 4.9: Acoustic emission signals emitted from Test Weld 3.

Figure 4.10 shows the detail of detected signals in cooling phase of Test Weld 3. As can be noticed from accumulative event number of the detected signal, Most of the detected signals generated in cooling phase were emitted in initial period of cooling phase. The accumulative event number of detected signal was totally equal to 82 events at the end of recording time which was approximately three minutes after welding phase was complete.

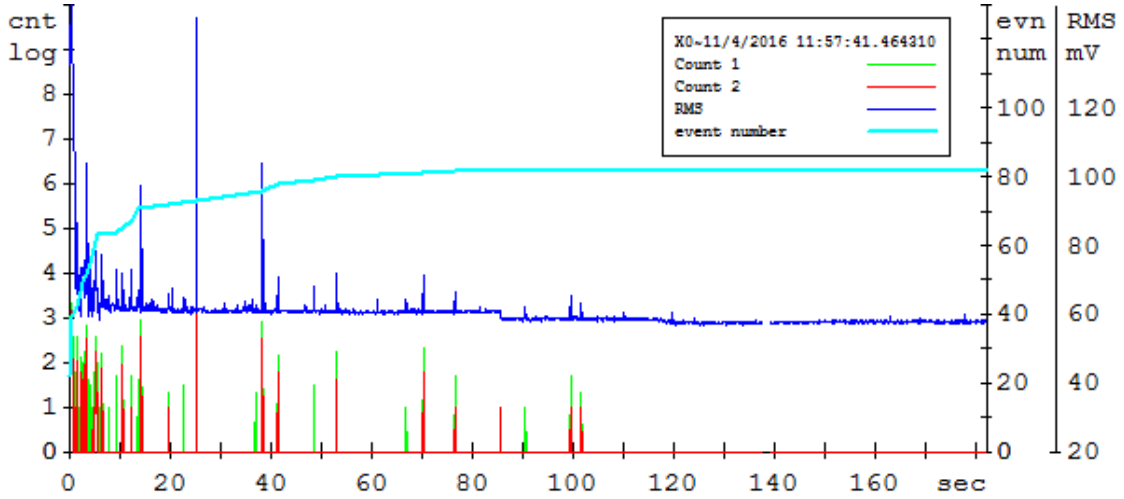

Figure 4.10: Acoustic emission signals emitted from Test Weld 3 in cooling phase.

The time domain and frequency domain plots of a random detected signal from Test Weld 3 during welding phase are shown in figure 4.11. The detected signal in this phase represented the characteristic of continuous signal with high amplitude of signal as illustrated in figure 4.11a. The maximum power spectral density value of a signal was detected at frequency of 140 kHz, and other tiny power spectral density values of signals could be monitored at 80, 290, 420 kHz as demonstrated in figure 4.11b.

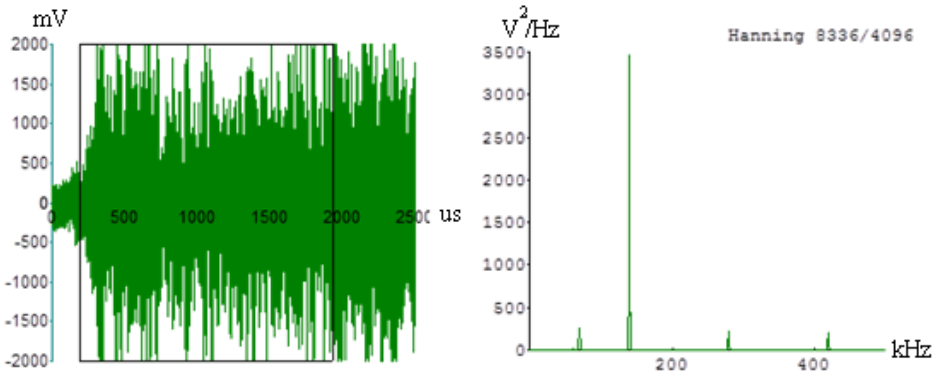

(a) *(b)*

Figure 4.11: Time domain (a) and frequency domain (b) of a random detected signal during welding phase of Test Weld 3.

In cooling phase of Test Weld 3, Most of the detected acoustic emission signals were a burst signal as shown in figure 4.12a. The time domain plot indicated that the maximum amplitude of a detected signal was about 1500 mV, and the maximum power spectral density value of a detected signal was appeared at frequency of 210 kHz with distribution of a detected signal frequency ranged from 100 kHz to 450 kHz as depicted in figure 4.12b.

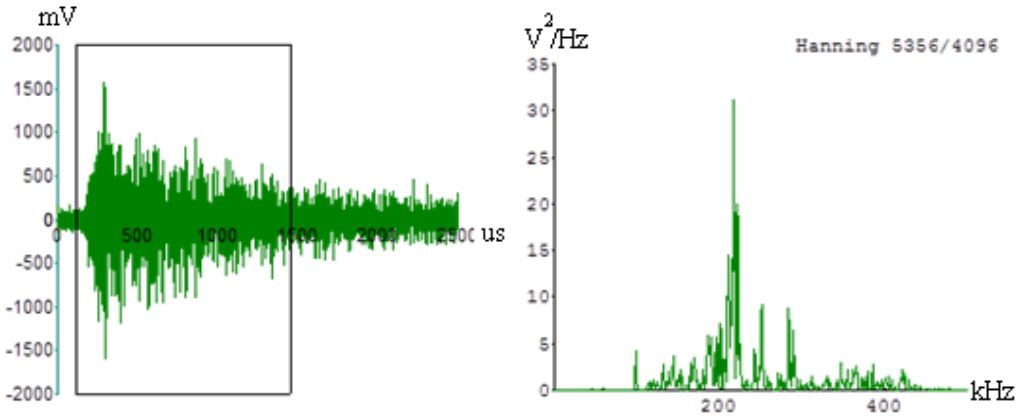

(a) *(b)*

Figure 4.12: Time domain (a) and frequency domain (b) of a random AE signal during cooling phase of Test Weld 3.

4.1.2.3.2 Welded specimen with second configuration

The characteristic of detected signals of Test Weld 4 welding Al6065 to DX51D sheet by using AlSi3 as filler material with different welding configuration from that of Test Weld 3 was demonstrated in figure 4.13. The extremely high acoustic emission signal was generated with a bit unstable signal during welding phase. In cooling phase, there were not many acoustic emission signals generated, and RMS value of acoustic emission gain showed the stable condition.

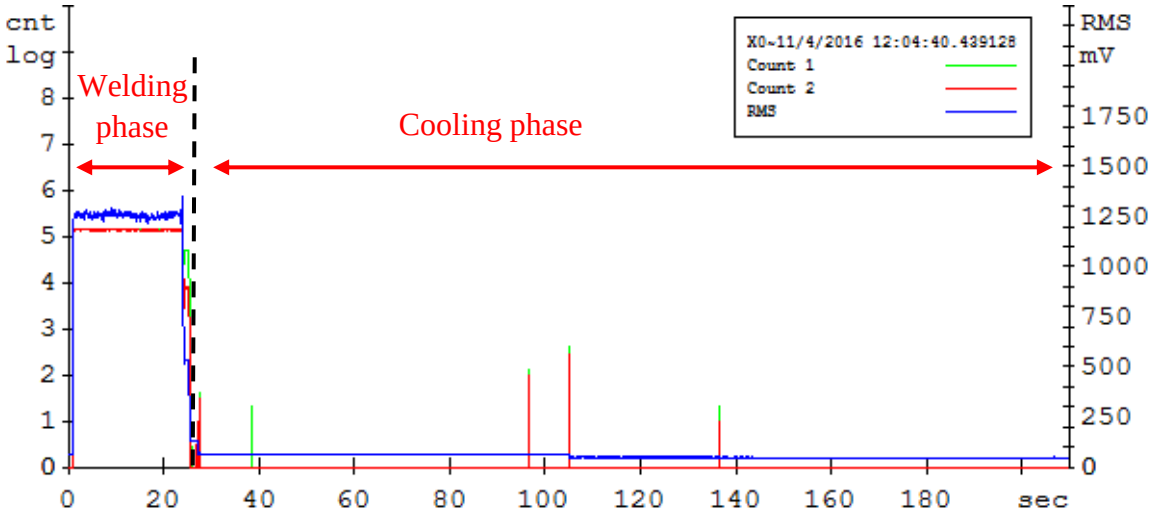

Figure 4.13: Acoustic emission signals emitted from Test Weld 4.

Figure 4.14 shows acoustic emission signal generated during cooling phase of Test Weld 4, most of the detected signals were emitted at the beginning of cooling phase after the welding phase was complete. The accumulative event number of detected signal was totally equal to three events, and the RMS value of detected signal immediately decreased from 60 to 50 mV at 80th second of cooling phase. Afterward, the RMS signal showed stable condition again, and the event number of detected signal was not increased through the end of monitoring process.

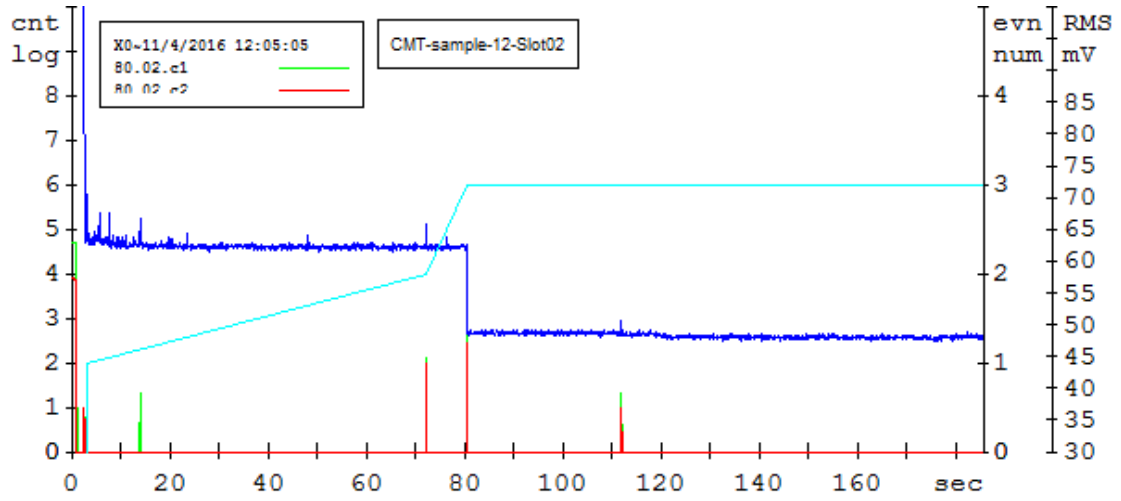

Figure 4.14: Acoustic emission signals emitted from Test Weld 4 in cooling phase.

For time domain and frequency domain plots of Test Weld 4 in welding phase, most of the detected signal were also shown in form of a continuous signal as depicted in figure 4.15a. The maximum amplitude of detected signal was around 1500 mv, and then the amplitude value of signal remained constantly from 1200 mV to 450 mV. Figure 4.15b

represents the frequency domain plot of detected signal. The highest power spectral density value of detected signal was equal to 600 Volt^2/Hz, and detected at signal frequency of 80 kHz. Also, there were other signals detected with low energy at signal frequency of 150 kHz, and 280 kHz.

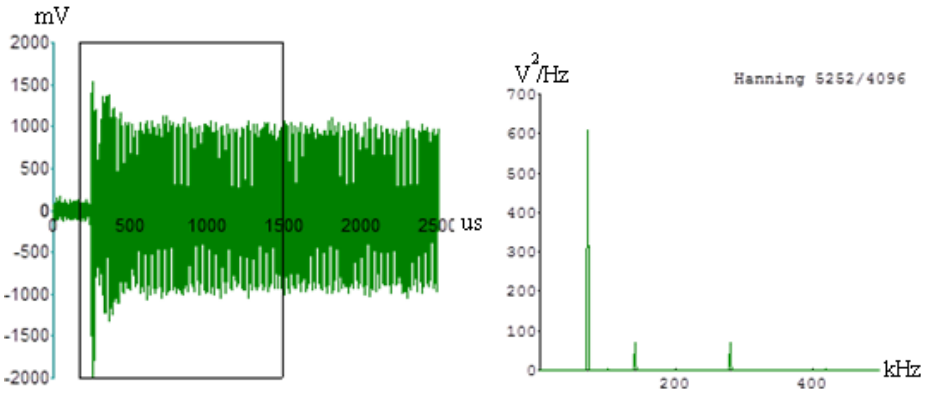

(a) *(b)*

Figure 4.15: Time domain (a) and frequency domain (b) of a random AE signal during welding phase of Test Weld 4.

Figure 4.16 demonstrates the appearance of detected signal emitted from Test Weld 4 in cooling phase. As can be observed in figure 4.16a, the burst signals with low intensity of signal were found in cooling phase. These detected signal having two maximum amplitudes were 1200 mV, and 1500mV. For frequency domain plot of detected signals, the power spectral density value of signal was ranged from 80 mV to 450 mV, and its maximum amplitude was equal to 4.2 Volt^2/Hz at signal frequency of 80 kHz as shown in figure 4.16b.

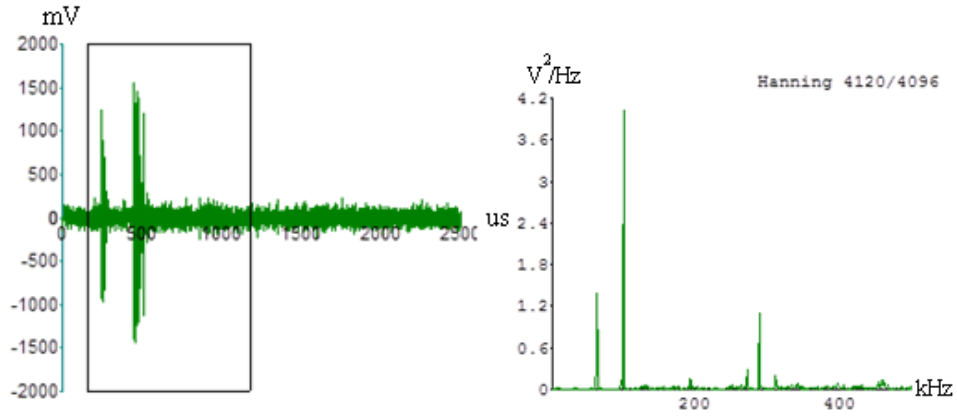

(a) *(b)*

Figure 4.16: Time domain (a) and frequency domain (b) of a random AE signal during cooling phase of Test Weld 4.

Based on the experimental outcomes of measuring acoustic emission signals generated from welded specimens during CMT welding process, they clearly identified that the characteristics of acoustic emission signals generated in CMT welding could be mainly differentiated between acoustic emission signals detected in welding phase and acoustic emission signals detected in cooling phase.

In welding phase, analyzing the time domain plots indicated that the acoustic emission signals detected from all specimens represented the property of a continuous signal with high value of acoustic emission signals. For signal frequency analysis, the frequency domain plots of detected signals in welding phase demonstrated that the maximum amplitudes of power spectral density value of detected signals were mainly found at low signal frequency ranged from 60 to 100 kHz. When considering the major causes of occurring a large number of acoustic emission signals during welding phase of CMT welding, it might occur from several reasons, for instance, deformation of welded material, movement of welding wire, and arc of welding process. Thus, monitor of the quality of CMT weldment during welding phase by using acoustic emission technique might be inappropriate, because there were many unwanted events generating acoustic emission signals during CMT welding process.

For acoustic emission signals detected in cooling phase, the time domain plots of all welded specimens demonstrated that all detected signals showed the signal appearance of a burst signal. However, a great amount of acoustic emission signals could be detected from welded specimen when it was incomplete fusion, whereas a small number of acoustic emission signals were detected when the welded specimen had perfect weldment. For frequency domain plots, they clarified that maximum amplitudes of power spectral density value of unsuccessful welded specimens were mainly generated at signal frequency of 220 kHz, but specimen with successful weldment showed maximum amplitudes of power spectral density values occurring at signal frequency of 100 kHz. Furthermore, to evaluate the quality of weldment, using an acoustic parameter which was accumulative event number of detected signals in cooling phase might be beneficial to interpret the deformation processes of welded specimen after welding process was done.

According to these experimental results, monitoring acoustic emission signals during CMT welding process could be employed to evaluate the quality and deformation of weldment, especially in cooling process. Although, it would be difficult to monitor the wanted-acoustic emission signals in welding phase of CMT welding process.

4.2 Corrosion process of CMT-welded specimens

4.2.1 Selection of test specimens for corrosion testing

After welding process was done, the successful welded workpieces which were Test Weld 3 and Test Weld 4 were chosen to be the test specimens for being placed into the salt spray chamber. The dimension of each specimen in this experiment was prepared to be 80mm x 20mm x 1mm as described in the section of 3.3.2. The number of test specimens was 10 pieces of Test Weld 3, and 10 pieces of Test Weld 4. Therefore, the total number of test specimens in this experiment was 20 pieces. The salt spray chamber according to ISO 9227 was employed to create the corrosive environment on the test samples for 96 hours continuously.

4.2.2 Corrosion appearance of test specimens

After the test specimens were exposed to corrosive environment inside the salt spray chamber for 96 hours, the macro-photos of test specimens of Test Weld 3 and Test Weld 4 are shown in figure 4.17 and figure 4.18, respectively. As can be seen from figure 4.17, corrosive area occurring on the surface of Test Weld 3 mostly appeared on the galvanized steel DX51D sheet, whereas the surface of Al6065 Alloy did not have the corrosive area on its surface. The severe corrosive areas of Test Weld 3 were obviously observed and could be divided into three zones; the edge of DX51D sheet, the weldment area, and the back site of weldment area on DX51D sheet.

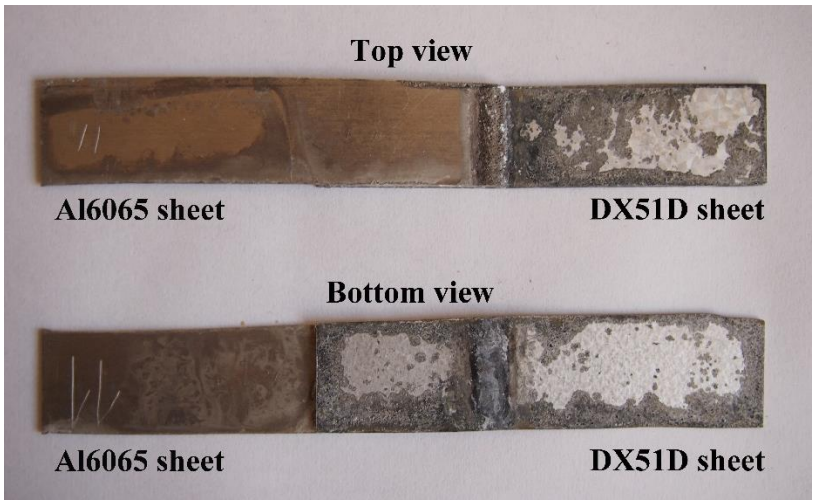

Figure 4.17: A corrosive sample of Test Weld 3 after 96 hours in salt spray chamber.

Figure 4.18 depicts the corrosive specimen of Test Weld 4 after tested in salt spray chamber for 96 hours. The corrosive appearances were mainly found two areas which

were the edge of DX51D sheet and the weld zone of DX51D sheet. However, the weld back site of weldment area on DX51D sheet of Test Weld 4 did not appear the corrosive area which was different from the corrosive specimens of Test Weld 3 that had the corrosive surface on this area. Additional, on the surface of DX51D sheet of Test Weld 4, the large amount of white substance was observed on surface of galvanized steel as shown in figure 4.19. This was probably because the chemical reaction between zinc at surface of test specimen, oxygen and water in the air. From combination of those elements, zinc oxide (ZnO) and zinc hydroxide ($Zn(OH)_2$) could be formed as the white matter on the surface of test specimen and these corrosion products could help decreasing the corrosion rate occurring on the test specimen.

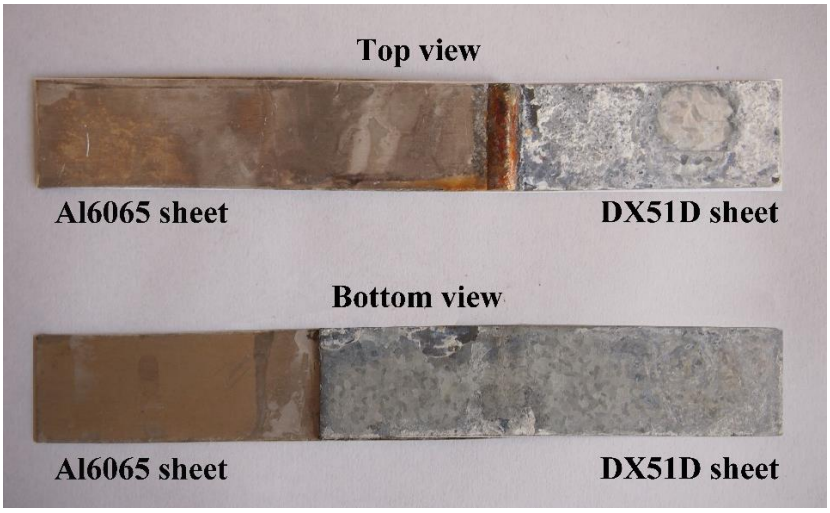

Figure 4.18: A corrosive sample of Test Weld 4 after 96 hours in salt chamber.

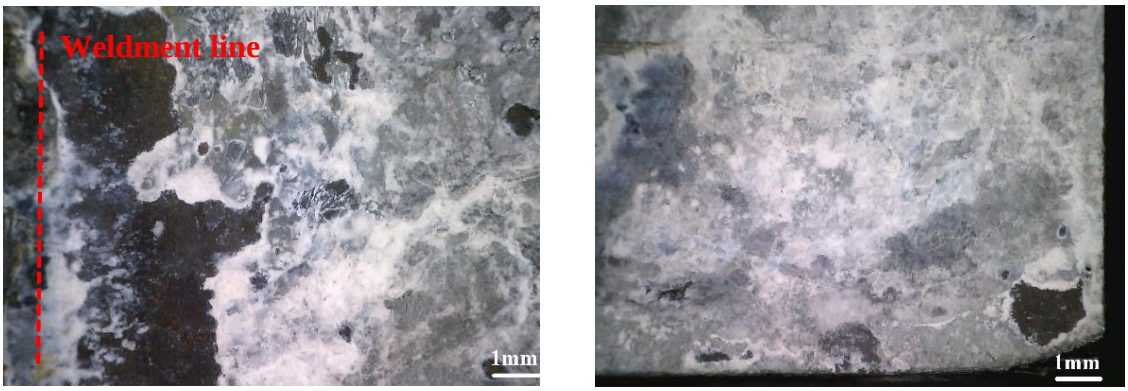

(a) *(b)*

Figure 4.19: Corrosion production established on galvanized steel, (a) at weld zone, (b) at edges of galvanized steel.

According to the experimental results in corrosion testing, it was noticed that the degradation of metallic material largely appeared in galvanized steel sheet (DX51D). This

was probably because Al6065 and DX51D had the different value of electrochemical potential. Technically, jointing two dissimilar metals, the corroded metal which is less electrochemical potential will show anodic condition, whereas the protected metal which has more electrochemical potential will be indicated to be cathodic condition. Therefore, in this experiment, anodic condition was DX51D sheet, and cathodic condition was Al6065 sheet.

When considering the positions of corrosive areas on DX51D sheet, there were three major areas where corrosion progress was mainly observed. These areas were the edge of DX51 sheet, the weld zone of DX51D sheet, and the back site of weld of DX51D sheet. It was obviously shown that corrosion process began at areas in which zinc layer was damaged by cutting and welding process. Cutting process for preparing the test specimen caused the edge of steel directly exposed the corrosive environment because of loss of zinc protection layer and this consequences easily made corrosion process occurring on the edge of DX51D sheet as illustrated in figure 4.20a. Also, the extreme heat of welding process vaporized the zinc coating near the welded area. This vaporization of zinc made the steel surface exposed directly the corrosive environment as shown in figure 4.20b. Due to loss of zinc protection layer on steel surface, it made test specimen easily corroded at welded location. Even though the remaining zinc continued to provide some protection to the zinc-free areas, but it was not enough and the zinc-free areas were continuously corroded when they were still exposed to the corrosive environment. Consequently, the surface of steel without zinc protection layer became corroded by pitting corrosion as illustrated in figure 4.21.

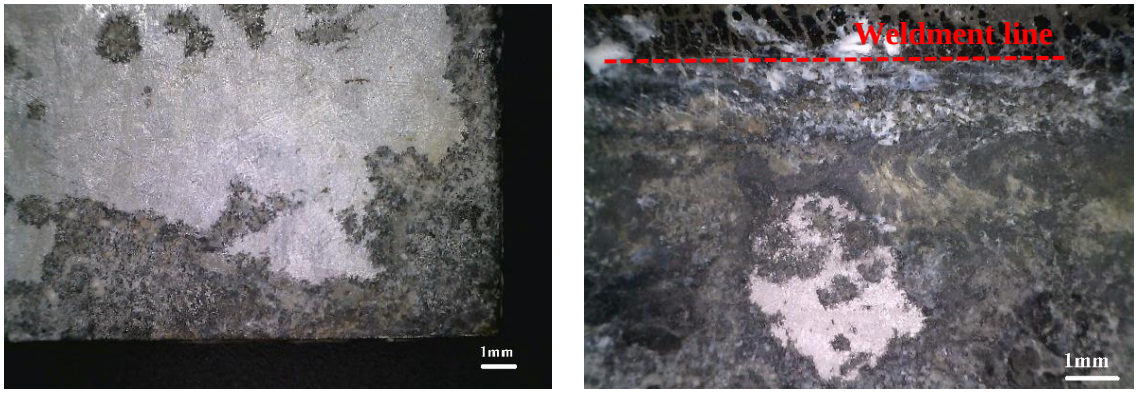

(a) *(b)*

Figure 4.20: Degrading zinc protection layer on galvanized steel, (a) at edges of galvanized steel, (b) at weld zone.

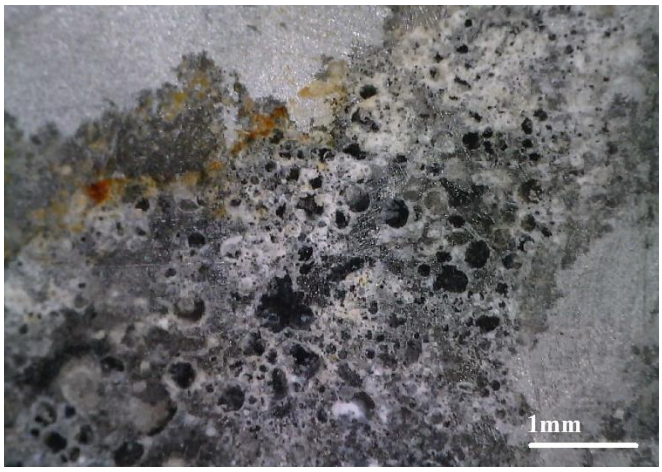

Figure 4.21: Forming pitting corrosion on surface of galvanized steel.

The observation of CMT-welded specimens clarified that setting up the configurations of welding machine highly affected to the appearance of weld and the corrosion resistance on the test specimens. Base on the experimental results of this study, using too high power in welding process generated extreme temperature that could destroyed the protection layer of welded sheet. Consequently, welded sheets easily were corroded by corrosion process, particularly galvanic corrosion in welding dissimilar metals. Therefore, it is necessary to thoroughly consider the welding configurations of welding machine when the specific workpieces need to be welded in order to avoid the low quality of weld as well as the poor corrosion resistance of weld workpieces.

4.2.3 Detection of acoustic emission signals during corrosion process

Before monitoring acoustic emission signals from the test specimens during corrosion process, Pentest was firstly implemented to find the appropriate parameters set up in *DAEMON* software. Table 20 shows the parameters that were configured in software after Pentest was completely done. Based on using these parameters, at beginning time of this experiment, the *DAEMON* software could properly detect and record the acoustic emission signals without capturing unwanted signals, and back ground noises.

Table 20: Acoustic emission parameters configured in the DAEMON software for monitoring corrosion process.

AE configuration input	Value
Gain (amplifier)	40
Data-saving interval	100 ms
Threshold level of count 1	200 ‰.r
Threshold level of count 2	302 ‰.r
Sampling frequency	2 MHz
Threshold level of AE event	251 ‰.r

The experimental results of CMT-welded specimens continuously exposed the corrosive environment inside the salt spray chamber for 96 days could be described as following.

The monitored acoustic emission activities of Test Weld 3 is shown in figure 4.22. In this chart, three relevant acoustic emission parameters were used to describe the acoustic emission phenomena generated from tested specimens being in corrosive environment. These parameters were comprised of root mean square (RMS), count number 1, and count number 2. As can be noticed in figure 4.22, acoustic emission signals could be detected throughout four days of experiment. When considering the RMS signals, it was obviously observed that RMS value of detected signals with its initial setting value of 42 mV was mainly fluctuated between 42 and 53 mV and the detected RMS value suddenly increased at 42^{th} hour of experiment. For count number of the detected signals, the density of count number generated from Test Weld 3 could be divided into two parts; First part was the low density of count number of the detected signals which was observed from beginning time to 42^{th} hour of experiment and second part was the high density of count number of the detected signals which started from 42^{th} hour of experiment to the end of experiment.

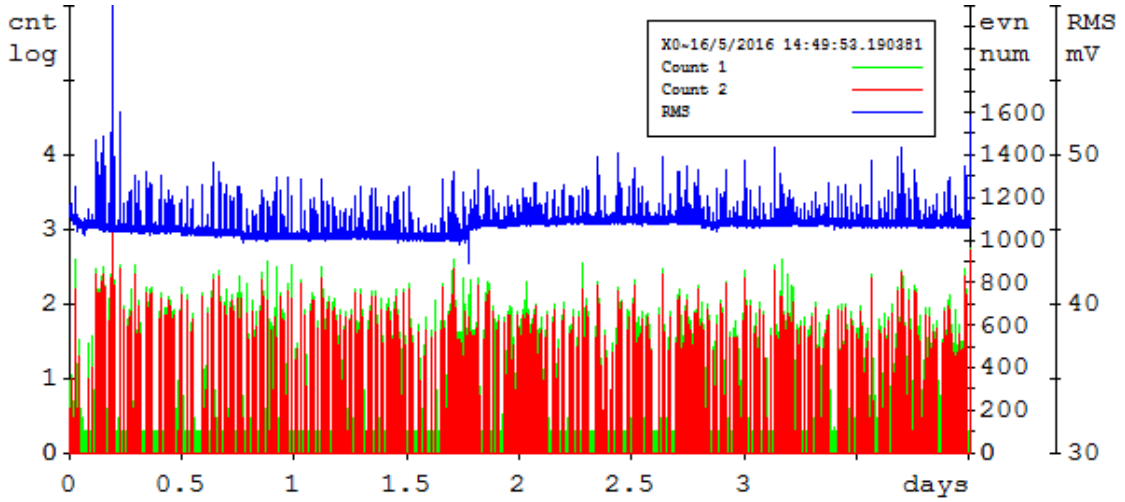

Figure 4.22: Acoustic emission signals detected in Test weld 3 during corrosion testing.

Figure 4.23 illustrates the frequencies of the detected signal of Test Weld 3 as a function of time or power spectral density chart. *MATBAB R2013a* software was used to calculate and create the 3D power spectral density (PSD) chart. The three axes of this chart consist of x-axis showing the frequency value of signal in unit of Hz, y-axis indicating the monitoring period in unit of minute, and z-axis displaying the value of power spectral density of signal in unit of $Volt^2/Hz$. As can be observed in figure 4.23, detected acoustic emission signals could be separated into three zones; the first zone was initial corrosion process from beginning time to 500^{th} minute. In this zone, acoustic emission signals with amplitude of 200 kHz were detected clearly. Then, the second zone was easily noticed in the range of 500^{th} to 2000^{th} minute and there was obviously no acoustic emission signal detected in this zone. Last but not least, the third zone was observed after 2500^{th} minute of experiment. The detected signals in this zone emitted with various frequencies and the amplitude of the detected signals gradually increased over experimental period.

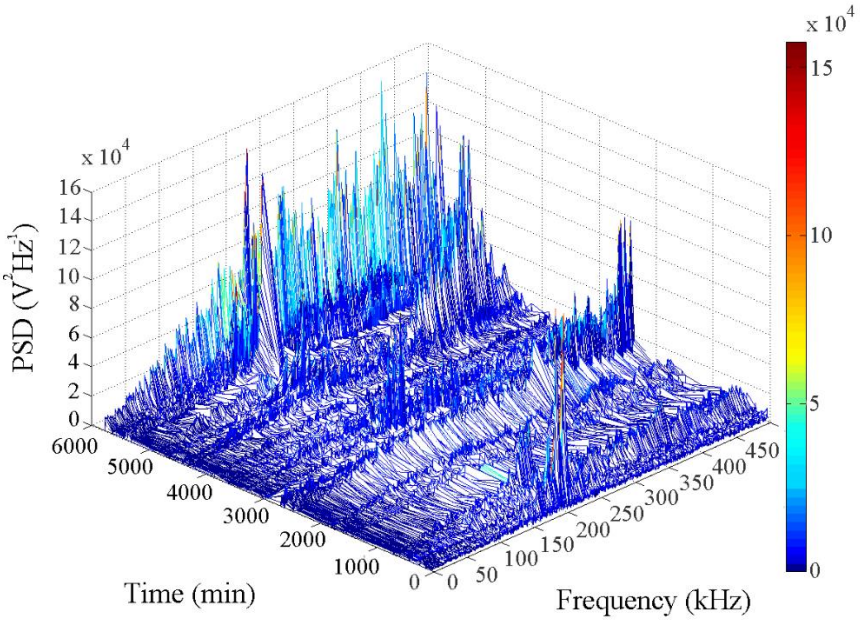

Figure 4.23: PSD of signals detected from Test weld 3 during corrosion testing.

The results of monitoring acoustic emission activities in Test Weld 4 during corrosion process were similar to the outcomes of experiment in Test Weld 3 as mentioned above. Figure 4.24 represents acoustic emission parameters against experimental time of Test Weld 4. In this chart, both RMS signal value and count number of the detected signal gradually increased along with increasing experimental time. The intensity of count number generated in the corrosion process could be described the degradation process on the test specimen. For analyzing the 3D PSD chart of Test Weld 4, its result is shown in figure 4.25. The signal characteristic of Test Weld 4 could be also separated into three zones like the 3D PSD result of Test Weld 3. However, in the third zone of three dimension PSD chart of Test Weld 4, the frequency of signals was only detected in range of 50 kHz to 250 kHz.

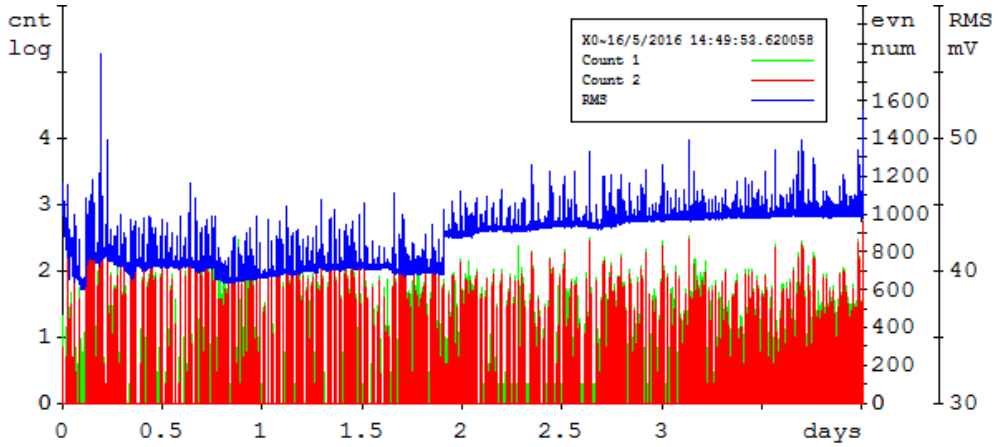

Figure 4.24: Acoustic emission signals detected in Test weld 4 during corrosion testing.

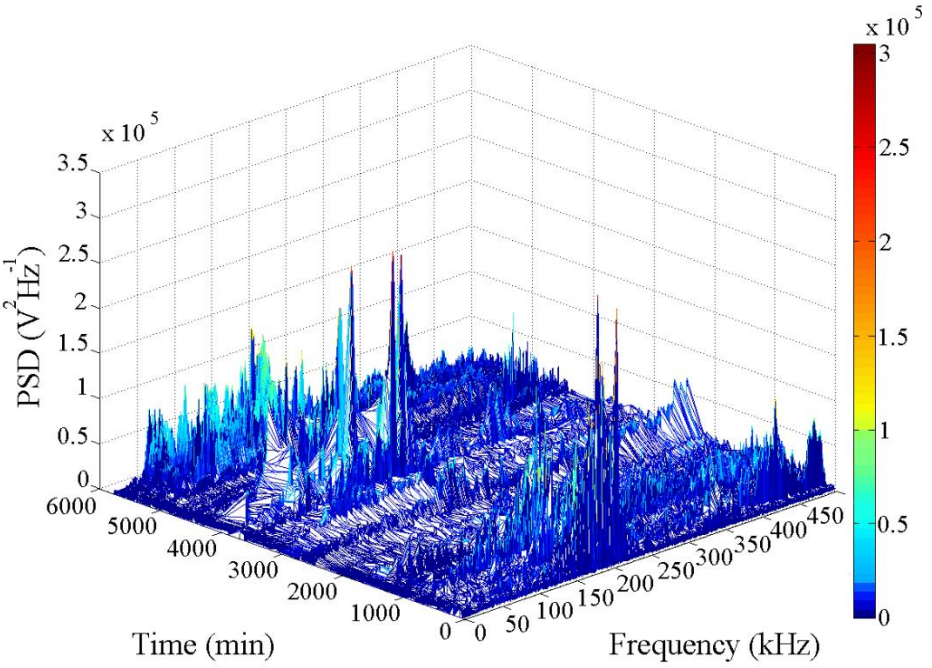

Figure 4.25: PSD of signals detected from Test weld 4 during corrosion testing.

Based on the experimental results of detecting acoustic emission signal during corrosion process on the test specimen, the characteristics of detected signals corresponded to the corrosion process occurring on the test specimen. As can be noticed from acoustic emission results, the detected signals showed the weak signals at the beginning of corrosion process. It was expected that there was oxide layer forming on the surface of galvanized steel sheet due to oxidation reaction of zinc. This oxide layer or protection film prevented the rate of corrosion process happening on the test specimen. Therefore, acoustic emission signals monitored were low in this period. However, when oxide layer was destroyed because the zinc layer was not strong enough to protect the surface of steel. The acoustic emission sensor could detect the great number of signals emitted from the test specimen. This results showed that acoustic emission method might be able to differentiate each process of galvanic corrosion occurring on the workpiece that was welded by using dissimilar materials.

4.3 Tensile testing of CMT-welded specimens

4.3.1 Mechanical property of CMT-welded specimens

To investigate the mechanical property of CMT-welded specimens, Test Weld 4 specimens were chosen to be tested in tensile testing, because they had the best condition of weldment when compared their qualities of weldment with others. The number of test

specimens for being tested in this section was totally 20 pieces of specimens. They consisted of 10 pieces of corrosive specimens of Test Weld 4 and 10 pieces of non-corrosive specimens of Test Weld 4. To implement this experiment properly, each specimen was carefully installed with the tension machine in order to be subjected to the tension force until the test specimens were fractured. Table 21 shows the results of maximum tension force used to break both corrosive and non-corrosive specimens.

Table 21: Breaking forces of both corrosive and non-corrosive specimens.

No. Specimen	**Corrosive specimen (N)**	**Non-corrosive specimen (N)**
1	2001	2250
2	2078	2378
3	2096	2326
4	1979	2249
5	2010	2235
6	1980	2350
7	1995	2258
8	2022	2256
9	2050	2401
10	2036	2342
Average	2024.7	2304

When considering the mean values of both corrosive and non-corrosive specimens, it was found that the mean value of corrosive specimen was equal to 2024.7 N, and that of non-corrosive specimen was equal to 2304. Therefore, the difference of mean value between both corrosive and non-corrosive specimen was equal to 279.8 N. Based on the mean values of this experimental result, it indicated that the breaking force of specimen would be decreased approximately 12.14%, when the specimen got corroded for 96 hours in the salt spray chamber. Figure 4.26 points out comparing the mean values of both types of test specimens.

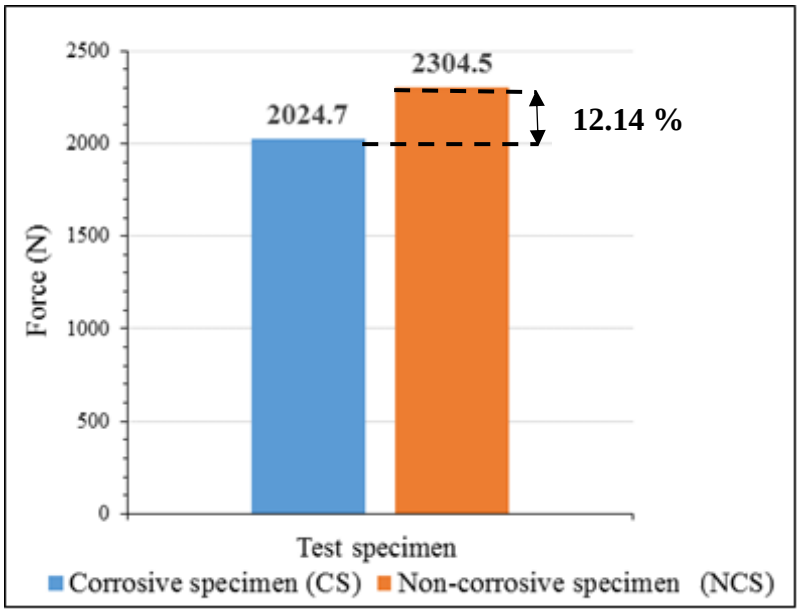

Figure 4.26: Comparing breaking force between corrosive and non-corrosvie specimens.

To evaluate the damges of joint of welded specimens after tensile testing was done, two types of different fracture were found as show in figure 4.27. All corrosive CMT-welded specimens were broken at the interface between the weld metal and galvanized steel DX51D sheet as displayed in figure 4.27a, and all non-corrosive CMT-welded speicmens were fractured at the fusion zone close to the aluminum alloy sheet Al6065 as illustrated in figure 4.27b.

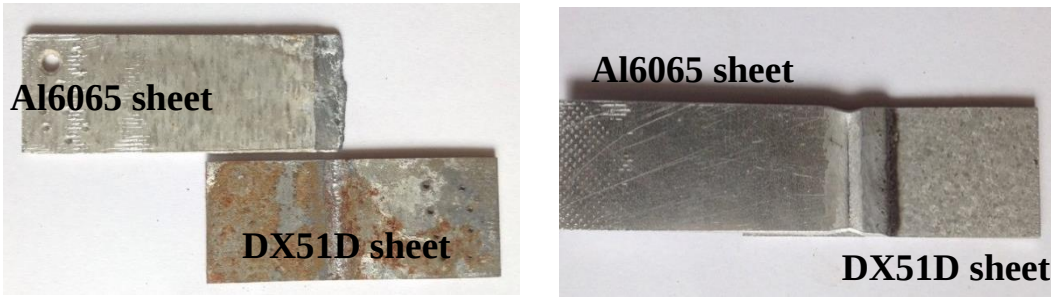

(a) *(b)*

Figure 4.27: Rupturing appearances of (a) corrosive specimen and (b) non-corrosive, specimen after being tested.

Based on the tensile testing of CMT-welded specimens of Test Weld 4, the experimental results clarified that corrosion process occurred on the test specimens directly affected to both strength of the welded specimens and failure appearance of the welded specimens. Therefore, applying suitable corrosion protections to the welded

specimen is highly important in order to extend the lifespan of a welded specimen, or a structure, resulting in saving the cost of maintaining process.

4.3.2 Monitor of acoustic emission signals during tensile testing

To set up the configuration of *DAEMON* software for detecting acoustic emission signals emitted during tensile testing properly, Pentest was conducted to generate a burst signal on a test specimen. A burst signal was used to determine the configuration parameters used in the software. Table 22 lists the suitable parameters configured in *DAEMON* software for recording the signals emitted from a test specimen during tensile testing.

Table 22: Acoustic emission parameters configured in the DAEMON software for detecting signals during tensile testing.

AE configuration input	Value
Gain (amplifier)	40
Data-saving interval	10 ms
Threshold level of count 1	100 ‰.r
Threshold level of count 2	302 ‰.r
Sampling frequency	4 MHz

In this experiment, ten pieces of corrosive specimen and another ten pieces of non-corrosive specimen were individually tested in tensile testing by using the ZDM5/51 universal testing machine. Meanwhile, acoustic emission device was also used to record the acoustic emission signals generated from the test specimen during tensile testing. To detect the signal from specimen properly, acoustic emission sensor was fixed on the test specimen by plastic gripper.

To estimate the results in this experiment, root mean square (RMS), displacement, and force values were considered to be the variables that showed the relation between acoustic emission signal and mechanical properties. After testing all specimens was done, the experimental results can be displayed in figures 4.28, and 4.29. As can be seen in figure 4.28, this chart showed the typical relation between RMS, displacement, and forces values against experimental period of corrosive specimens. From this chart, displacement and force values of corrosive specimen were constantly increased along with time, but it was difficult to detect acoustic emission signals at the beginning of tension stage.

However, the large number of acoustic emission signals could be monitored at point before a corrosive specimen was destroyed and a peak value of acoustic emission signal was found at the same time when a corrosive specimen was broken by breaking force. Thus, these detected signals could be interpreted that there were the great number of acoustic emission signals emitted when the internal structure of corrosive CMT-welded specimen was changed by deformation processes.

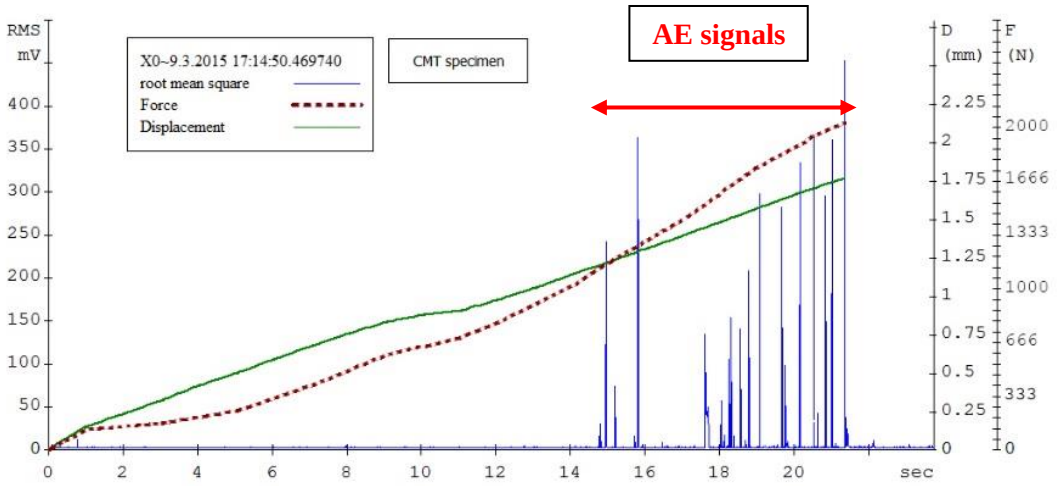

Figure 4.28: AE parameter (RMS), displacement, and force versus time of a corrosive specimen loaded by tension force.

For tensile testing results of non-corrosive specimens, the relation between acoustic emission signal and mechanical properties of all non-corrosive specimens is identically shown in figure 4.29. As can be observed in this chart, the fracture point of a non-corrosive specimen did not occur at the maximum tension force, but the test specimen was fractured by breaking force that had force value lower than the maximum tension force recorded. Moreover, acoustic emission signals detected could be divided into three parts; first part was the initial stage in which the detected signals were emitted with low amplitude of signals, second part was the middle stage where the detected signal had much higher amplitude than the detected signals of initial stage, and this signal was detected at same time of maximum tension force occurring on test specimen, and third part was the last stage that showed the peak value of RMS at fracture point of test specimen.

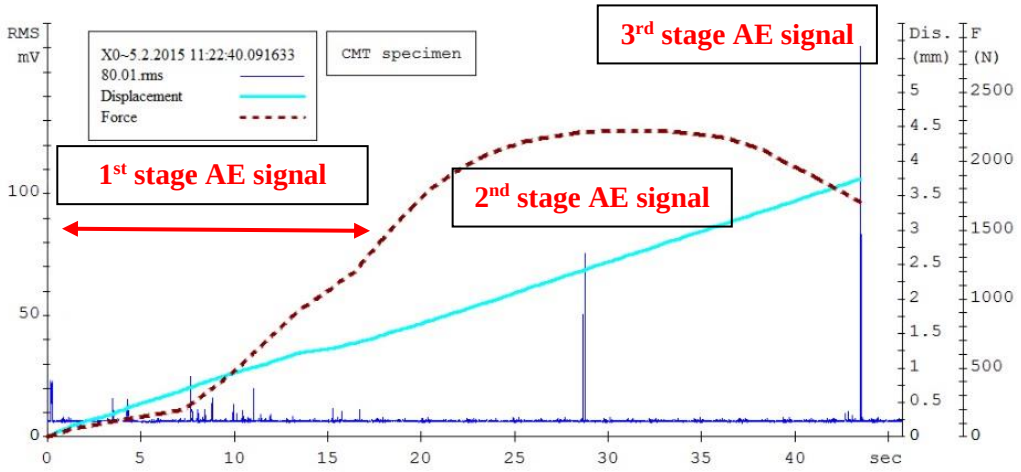

Figure 4.29: AE parameter (RMS), displacement, and force versus time of a non-corrosive specimen loaded by tension force.

Figure 4.30 represents the common type of the detected signals from all test specimens during tensile testing. From the time domain chart as displayed in figure 4.30a, the characteristic of monitored signal was a burst signal with frequency of signal between 100 and 220 Hz as depicted in figure 4.30b. It was supposed that this detected signal might be released in material during deformation process due to tension force.

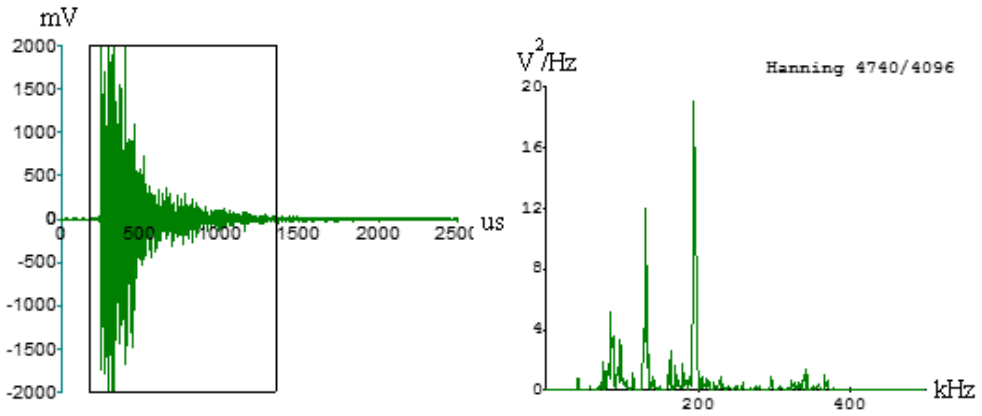

(a) *(b)*

Figure 4.30: Time domain (a) and frequency domain (b) of typical acoustic emission emitted during tension testing.

From the experimental results mentioned above, monitoring acoustic emission signals during tensile testing demonstrated that there were the high amplitudes of the detected signal emitted from both corrosive and non-corrosive specimens before they were ruptured by maximum breaking forces. Thus, these detected signals were useful to be warning signal, or alarming signal prior to the failure occurring on the material.

4.4 High cycle fatigue testing

4.4.1 Appearance of test specimens after corrosion process

To study the fatigue life in several conditions of fatigue specimen, thus, in this experiment, there were three different types of fatigue specimens prepared as depicted in figure 4.31a showing free corrosion specimens, figure 4.31b representing two day-corroded specimens, and figure 4.31c displaying four day-corroded specimens. It is worth noting that there was obviously the corrosion product formed on the surface of four day-corroded specimens much more than that of two day-corroded specimens, although their experimental duration of corrosion process was different only two days, and this could be explained that the magnesium alloy was highly susceptible to be corroded in corrosive environment. To more understand the fatigue strength of magnesium alloy, all prepared specimens were tested by using the resonant fatigue testing machine for finding the fatigue limits of test specimens and then comparing the fatigue limits between non-corrosive specimen and corrosive specimen was discussed.

(a) *(b)* *(c)*

Figure 4.31: Three types of fatigue specimen, (a) free corrosion specimens, (b),(c) corrosive specimens after two and four days in corrosion process, respectively.

4.4.2 Evaluation of test specimen fatigue limits

The test results of high-cycle bending fatigue testing of magnesium specimens are reported in figure 4.32 as S-N curve. The bending stresses applied to specimens were 60, 80, 90, 119, 139, and 156 MPa at the stress ration R=-1. As S-N curve, it was observed that most of the non-corrosive specimens had fatigue strength value higher than other types of specimen at same bending stress levels. On the other hand, in same bending stress levels, four day-corroded specimen had the fatigue strength value less than the fatigue strength of both two day-corroded specimen and non-corrosive specimen. When

considering the fatigue limit of test specimens, it was found that the fatigue limits of non-corrosive specimen, two day-corroded specimen, and four day-corroded specimen were 80, 80, and 60 MPa, respectively.

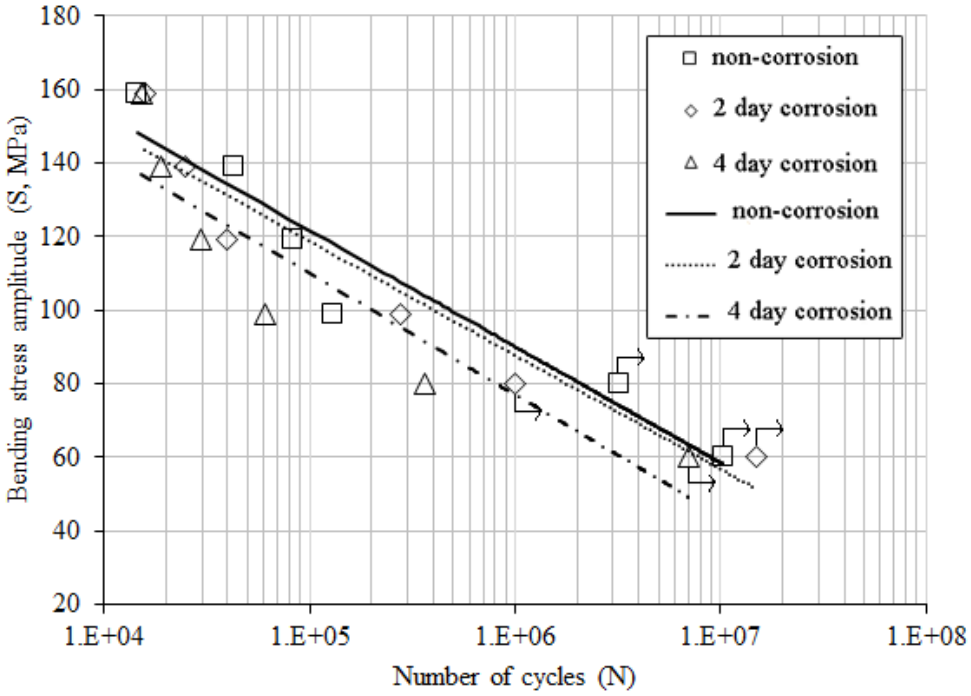

Figure 4.32: S-N curve of Mg alloy (AZ31B) specimens from bending fatigue testing.

Based on the experimental results, the reduction of fatigue limit in magnesium alloy could be found that when the magnesium alloy was under corrosive condition. This might be because surface roughness of test specimen was increased due to corrosion process occurring on the surface of test specimen. By increasing the rough surfaces on the test specimen, this could create stress concentration that facilitated the fatigue crack formation on the test specimen and then the fatigue strength of specimen was greatly reduced. Technically, the smoother the surface finish on the metal specimen, the higher the fatigue strength.

4.4.3 Monitor of acoustic emission signals during fatigue testing

Table 23 lists the essential parameters configured in *DAESHOW* software in order to record the acoustic emission signals properly during fatigue testing. Pentest was firstly conducted to determine these parameters.

Table 23: Relevant parameters used in the DAESHOW software.

AE configuration input	Value
Gain (amplifier)	25
Data-saving interval	1000 ms
Threshold level of count 1	102 ‰.r
Threshold level of count 2	302 ‰.r
Sampling frequency	2 MHz
Threshold level of AE event	102 ‰.r

The experimental results of monitoring acoustic emission signals from three different types of test specimens loaded under cyclic bending stresses of 60, 80, 99, 119, 139, and 159 MPa were found that the characteristics of detected signals from fatigue testing could be separated into two groups; first group was the detected signals that were generated from the test specimens being under cyclic load more than or equal to 139 MPa, and second group was the detected signals that were emitted from the test specimens being under cyclic load less than 139 MPa.

Considering the signals emitted from test specimens being under loads more than or equal to 139 MPa, the similar characteristics of detected signals can be represented in figure 4.33, 4.34, and 4.35 for non-corrosive specimen, two day-corroded specimen, and four day-corroded specimen, respectively. As can be noticed from these figures, it was obviously observed that non-corrosive specimen could tolerate the applied cyclic stress longer time than two day-corroded specimen, and four day-corroded specimen, and two day-corroded specimen could resist the applied cyclic bending stress longer time that four day-corroded specimen.

For appearance of the detected signals, it could be divided into three periods as demonstrated in figure 4.33, 4.34, and 4.35; first period represented that there were a lot of acoustic emission signals generated from test specimen and loading frequency value of test specimen was a bit constant, second period showed that the great reduction of detected signals was clearly observed, but loading frequency value of test specimen was still constant, third period indicated that there were a large number of acoustic emission signals emitted from test specimen, and the loading frequency value of test specimen was dramatically decreased before the test specimen reached its fracture point.

From such acoustic emission results, it was worth noting that detected acoustic emission signals corresponded to the deformation of metal structure subjected to cyclic

loading because acoustic emission signals detected in the first period showed condition of crack initiation happening in test specimen. Theoretically, crack initiation occurs because plastic deformation is not a completely reversible process and this process creates slipband extrusions and slipband intrusions on the surface of the test specimen. Thus, it was expected that emitting the large number of acoustic emission signals in first period caused from the slipband phenomena due to the plastic deformation process. For monitoring signals in second period, the detected signals were obviously much weaker than that in the first period because the surface irregularities along the slipband caused the formation of cracks close to the surface that propagated into the specimen. In theory, this period was called the fatigue crack growth, and the rate of the crack growth was very low and this was the reason why there were the weak detected signals in the second period. Lastly, detecting the great amount of acoustic emission signals was found in third period because crack propagation at a relatively rapid rate was occurred, and fatigue striations were created as the crack advances across the cross section of the test specimen. Moreover, the loading frequency in third period was suddenly decreased, and this could be interpreted that the fatigue strength of test specimen almost reached the ultimate failure of test specimen.

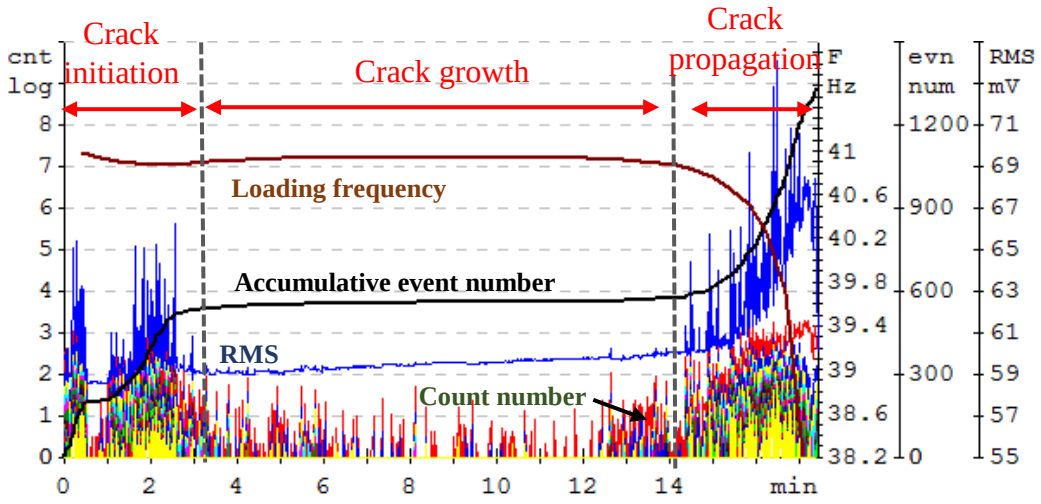

Figure 4.33: AE signals and loading frequency detected from non-corrosive specimen at cyclic bending stress of 139 MPa.

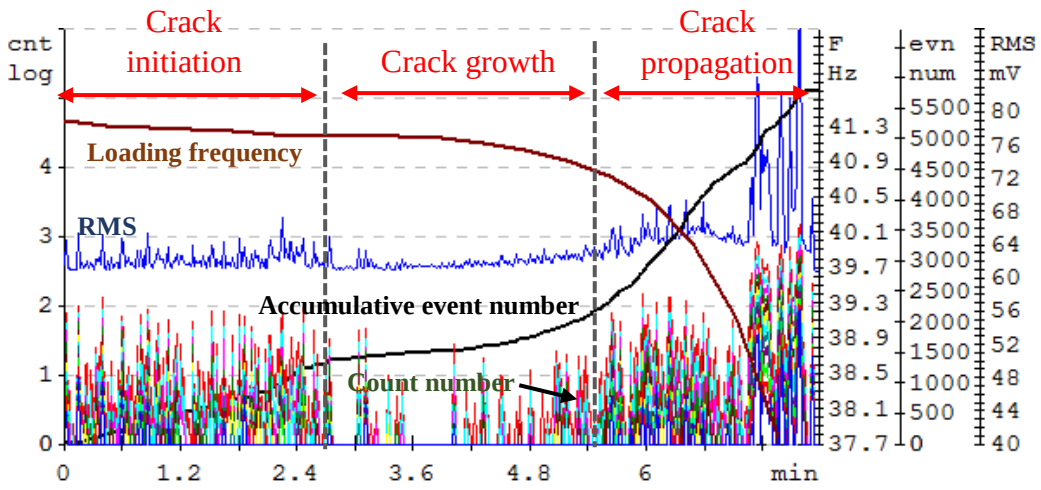

Figure 4.34: AE signals and loading frequency detected from two day-corroded specimen at cyclic bending stress of 139 MPa.

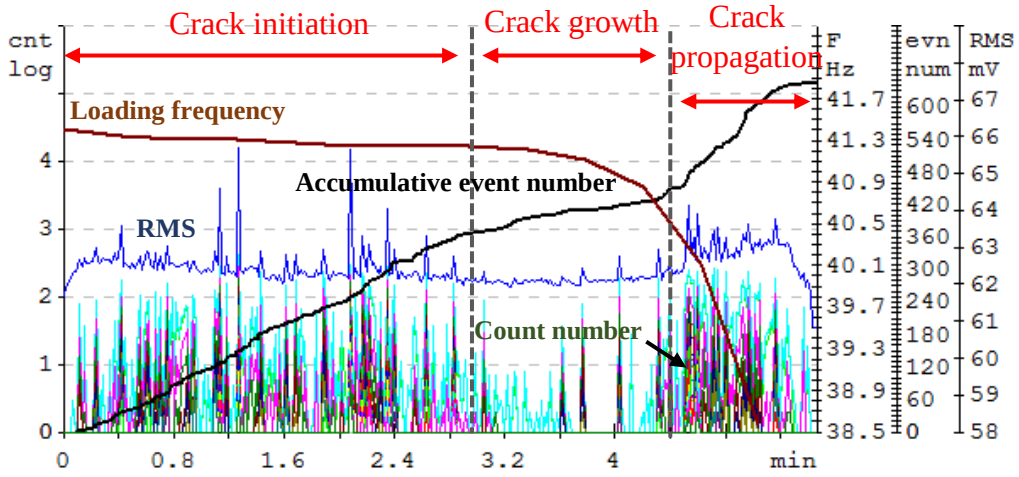

Figure 4.35: AE signals and loading frequency detected from four day-corroded specimen at cyclic bending stress of 139 MPa.

For experimental results of the detected signals generated from the test specimen being under cyclic load less than 139 MPa, the typical characteristics of acoustic emission signals and loading frequency measured from test specimen are similarly shown in figures 4.36, 4.37, and 4.38 for non-corrosive specimen, two day-corroded specimen, and four day-corroded specimen, respectively. As can be seen in these charts, the non-corrosive specimen showed the longest duration for resisting the applied fatigue load before getting its fatigue failure. On the other hand, the four day-corroded specimen demonstrated the shortest duration for opposing the applied fatigue load, and this results could be explained that the corrosion process greatly affected to fatigue strength of the test specimen.

When comparing the acoustic emission signals emitted from both test specimen being under cyclic stress more than 139 MPa and test specimen being under cyclic stress

less than 139 MPa, both acoustic emission results had different characteristics of detected signals. Nevertheless, the acoustic emission signals and loading frequency monitored from test specimens being under cyclic load lower than 139 MPa could be also divided into three periods. In first period, there were not many acoustic emission signals detected from test specimen and loading frequency value measured from test specimen was slightly increased, and then the loading frequency value was gradually decreased with continuously increasing the detected signals in the second period as illustrated in figure 4.36. For third period, in this period, there were a great number of acoustic emission signals generated, whereas the loading frequency value was immediately decreased before the test specimen broke due to fatigue failure.

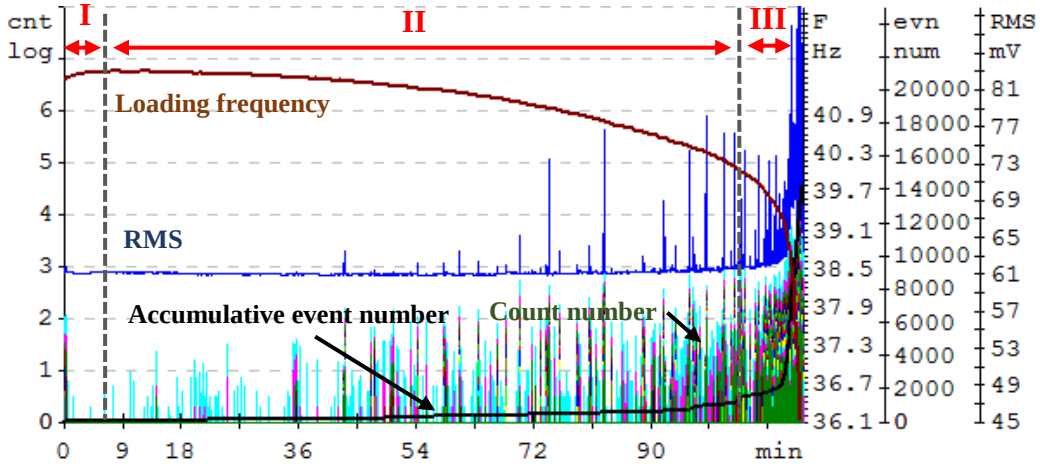

Figure 4.36: AE signals and loading frequency detected from non-corrosive specimen at cyclic bending stress of 99 MPa.

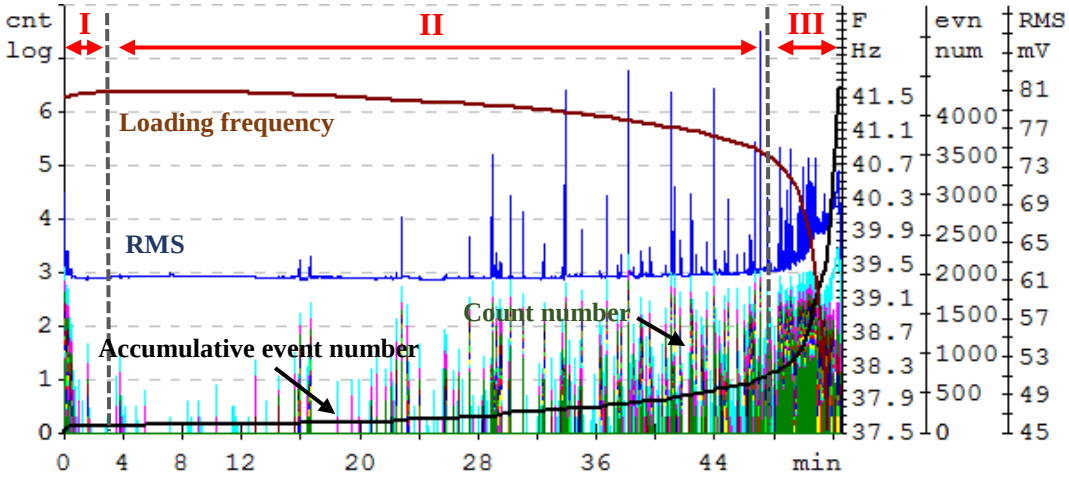

Figure 4.37: AE signals and loading frequency detected from two day-corroded specimen at cyclic bending stress of 99 MPa.

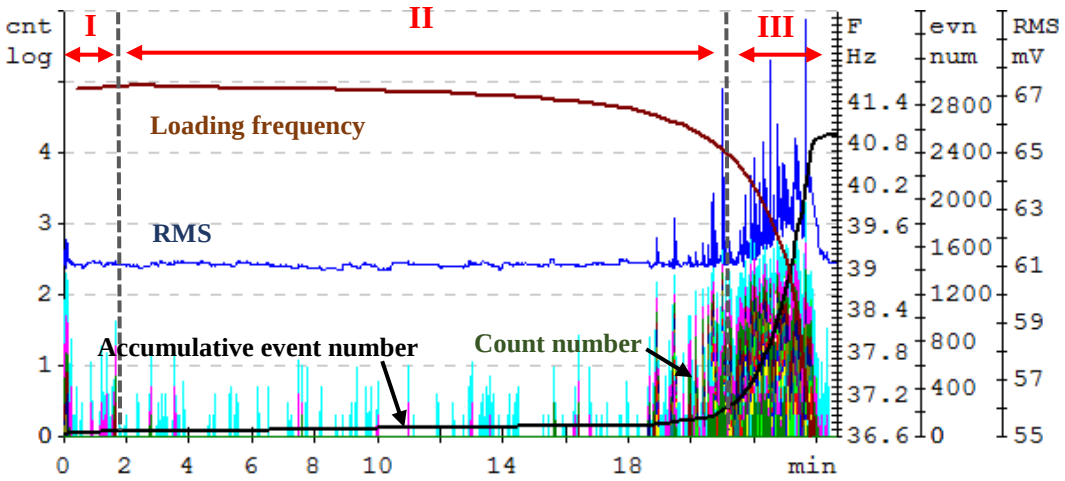

Figure 4.38: AE signals and loading frequency detected from four day-corroded specimen at cyclic bending stress of 99 MPa.

According to the results mentioned above, at the low applied cyclic bending stress, less than 139 MPa, it could be described that the loading frequency of test specimen was a bit increased at the beginning of experiment, this was probably because a large quantity of microstructural barriers such as a grain boundary, inclusions, was formed in materials by low cyclic load, and this could increase the fatigue strength of material and also was capable of preventing the crack initial growth occurring on structure of material, resulting in detecting the acoustic emission signals that was very weak in this period. For the detected signals in second period, it was expected that the crack initiation and crack growth were occurred in this period because acoustic emission system could detected the signals that gradually increased throughout the time until the end of second, and all these detected signals were supposed to be generated from short cracks that basically occurred in crack initiation and crack growth conditions. Lastly, the third period was expected that detected signals were generated from the crack propagation stage like the signals detected in the crack propagation of test specimens being under the cyclic stresses more than or equal to 139 MPa.

The initial cracks on surface of a four day-corroded specimen due to fatigue testing is depicted in figure 4.39. The formation and growth of these cracks were obviously seen around the notched part of test specimen in which the maximum and minimum bending stresses applied. Consequently, these initial cracks strongly induced the crack propagation occurring on the test specimen. Figure 4.40 shows the fatigue fracture surface of a four day-corroded specimen after reached its final fracture toughness. As can be noticed from the section surface in figure 4.40, the specimen surface could be divided into two distinct regions; (1) top and bottom regions, these regions showed the

rubbing action between the open surface region as crack initiation and crack propagation processes grew across the section and (2) middle region, this region represented a rough surface area formed by the fast fracture when the load became too high for the remaining cross section. Technically, the exact area of fraction of each region depends on the applied load level. High applied loads result in a small crack propagation area. On the other hand, when lower loads are applied, the crack will have to grow for longer before the test material reaches its fatigue failure, resulting in a smaller area of fast fracture [89].

Figure 4.39: Initial cracks found on surface of specimen at notched area.

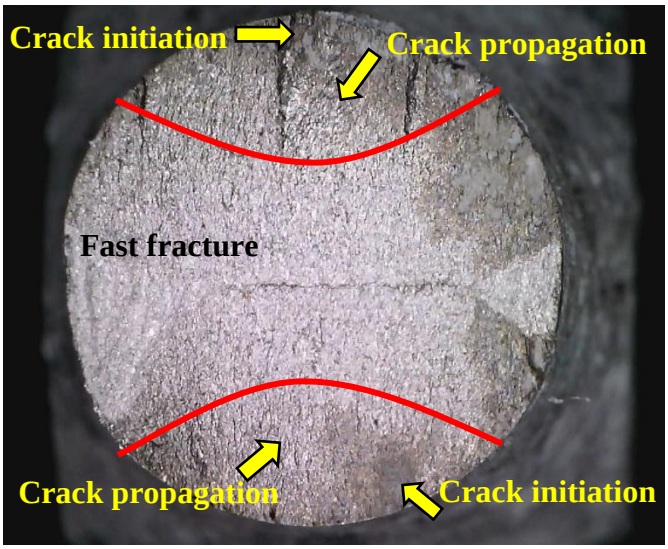

Figure 4.40: Fatigue fracture surface.

Based on the experiment results of monitoring acoustic emission signals during high cycle fatigue testing in magnesium alloy, the characteristics of the detected signals interestingly corresponded with the deformation processes of test materials due to fatigue load. Moreover, using the acoustic emission system was capable of revealing the different

fatigue behaviors occurring on the test specimens which were loaded in different cyclic bending stresses. Therefore, from this experiment, there is highly potential to use the acoustic emission device for monitoring the degradation of material that is subjected to high cycle fatigue load.

CHAPTER 5: CONCLUSIONS

Study of utilizing acoustic emission method to monitor the CMT welding process, corrosion process, and mechanical testing processes in the metal materials is conducted in the present dissertation. The studied results can be summarized as following items;

1. In CMT welding process, the studied results shows that setting up welding configurations and selecting the filler materials which are appropriate to base materials prior to starting welding are great significant to the weld appearance on welded specimen, particularly when welding the dissimilar metals. Therefore, to avoid the damage of welded material during welding process, consideration of welding configuration and filler material must be implemented thoughtfully. For monitor of acoustic emission signals during CMT welding process, the characteristic of the detected signals can be separated into two parts; 1) the signals detected in welding phase, 2) the signals detected in cooling phase. It is found that the detected signals emitted from the cooling phase is more likely to be used for evaluating the weld quality of the welded specimens.

2. Corrosion process occurring on the CMT-welded specimen can be monitored by means of acoustic emission technique because the characteristic of signals detected from the specimen being under corrosive environment corresponds to the corrosion process appearing in the specimen. However, monitoring the acoustic emission signals in corrosion process must be carefully aware of protecting the AE sensor from corrosive environment in order to make the sensor functioning properly.

3. Mechanical deformation of CMT-welded specimen due to tensile testing can be detected by using acoustic emission method. The experimental result indicates that a great number of the signals are released from both the corrosive specimen and the non-corrosive specimen before both types of specimen reach their breaking point. However, the characteristic of the signals generated in the whole process of both types of specimen is different. Therefore, the corrosion process directly affects to acoustic emission property of CMT-welded specimen during mechanical testing.

4. Test of high cycle fatigue on magnesium alloy with different corrosive conditions clarifies that the degradation process occurring on magnesium alloy obviously causes the reduction of its fatigue life. For monitoring AE during high cycle fatigue, AE system is capable of disclosing the fatigue behaviors of magnesium alloy loaded under different cyclic bending stresses and also the detected signals can be interpreted to explain the microstructural deformations of magnesium alloy due to fatigue testing.

REFERENCES

[1] AIRCRAFT CORROSION WIKI [Accessed: 2016, March 14]. Available at: < http://aircraft-corrosion.wikia.com/wiki/Aircraft_Corrosion_Wiki>

[2] ALCOTEC [Accessed: 2016, March 22]. Available at: < http://www.alcotec.com/us/en/education/knowledge/techknowledge/understanding-the-alloys-of-aluminum.cfm>

[3] AMERICAN FOUNDRY SOCIETY [Accessed: 2016, March 30]. Available at: <http://www.afsinc.org/technical/IJM.cfm?navItemNumber=533>

[4] AMERICAN WELDING SOCIETY (AWS) [Accessed: 2016, May 9]. Available at: <https://app.aws.org/itrends/2007/04/it200704/it0407-15.pdf>

[5] APP [Accessed: 2016, March 11]. Available at: < http://blog.appinc.co/corrosion-part-1-what-is-it>

[6] AREF B.: Investigation of using fiber laser and CMT technology in welding of Docol pipes. Master thesis presented at School of Industrial and Information Engineering, Polytechnic University of Milan. Italy. 2014 [Accessed: 2016, March 10].

[7] ASM INTERNATIONAL [Accessed: 2016, March 30]. Available at: <http://www.asminternational.org/documents/10192/3477458/05114G_Chapter_1.pdf/014d105b-5a2a-42a7-918e-a32b31ff6390>

[8] ASM INTERNATIONAL [Accessed: 2016, April 21]. Available at: <http://www.asminternational.org/>

[9] AZO MATERIALS [Accessed: 2016, May 31]. Available at: <http://www.azom.com/article.aspx?ArticleID=6707>

[10] BARBARA, A.: Corrosion resistance of magnesium alloys. ASM International. [Accessed: 2016, April 8]. Available at: <http://www.asminternational.org/documents/10192/1849770/06494G_Chapter_Sample.pdf>

[11] BEYTULLAH, G., ERDINC, K., EMEL, T., AYDIN, S.: Mechanical and microstructural properties of robotic Cold Metal Transfer (CMT) welded 5083-H-111 and 6082-T651 aluminum alloys. Materials and Design, 54(2014): 207-211.

[12] CAMPBELL, F.C.: Elements of metallurgy and engineering alloys. ASM International, 2008. ISBN 978-0-87170-867-0.

[13] CAO, R., CHEN, H.J.H., WANG, P.: Cold metal transfer spot plug welding of AA6061-T6-to-galvanized steel for automotive applications. Journal of Alloys and Compounds, 585(2014): 622-632.

[14] CAO, R., FENG, Z., LIN, Q., CHEN, J.H.: Study on cold metal transfer welding-brazing of titanium to copper. Materials and Design, 56(2014): 165-173.

[15] CAO, R., WEN, B.F., CHEN, J.H., WANG, P.: Cold metal transfer joining of magnesium AZ31B-to-aluminum A6061-T6. Materials Science & Engineering A, 560(2013): 256-266.

[16] CAO, R., YU, G., CHEN, J.H., WANG, P.C.: Cold metal transfer joining aluminum alloys-to-galvanized mild steel. Journal of Materials Processing Technology, 213(2013): 1753-1763.

[17] CLIMATETECHWIKI [Accessed: 2016, April 14]. Available at: < http://www.climatetechwiki.org/technology/alu>

[18] CMT: Cold Metal Transfer [Accessed: 2016, February 26]. Available at: < http://www.axson.se/pdf/fro_bro_CMT_eng.pdf>

[19] CORROSION DOCTORS [Accessed: 2016, April 25]. Available at: < http://corrosion-doctors.org/Forms-fatigue/fatigue.htm#Checklist >

[20] CORROSIONPEDIA [Accessed: 2016, March 14]. Available at: <https://www.corrosionpedia.com/definition/347/crevice-corrosion>

[21] CO2CORROSIONCHEM409 [Accessed: 2016, March 11]. Available at: <https://co2corrosionchem409.wikispaces.com/Background+of+CO2+Corrosion >

[22] DAKEL [Accessed: 2016, June 07]. Available at: <http://www.dakel.cz/index.php?pg=prod/dev/xedo_en>

[23] DAVIS, J.R.: Corrosion (understanding the basics). ASM international, 2003. ISBN 0-87170-641-5.

[24] DIRECT INDUSTRY [Accessed: 2016, March 31]. Available at: <http://www.directindustry.com/>

[25] DOSTÁL, P.: Corrosive and stress degradation of Al-Mg Alloys. Dissertation presented to the Faculty of Agronomy, Mendel University in Brno, Czech Republic, 2011.

[26] DOSTAL, P., CERNY, M., LEV, J., VARNER, D.: Proportional monitoring of the acoustic emission in crypto-conditions. ACTA Universitatis Agriculturae Et Silviculturae Mendelianae Brunensis, 59(2011): 31-38.

[27] EFUNDA [Accessed: 2016, April 20]. Available at: <http://www.efunda.com/formulae/solid_mechanics/fatigue/fatigue_factor.cfm>

[28] ENGINEERS EDGE [Accessed: 2016, April 18]. Available at: < http://www.engineersedge.com/material_science/fatigue_failure.htm>

[29] EUROPEAN ALUMINIUM [Accessed: 2016, March 10]. Available at: <http://www.european-aluminium.eu/wp-content/uploads/2011/12/3-Arc-welding_2015_new.pdf>

[30] EUROPEAN ALUMINIUM [Accessed: 2016, March 21]. Available at: <http://www.european-aluminium.eu/wp-content/uploads/2012/01/AAM-Materials-4-Microstructure-and-properties.pdf>

[31] FONTANA, M.G.: Eight forms of corrosion, corrosion engineering (third edition). McGraw-Hill, 1986. ISBN 9-780-072939736.

[32] FREGONESE, M., IDRISSI, H., MAZILLE, H., RENAUD, L., CETRE, Y.: Initiation and propagation steps in pitting corrosion of austenitic stainless steels: monitoring by acoustic emission. Corrosion Science, 43(2001): 627-641.

[33] FRONIUS [Accessed: 2016, May 30]. Available at: <http://www.fronius.com/cps/rde/xbcr/SID-BBF1EF32-82E0BBF5/fronius_uk/CMTRobotics_pres_openhouse__538967_snapshot.pdf>

[34] FRONIUS INTERNATIONAL [Accessed: 2016, March 09]. Available at: <http://www.fronius.com/cps/rde/xchg/SID-7620BF8C-F9FA885B/fronius_international/hs.xsl/79_23609_ENG_HTML.htm#.Vt_j6-ZLdaA>

[35] FUNDAMENTALS OF ELECTROCHEMICAL ORROSION [Accessed: 2016, April 14]. Available at: <http://www.asminternational.org/documents/10192/3466254/ACFA9DE.pdf/dcf8d808-336a-4636-aadf-80b7e2092398>

[36] GE OIL & GAS [Accessed: 2016, March 31]. Available at: <www.geinspectiontechnologies.com>

[37] GOODHEART-WILLCOX PUBLISHER [Accessed: 2015, April 1]. Available at: <http://www.g-w.com/technology-engineering>

[38] GROSSE, C.U., OHTSU, M.: Acoustic emission testing (basics for research and applications in civil engineering). Springer-Verlag Berlin Heidelberg, 2008. ISBN 978-3-540-69865-1.

[39] GUPTA, M., SHARON, N.M.L.: Magnesium, magnesium alloys, and magnesium composites. John Wiley & Sons, 2011. ISBN 978-0-470-49417-2.

[40] INEC(THAILAND) [Accessed: 2016, March 17]. Available at: <http://siamkaewkumsai.blogspot.cz/2010/05/galvanic-corrosion.html>

[41] INTECH [Accessed: 2016, April 21]. Available at: <http://cdn.intechopen.com/pdfs/33625.pdf>

[42] INTERNATIONAL ATOMIC ENERGRY AGENCY [Accessed: 2016, March 31]. Available at: <http://www-pub.iaea.org/books/>

[43] INTERNATIONAL ATOMIC ENERGY AGENCY (IAEA) [Accessed: 2016, May 9]. Available at: <http://www-pub.iaea.org/MTCD/publications/PDF/TCS-48_web.pdf>

[44] INTERNATIONAL MAGNESIUM ASSOCIATION [Accessed: 2016, March 29]. Available at: < http://www.intlmag.org/magnesiumbasics/mech08.cfm >

[45] INTERNATIONAL MAGNESIUM ASSOCIATION [Accessed: 2016, March 29]. Available at: <http://www.intlmag.org/magnesiumbasics/what.cfm>

[46] IN®SLIDESHARE [Accessed: 2016, April 23]. Available at: <http://www.slideshare.net/SpringerIndia/fatigue-and-corrosion-in-metals>

[47] IOWA STATE UNIVERSITY [Accessed: 2016, March 31]. Available at: <http://www.iprt.iastate.edu/>

[48] ISO [Accessed: 2016, June 02]. Available at: <http://www.tc57.com/Pages/news_images/201194161013648.pdf>

[49] JIAN, X., XINQIANG, W., EN-HON, H.: Acoustic emission during pitting corrosion of 304 stainless steel. Corrosion Science, 53(2011): 1537-1546.

[50] JIAN, X., XINQIANG, W., EN-HOU, H.: Acoustic emission during the electrochemical corrosion of 304 stainless steel in H_2SO_4 solutions. Corrosion Science, 53(2011): 448-457.

[51] JING, S., KEHONG, W., QI, Z., DEKU, Z., JUN, H., GUANGLE, L.: Microstructure characteristics and mechanical properties of cold metal transfer welding Mg/Al dissimilar metals. Materials and Design, 34(2012): 559-565.

[52] JIRARUNGSATIAN, C., PRATEEPASEN, A.: Pitting and uniform corrosion source recognition using acoustic emission parameters. Corrosion Science, 52(2010): 187-197.

[53] JOMDECHA, C., PRATEEPASEN, A., KAEWTRAKULPONG, P.: Study on source location using an acoustic emission system for various corrosion types. NDT&E International, 40(2007): 584-593.

[54] KASAI, N., UTATSU, K., PARK, S., KITSUKAWA, S., KAZUYOSHI, S.: Correlation between corrosion rate and AE signal in an acidic environment for mild steel. Corrosion Science, 51(2009): 1679-1684.

[55] KIM, Y.P., FREGONESE, M., MAZILLE, H., FERON, D., SANTRINI, G.: Ability of acoustic emission technique for detection and monitoring of crevice corrosion on 304L austenitic stainless steel. NDT&E International, 36(2003): 553-562.

[56] KUMAR, N.P., VENDAN, S.A, SHANMUGAM, N.S.: Investigations on the parametric effects of cold metal transfer process on the microstructure aspects in AA6061. Journal of Alloys and Compounds, 658(2016): 255-264.

[57] LEITELT BROS [Accessed: 2016, March 30]. Available at: <http://www.lbfoundry.com/aluminum-sand-castings.html>

[58] LIEBISCH LABORTECHNIK [Accessed: 2016, March 15]. Available at: <http://www.liebisch.com/englisch/html/prufstandards.htm>

[59] LINCOLN [Accessed: 2016, May 30]. Available at: <http://www.lincolnelectric.com/en-gb/Pages/default.aspx>

[60] LISKUTIN, P., MAZAL, P., FIALA, J., VLASIC, F.: Application of NDT Procedures for identification of fatigue life stages of AlMg Alloys. 17th World Conference on Nondestructive Testing, 25-28 Oct 2008, Shanghai, China.

[61] LUI, Y., ZHI, Y., XIE, X., ZHU, Y., WAN, R.: Effect of welding heat input to metal droplet transfer characterized by structure-borne acoustic emission signals detected in GMAW. Measurement, 70(2015): 75-82.

[62] MAGNESIUM ELEKTRON [Accessed: 2016, March 29]. Available at: <http://www.fire.tc.faa.gov/2007conference/files/Materials_Fire_Safety/WedAM/GwynneMagnesium/GwynneMagnesiumPres.pdf>

[63] MATMEB [Accessed: 2016, May 27]. Available at: <http://www.matweb.com/search/datasheettext.aspx?matguid=d24f94ab8e154fa7b659a816986ba10e>

[64] MAZAL, P., LISKUTIN, P.: Experimental evaluation of fatigue properties of wrought Al alloys EN AW-6082 and EN AW-7075. Metal 2010, 18-20.5.2011, Brno, Czech Republic, EU.

[65] MAZAL, P., VLASIC, F., KOULA, V.: Use of acoustic emission method for identification of fatigue micro-cracks creation. Procedia Engineering. 133 (2015): 379-388.

[66] MERIDIAN [Accessed: 2016, March 17]. Available at: <http://www.meridian-mag.com/magnesium-die-casting/magnesium-vs-steel/>

[67] MID-ATLANTIC CASTING SERVICES [Accessed: 2016, March 30]. Available at: <http://www.mid-atlanticcasting.com/alum-casting-alloys_FEB05.pdf>

[68] MISTRAS [Accessed: 2016, February 26]. Available at: <http://www.mistrasgroup.com/products/technologies/acousticemission.aspx>

[69] MITOPENCOURSEWARE [Accessed: 2016, April 19]. Available at: <http://ocw.mit.edu/courses/materials-science-and-engineering/3-11-mechanics-of-materials-fall-1999/modules/fatigue.pdf>

[70] MW INDUSTRIES [Accessed: 2016, April 19]. Available at: <http://www.mw-ind.com/pdfs/GoodmanFatigueLifeEstimates.pdf>

[71] NDT.NET [Accessed: 2016, Mya 9]. Available at: <http://www.ndt.net/article/v05n09/berke/berke1.htm>

[72] NDT RESOURCE CENTER [Accessed: 2016, March 31]. Available at: <https://www.nde-ed.org/index_flash.htm>

[73] NDT RESOURCE CENTER [Accessed: 2016, May 9]. Available at: <https://www.nde-ed.org/EducationResources/CommunityCollege/PenetrantTest/Principles/prosandcons.htm>

[74] NDT RESOURCE CENTER [Accessed: 2016, May 9]. Available at: <https://www.nde-ed.org/EducationResources/CommunityCollege/Ultrasonics/Introduction/description.htm>

[75] NDT RESOURCE CENTER [Accessed: 2016, April 19]. Available at:<https://www.nde-ed.org/EducationResources/CommunityCollege/Materials/Structure/fatigue.htm>

[76] OLYMPUS [Accessed: 2016, May 9]. Available at: <http://www.olympus-ims.com/en/eddycurrenttesting/>

[77] PAUL K.: Welding of sheet metal using modified short arc MIG/MAG welding process. Master thesis presented at the Laboratory of Welding Technology, Department of Mechanical Engineering, Lappeenranta University of Technology. Finland. 2007 [Accessed: 2016, March 10].

[78] PHILIP, A., SCHWEITZER, P.E.: Encyclopedia of corrosion technology (second edition, revised and expanded). Marcle Dekker, Inc, 2004. ISBN 0-8247-4878-6.

[79] PICKIN, C.G., YOUNG, K.: Evaluation of cold metal transfer (CMT) process for welding aluminium alloy. Science and Technology of Welding and Joining [Accessed: 2016, March 09]. Available at: <https://weldconsultuk.files.wordpress.com/2013/01/cold-metal-transfer.pdf>

[80] PIERRE, R.R.: Handbook of corrosion engineering (second edition). The McGraw-Hill Companies, 2012. ISBN 978-0-07-175037-0.

[81] Q-LAB [Accessed: 2016, March 15]. Available at: <http://www.q-lab.com/documents/public/9d6596d5-0667-498d-9303-94b87a1ff9df.pdf>

[82] ROBERGE, P.R.: Corrosion engineering, Principles and Practice. McGraw-Hill, 2008. ISBN 978-0-07-148243-1.

[83] RONNIE, K.M., ERIC, V.K.: Nondestructive testing handbook, acoustic emission testing (third edition). American society for nondestructive testing, 2005. ISBN 1-57117-106-1.

[84] ROSADO, T., ALMEIDA, P., PIRES, I., MIRANDA, R., QUINTINO, L.: Innovation in arc welding. In: 2 Congresso de Engenharia de Mocambique. September 2, 2008, Maputo [Accessed: 2015, September 01]. Available at: <https://fenix.tecnico.ulisboa.pt/downloadFile/3779571903885/mocambique.pdf >

[85] SMITH, W.F.: Principles of materials science and engineering. McGraw-Hill, 1986. ISBN 0-07-058521-0.

[86] SMITH, W.F., HASHEMI, J.: Foundations of materials science and engineering (fifth edition), 2006. ISBN 978-0-07-352924-0.

[87] SUBSTECH [Accessed: 2016, April 14]. Available at: <http://www.substech.com/dokuwiki/doku.php?id=wrought_magnesium_alloys >

[88] SUBSTECH [Accessed: 2016, April 21]. Available at: <http://www.substech.com/dokuwiki/doku.php?id=pitting_corrosion>

[89] SURESH, S.: Fatigue of materials (second edition). CAMBRIDGE UNIVERSITY PRESS, 2004. ISBN 0-521-57847-7.

[90] THE AMERICAN SOCIETY FOR NONDESTRUCTIVE TESTING [Accessed: 2016, May 9]. Available at: <https://www.asnt.org/MinorSiteSections/AboutASNT/Intro-to-NDT>

[91] THE MAGNESIUM HOME PAGE [Accessed: 2016, March 31]. Available at: <http://mg.tripod.com/mggen.htm#prod>

[92] THE MEMBER JOURNAL OF THE MINERALS, METALS&MATERIALS SOCIETY [Accessed: 2016, February 26]. Available at: <http://www.tms.org/pubs/journals/jom/9811/huang/huang-9811.html>

[93] THE MULTIMEDIA CORROSION GUIDE [Accessed: 2016, March 14]. Available at: <http://www.cdcorrosion.com/mode_corrosion/corrosion_image/caverneuse_2_zoom.jpg>

[94] THE NATIONAL BOARD OF BOILER AND PRESSURE VESSEL INSPECTORS [Accessed: 2016, May 9]. Available at: <http://www.nationalboard.org/index.aspx?pageID=164&ID=374>

[95] TOTAL MATERIA [Accessed: 2016, April 19]. Available at: <http://www.totalmateria.com/articles/Art49.htm>

[96] TRETHEWEY, K.R., CHAMBERLAIN, J.: Corrosion for science and engineering (second edition). Longman Group Limited, 2001. ISBN 0-582-238692.

[97] TRINITY NDT [Accessed: 2016, May 9]. Available at: <http://www.trinityndt.com/services_mt.php>

[98] UCDAVIS CHEMWIKI [Accessed: 2016, March 14]. Available at: <http://chemwiki.ucdavis.edu/Core/Analytical_Chemistry/Electrochemistry/Case_Studies/Corrosion/Corrosion_Basics>

[99] UNIVERSITY OF BABYLON [Accessed: 2016, April 14]. Available at: <http://www.uobabylon.edu.iq/eprints/paper_12_1893_228.pdf>

[100] VALLEN, H.: Acoustic emission testing; fundamentals, equipment, applications. Castell Publication Inc, 2006. ISBN 3-934 255-26-4.

[101] VALLEN SYSTEME [Accessed: 2016, May 10]. Available at: <http://www.vallen.de/sites/default/files/sov1212.pdf>

[102] VARNER, D.: Acoustic emission during static bending of wood specimens. Dissertation presented to the Faculty of Agronomy, Mendel University in Brno, Czech Republic, 2012.

[103] VLASIC, F., HOHAL, L., MAZAL, P., LISKUTIN, P.: Study of high-cycle fatigue behavior of titanium alloy using acoustic emission method. Metal 2013, 15-17.05.2013, Brno, Czech Republic, EU.

[104] WEBCORR CORROSION CONSULTING SERVICES [Accessed: 2016, April 23]. Available at: <http://www.corrosionclinic.com/types_of_corrosion/pitting_corrosion.htm>

[105] WIKIPEDIA [Accessed: 2016, March 31]. Available at: <https://en.wikipedia.org/wiki/Magnetic_particle_inspection>

[106] WILLIAM, D.C., DAVID, G.R.: Fundamentals of materials science and engineering (fourth edition), 2013. ISBN 978-1-118-32269-7.

[107] WOONGGI, H., SEUNGGI, B., JAESEONG, K., SUNGSIK, K., NOGWON, K., BOYOUNG L.: Acoustic emission characteristics of stress corrosion cracks in a type 304 stainless steel tube. Nucl Eng Technol, 47(2015): 454-460.

LIST OF FIGURES

LIST OF TABLES

LIST OF ABBREVIATIONS

A	area
AE	acoustic emission
AET	acoustic emission testing
ASTM	American society for testing and materials
CMT	cold met transfer welding
d	density (g/cm^3)
DLL	dynamic link library
Eq	equation
K	constant number
N	the number of loading cycles
NDT	Non-destructive testing
PSB	persistent slip bands
PSD	power spectral density
PT	penetrant testing
T	time of exposure (hour)
R	corrosion rate, stress ration
RE	rare earth elements
RMS	root mean square
RT	radiographic
RVT	remote visual testing
S	constant cyclic stress amplitude
SCC	stress corrosion crack
SEM	scanning electron microscope
UT	ultrasonic testing
VI	visual inspection
W	weight loss (g)
a_f	critical crack size
a_0	crack size from the initial crack size
da/dN	fatigue crack growth rate
I_{anodic}	anodic current
$I_{cathodic}$	cathodic current
ΔK	stress-intensity factor

K_{max}	stress-intensity factor at maximum cyclic stress
K_{min}	stress-intensity factor at minimum cyclic stress
N_f	cycles to failure
S_a	anodic surface area
S_c	cathodic surface area
Y	geometric correction factor
σ_e	endurance limit
σ_{max}	stress value at maximum cyclic stress
σ_{min}	stress value at minimum cyclic stress

APPENDIX

Certificate of calibration of IDK-09-MU14 confirmed by *DAKEL*

SN	430-11	*Connector :*	coaxial cable with BNC connector
Type :	IDK-09-MU14	*Working temperature :*	0 - +70 °C
Case :	stainless steel	*Max. rel. humidity :*	100%
Contact surface :	alumina ceramic 99.6		

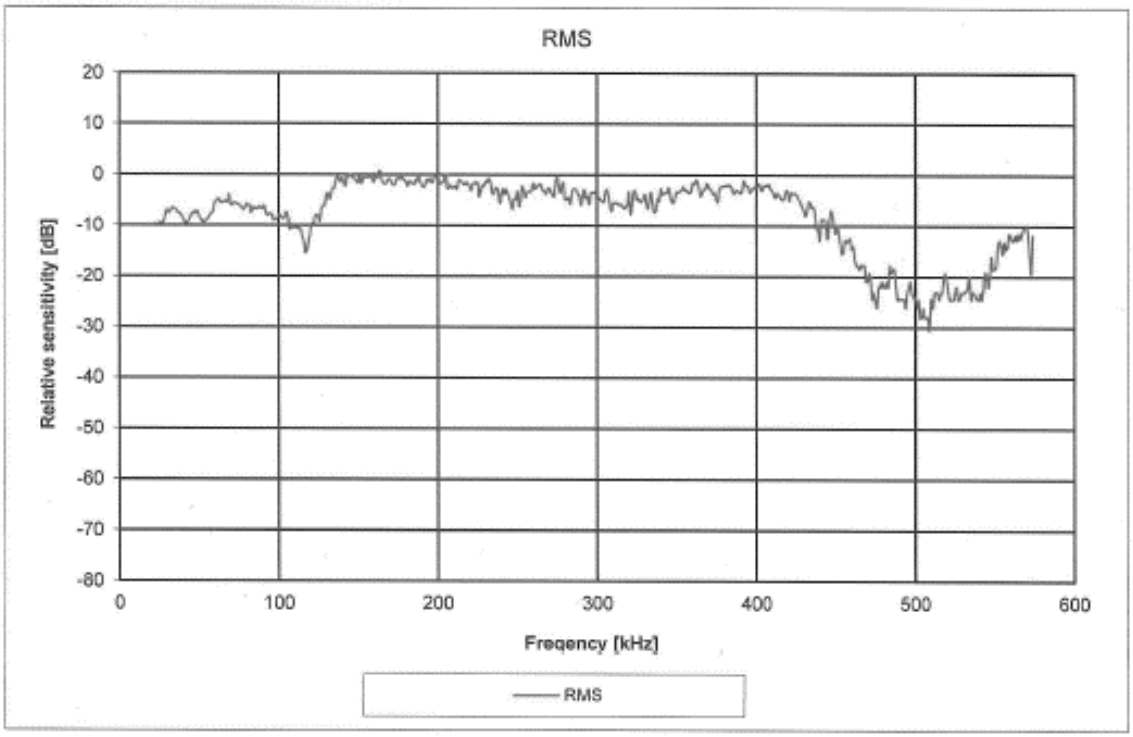

Method of calibration :	Frequency wobble (sweep from 25 to 600 kHz, velocity 5 kHz/sec) in system sensor/pulser	
Relative sensitivity :	Count 1, Count 2:	Number of overshot a treshold (300 resp. 600 ‰ of range) in correlation with pusler freqency
	RMS:	True RMS in relation to 1000mV
Temperature of calibration :	20 °C	
Date of calibration :	16.7.2014	*Sign :*